PERFORMANCE MODELING AND VALIDATION OF A CHIRPED PULSE QUANTUM CASCADE LASER FOR OPEN-PATH AMBIENT GAS MONITORING

by

MAUNG THET LWIN

A dissertation submitted to the Graduate Faculty in Engineering in partial fulfillment of the requirements for the degree of Doctor of Philosophy

The City University of New York

2010

This manuscript has been read and accepted for the Graduate Faculty in Engineering in satisfaction of the dissertation requirement for the degree of Doctor of Philosophy.

Professor Fred Moshary

Date — Chair of Examining Committee

Professor Mumtaz Kassir

Date — Executive Officer

Prof. Barry Gross (Co-Mentor), Dept. of Electrical Engineering, CUNY

Prof. Samir Ahmed, Dept. of Electrical Engineering, CUNY

Dr. Mark Arend, NASA/NOAA-CREST, CCNY

Dr. John E. Selby, Northrop Grumman Corporation

Supervisory Committee

THE CITY UNIVERSITY OF NEW YORK

Abstract

PERFORMANCE MODELING AND VALIDATION OF A CHIRPED PULSE QUANTUM CASCADE LASER FOR OPEN-PATH AMBIENT GAS MONITORING

by

Maung Lwin

Adviser: Professor Fred Moshary, Professor Barry Gross (Co-Mentor)

The quantum cascade laser (QCL) has been successfully used to measure atmospheric trace-gas concentrations at part per billion by volume (ppbv) in portion of the mid-infrared (mid-IR) region (3-5, 8-10 μm). In this proposal, we explore the feasibility of using a time chirped pulsed QCL to simultaneously measure ozone (O_3) and ammonia (NH_3) which are two important gases in ground level air because of their adverse impact on human, and the role they play in climate change. Based on careful optimization of the spectral absorption features of O_3 and NH_3 as well as interfering gases, we present a numerical simulation approach for a compact open-path system design that can detect O_3 and NH_3 concentrations to 1% ambient concentration levels. .

The Quantum Cascade Laser Open-path System (QCLOPS) we are optimizing uses a single distributed feedback (DFB) QCL operating at 9.6 μm wavelength (1045 cm^{-1} in wavenumber and turning range of 2 cm^{-1}), which corresponds to the best absorption lines of O_3, and NH_3 in the presence of interfering gases H_20 and CO_2. Based on accurate

measured chirp responses, both the spectral sampling and the resolution are derived and used to simulate the convolved spectral response for all ambient gases calculated from the monochromatic spectral responses from GENSPECT (a line-by-line molecular transition simulation code). This allows us to estimate the required SNR needed per pulse to reach the needed trace gas detection levels for ambient urban conditions using linear least square analysis.

Once the per-pulse SNR requirements are determined, an open-path system model (OPSM), which evaluates the laser-matter interactions in the atmosphere including scattering, geometric and turbulence losses as well as the details of the light source, remote target and receiver is proposed and used to determine the feasibility of measuring the ambient species. In particular, the model is used to assess the measurement duration needed to obtain specified retrieval thresholds as a function of the path length and realistic laser power and noise sources. In particular, we find that for path lengths as short as 100 meters, 1% ambient concentrations can be measured with durations < 1min while 1% ambient levels can be realistically done in < 1s at path lengths between 1km and 6km.

Due to unavailability of QCL at the optimized wavelength, the approach was applied instead to an equivalent system which was readily available. This prototype instrument, called QCLOPS-CCNY, uses a 5.3 μm QCL instead of 9.6 μm QCL. While this system is not designed for Ozone-Ammonia, it is suitable for measurements of water vapor which also provides us with a means of validation against Meteorological surface measurements as well as complementary open-path FTIR measurements. Preliminary measurements for links of L=120 m were made that validate many facets of the

simulation model including the convolved trace gas absorption spectrum, inversion algorithm and the link-budget analysis including both the detector and path noises. Comparisons with both FTIR and ambient MET models show retrieval performances < 2% providing confidence that our Ozone-Ammonia estimates are reasonable.

This thesis is dedicated to

my parents, U Maung Win and Daw Ma Lone

and my wife, MyaMya Teiktin

Acknowledgements

First and foremost, I would like to thank my mentor Professor Moshary for the opportunities he gave me to work in this project. I would like to thank him for giving me financial security and for showing me how to do the research properly.

This thesis would have never been completed without the guidance of my co-mentor Prof. Gross. I have gained a lot of knowledge from his valuable comments, constant support and discussion I had with him. I express my special gratitude to Dr. Paul Corrigan for his suggestion in the project of my work, his kind supervision and continuous guidance and help during my research, his valuable notes during discussion. I also thank to Professor Ahmed, Dr. Mark Arend, and Dr. John Selby for kindly serving on my thesis committee.

I would like to thank all the current and former group members who I have interacted with: Paulo Castillo, Carlos Padilla, Alexandra Tsekeri, Amandeep Chhabra and Reuven Huntley, for their support, helpful discussion as well as their friendship.

Finally, I would like to thank the Mid-InfraRed Technologies for Health and the Environment Center (MIRTHE) and NSF for the financial support.

Table of Contents

1. INTRODUCTION 1

Thesis Outline 5

References.....7

2. MID-INFRARED LASER ABSORPTION SPECTROSCOPY FOR TRACE GAS DETECTION 8

2.1. The Composition and Structure of the Atmosphere and Impacts of Ozone and Ammonia on Human Health 8

2.2. Mid-infrared Laser Absorption Spectroscopy 10

2.2.1. Rotational-vibrational Transitions of Molecules 10

2.2.1a. Ozone (O_3) 12

2.2.1b. Ammonia (NH_3).....13

2.2.2. Translation Line Strength and Shape 14

2.2.3. HITRAN Spectral Database 17

2.3. Quantitative Analysis 18

2.3.1. The Retrieval Method of the QCLOPS 18

2.3.2. Program Functions 20

2.4. QCL based Open-path Trace Gas Sensor System 22

2.4.1. Mono-static Retroreflector and Backscattering Systems 22

2.4.2. Quantum Cascade Laser 24

References 30

3. CHARACTERIZATIONS OF THE QCLOPS DESIGN 33

3.1. Spectral Window Searching for Ozone and Ammonia Simultaneous Detection ...33

3.2. System Components 36

3.2.1. The Quantum Cascade Laser and Controller Module 37

3.2.1a. Characterization of the QCL, DQ9-M784I (9.53 μm emission) 39

3.2.2. Thermoelectrically Cooled MCT Detector 41

3.2.3. Telescope and Chassis Design 43

3.2.4. Optical Setup 46
3.3. Resolution Limit 49
3.4. Link Power Analysis (Open-path System Model) 50
3.4.1. Power Loss due to Scattering 51
3.4.2. Power Loss due to Atmospheric Turbulence 52
3.4.3. Power Loss due to Molecular Absorption 53
3.4.4. Free Space Loss due to the Laser Beam Divergence 54
3.4.5. Power Loss due to System's Optics 57
3.4.6. Quantifying System Noise 58
3.4.7. The Open-path System Model Simulation Results for O_3-NH_3 System 59
References 64

4. VALIDATION MEASUREMENTS 66
4.1. Introduction 66
4.2. Laboratory Measurements 72
4.2.1. Laser Tuning Rate Measurements 72
4.2.2. Multi-pass Gas Cell Measurements 76
4.3. Field Measurements 81
4.3.1. Operating Temperature and Path-length Configuration 82
4.3.2. Comparison between QCLOPS and FTIR Measurements 89
4.3.3. Measurements to Quantify the QCLOPS System Noise 94
4.4. Validating Link Power Analysis Model using QCLOPS Field Measurements 100
4.4.1. Required SNR for 5.3 μm Region 100
4.4.2. Model Simulation 101
4.4.3. Comparison of Model and Measurement Results 104
References 106

5. SUPPLEMENTAL STUDY 108
5.1. Backscattering Measurements of the Urban Building Materials 108
5.1.1. Introduction 108
5.1.2. Theoretical Background 109

5.1.3. Experimental Setup 109
5.1.4. Measurement Samples 111
5.1.5. Results and Discussion 112
References 120

6. CONCLUSION 121
6.1. Summary of the Thesis 121
6.2. Proposed Future Works 122

7. APPENDIX 126
A. Further Investigation on the System Noise to Compare the Measurements with the Model simulation Results 126
B. Investigation on Quantization Level and Noise Signal in the Process of Averaging Samples to Improve Measurement SNR 131
References 133

8. BIBLIOGRAPHY 134
9. PUBLICATION AND PRESENTATIONS 142

List of Tables

Chapter 3

Table 3.1: Main system components, QCL, detector and telescope parameters of the QCLOPS 36
Table 3.2: Applied voltage, current on the laser chip and output power of DQ9-M784I QCL when laser temperature is 35˚C 39
Table 3.3: Applied voltage, current on the laser chip and output power of DQ9-M784I QCL when laser temperature is 10˚C 40
Table 3.4: List of required values and designed values of telescope parameters along with their locations 46
Table 3.5: Locations and positions description list of QCL, detector and optics components on the system upper level board 48

Chapter 4

Table 4.1: Summary of field measurements using QCLOPS-CCNY 81
Table 4.2: Comparison of results based on data from CCNY weather station and data from QCLOPS measurements 88
Table 4.3: Comparison of noise level from QCLOPS indoor and field measurements 98
Table 4.4: Comparison of SNRs calculated by the model and measurements 104

Chapter 5

Table 5.1: Summary of albedo measurements on building materials using QCL and FTIR 117

List of Figures

Chapter1

Figure 1.1: Photos of healthy lung airway (left) and inflamed lung airway (right) 2

Figure 1.2: Comparison of absorbance spectra of O_3 and NH_3 in mid-IR and near-IR regions.....2

Figure 1.3: System layout of a Quantum Cascade Laser Open-path System 3

Chapter 2

Figure 2.1: Relative positions of ro-vib transitions in the absorption spectrum of a molecule where v and J are vibrational and rotational quantum numbers, v" has higher energy level than v' 10

Figure 2.2: Fundamental vibrational modes of O_3 with its structures 12

Figure 2.3: Absorption cross section of the symmetric stretching mode (v_1), bending mode (v_2) and asymmetric stretching mode (v_3) of O_3 in atmospheric pressure and temperature (left) and the close up view of strongest v_3 band showing P and R branches (right) 13

Figure 2.4: Absorption cross section of the fundamental vibrational modes, v_1, v_2, v_3, and v_4 of NH_3 in atmospheric pressure and temperature (left) and the close up view of strongest v_2 band (right) 14

Figure 2.5: A block diagram of the retrieval method 19

Figure 2.6: Schematic of monostatic open-path trace gas detection system using a retroreflector 23

Figure 2.7: Schematic of monostatic open-path backscattering system 23

Figure 2.8: a) Interband transitions in conventional semiconductor lasers emit a single photon. b) In quantum cascade structures, electrons undergo intersubband transitions and photons are emitted. The electrons tunnel to the next period of the structure and the process repeats. 25

Figure 2.9: Micrograph of a cross section of a QCL with several stages of active and injector layers and MBE process 26

Figure 2.10: Scheme of convention band energy diagram of two QCL active regions based on a three-well vertical transition mechanism. The laser transition is indicated by the vertical arrows and the electron flow by the horizontal arrows. 27

Chapter 3

Figure 3.1: Theoretical result of optimum micro-window that requires minimum SNR for O_3 and NH_3 to obtain 1% accuracy measurement 35
Figure 3.2: Required SNR with retrieval error 35
Figure 3.3: a) QCL on SN mounting, b) Cascade QCL module, and c) Cascade QCL controller module 38
Figure 3.4: Interface connections among QCL module, laser controller module and a computer 38
Figure 3.5: Applied voltage to laser controller and effected current on the laser chip (left), and comparison of measurement and data provided by the Maxion (right) 40
Figure 3.6: Current on the laser chip and emitted average power as a function of applied voltage in 10°C operation temperature 41
Figure 3.7: Detector performance, D* value with corresponding wavelength 42
Figure 3.8: a) PVI-3TE-10.6 detector in TO-8 package, b) wire connection and c) the completed detector with DB9, SMA interfaces and air cooling fan attached 42
Figure 3.9: The schematic of the telescope and system components 44
Figure 3.10: Design choice of the secondary mirror location with mirror diameter 45
Figure 3.11: Schematic diagram of optical setup of the system on the second level board 47
Figure 3.12: Resolution limit and detector bandwidth as a function of QCL tuning mechanism 49
Figure 3.13: Power loss due to scattering 52
Figure 3.14: Rytov Variance of the 9.6 μm laser transmission using the atmospheric structure function $C_n^2 = 10^{-14}$ (top) and power loss due to turbulence against with path-length (below) 53

Figure 3.15: Power loss due to ambient gas (H_2O + CO_2 + O_3 + NH_3) absorption (generated using GENSPECT and HITRAN database) 54
Figure 3.16: Geometry of the mono-static retroreflector open-path system to calculate divergences for 1) from laser module to the retroreflector and 2) from the retroreflector to the telescope 55
Figure 3.17: Diagram of the Galilean beam expander 59
Figure 3.18: Optical efficiency of retroreflector system (left) and backscattering system (right) 60
Figure 3.19: SNR with path-length for the retroreflector system (DAQ noise, which depends on the signal, is dominant so that the SNRs do not change much from L=100m to 3km. Then, the preamplifier noise, which is a constant for the specific gain, makes the SNRs decrease from 50 for L=4km to 1.5 for L=10km. 61
Figure 3.20: Number of samples required to achieve 1% accuracy result 62
Figure 3.21: The measurement time to achieve 1% accuracy result (P_{QCL}=200mW, pulse rate=20 kHz) 63

Chapter 4

Figure 4.1: Measured pulse signal of 5.3 μm QCL (DQ5-M575R) 68
Figure 4.2: Absorbance spectra of H_2O, CO_2, O_3, and NH_3 in ambient concentration and atmospheric pressure and temperature (generated using GENSPECT and HITRAN 2000 database) 69
Figure 4.3: Top view of the system showing the QCL beam trace and red laser beam trace 71
Figure 4.4: Experimental setup for QCL tuning rate measurement; 1) reference spectrum measurement when the etalon is out of laser beam path and 2) etalon fringes measurement when the etalon is installed on the laser beam path 73
Figure 4.5: Reference signal, etalon fringe pattern and normalized fringes of the DQ5-M575R with T_{QCL} = 25°C and pulse width = 500 ns 74
Figure 4.6: Laser tuning rate and tuning range at T_{QCL} = 10°C and pulse width = 500ns 75

Figure 4.7: Laser tuning rate and tuning range at T_{QCL} = -5°C and pulse width = 1 µs. Its average tuning rate is 0.022 cm^{-1}/ns and the calculated spectral resolution is 0.008 cm^{-1} 76
Figure 4.8: Experimental setup of 5.3 µm DFB QCL with a 210 m multi-pass gas cell 78
Figure 4.9: Reference signal and absorption signal of the 213 m multi-pass gas cell measurement 79
Figure 4.10: Spectral fitting of measurement spectrum with synthetic reference spectrum 80
Figure 4.11: GESPECT generated theoretical transmission spectrum of water vapor 82
Figure 4.12; Photo of instrument setup 83
Figure 4.13: Measurement spectra, (A) received signal with 60 m path-length, (B) recorded background signal 84
Figure 4.14: Background eliminated signal of fig. 4.13 A 85
Figure 4.15: Measurement absorption spectrum using laser temperature of 25°C. An absorption peak can be seen near 200^{th} data point. 86
Figure 4.16: The measurement signal (left), absorption spectra of L=60 m measurement and L=60 m, concentration =$3.4071x10^3$ ppm reference (right) 86
Figure 4.17: Absorption spectra of (L=40m) measurement and (L=40m, conc. = $3.3761x10^3$ ppm) reference 87
Figure 4.18: The positions of two systems, QCLOPS and OP-FTIR, and their absorption path-lengths (20m for OP-FTIR and 40m for QCLOPS) 90
Figure 4.19: Photos of two systems (QCLOPS and OP-FTIR) describing system telescopes and light source/retroreflector positions with optical path-lengths 90
Figure 4.20: The measurement result, H_2O concentration and spectrum fitting of measurement and reference absorption spectra 91
Figure 4.21: OP-FTIR measurement and reference fitting spectra 92
Figure 4.22: Comparison of QCLOPS, OP-FTIR and the weather station data results 92
Figure 4.23: Scatter plots weather station result against QCLOPS result (left) and weather station result against OP-FTIR result (right) 93
Figure 4.24: Measurement signals of first two samples using QCLOPS 95

Figure 4.25: The positions of three points (P1, P2, and P3) and analyzed signal part (red box) 97
Figure 4.26: Mean and standard deviation of indoor measurement signal at P1 (left) and P2 (right) (see also fig. 4.24) 97
Figure 4.27: Mean and standard deviation of field measurement signal at P1 (left) and P2 (right) (see also fig. 4.24) 98
Figure 4.28: Required SNR for H_2O, CO_2, O_3 and NH_3 vs. fractional error (left) and absorbance spectra of H_2O, CO_2, O_3 and NH_3 in ambient concentration, atmosphere temperature and pressure (right) 100
Figure 4.29: Absorption feature of H_2O for L=40m 101
Figure 4.30: Particle scattering loss, turbulence loss and free space loss as the function of path-lengths 102
Figure 4.31: The model simulation result of total RMS noise and noise voltages from detector, pre-amp and DAQ system as the function of path-length. The noise voltage curves (total RMS noise and DAQ noise) are not continuous because they are calculated from the noise voltage of received signal for 40m, 60m, 100m, and 120m path-length (coarse interval). 103
Figure 4.32: Comparison of 5.3μm measurements and model results (4mrad and 3mrad QCL beam divergences on model calculation) 104

Chapter 5

Figure 5.1: Schematic diagram of an active chemical sensor system. Transmitted QCL beam is reflected back by a building wall or a target of opportunity through chemical plume and collected onto a receiver of the system. 108
Figure 5.2: Schematic diagram of backscattering measurement setup with QCL and Lock-in amplifier 110
Figure 5.3: Experimental setup with IR source and FTIR 111
Figure 5.4: Reflectivity of common urban building wall materials with viewing angle from -90° to +10° 112
Figure 5.5: Reflectivity of weakly reflected materials 113
Figure 5.6: Reflectivity of different roughness aluminum surfaces 114

Figure 5.7: (a) Reference spectrum (reflected signal from goal coated mirror) and sample spectrum (reflected signal from polished granite), (b) calculated reflectivity of polished granite 114
Figure 5.8: Calculated spectrum of reflectivity for sanded aluminum surfaces from 400 – 2500 cm^{-1} 115
Figure 5.9: Comparison of reflectivity measurements using QCL and FTIR 116
Figure 5.10: Calculated SNR for open-path backscattering systems using granite, marble, or white ceramic wall and aluminum wall between 100m and 250m path-length 118

Chapter 6

Figure 6.1: H_2O absorption feature in the spectral window in which current 5.3 μm QCL can be operated (left), and detailed view of H_2O small feature between 1898 and 1899 cm^{-1} (right) 123
Figure 6.2: Required SNR of H_2O concentration retrieval in 1898-1899 cm^{-1} window as the function of fractional error 123
Figure 6.3: The link model simulation results (number of samples and measurement time) for H_2O peak retrieval at 1898-1899 cm^{-1} window (pulse rate = 20 kHz) 124

Appendix

Figure A-1: Rytov variance and scintillation index with aperture averaging 128
Figure A-2: Comparison of turbulent noise with detector noise, preamp noise (without gain factor), DAQ noise and total RMS noise 128
Figure A-3: Comparison of quantized measurement and real measurement: (A) N=0.1R, (B) N=R, and (C) N=10R 132
Figure A-4: Results of 100 cases 132

CHAPTER 1: INTRODUCTION

Air pollution is not a modern problem and understanding the fate of pollutants in the atmosphere depends on the ability to measure them accurately and precisely. The development of the quantum cascade laser (QCL) aims to address these issues and has opened a new chapter in spectroscopy and particularly in trace gas measurement. These measurements are used in a number of areas such as air quality, industrial or pollutant control and monitoring of greenhouse gases, which are responsible for global warming and human health diseases. An open-path measurement system allows path integration of the gases concentrations over long path lengths and since it is not sampling gases directly, it is suitable to use in urban environment where air pollution is usually concentrated [1].

More chemicals absorb light in the infrared (IR) region than in the ultraviolet (UV) region [2], which gives the open-path mid-IR Differential Optical Absorption Spectroscopy (DOAS) technique an advantage over the traditionally used open-path UV-DOAS technique. Another advantage of the mid-IR DOAS technique over the UV-DOAS is the much smaller mid-IR light extinction, scattering due to the molecules and aerosols, in comparison to the UV light extinction (Rayleigh scattering). For that reason, UV-DOAS systems can rarely measure in ranges greater than 2 km and they fail to perform accurately in severe weather or foggy conditions [2].

Despite their low concentration, part per million (ppm) to part per billion (ppb), ozone (O_3) in ambient air play an important role as potential tosins which are responsible for lung cancer and damage in respiratory system and ammonia (NH_3) can cause negative

impacts in climate changes by contributing to the formation of air pollutant known as particulate matter $PM_{2.5}$ (size < = 2.5μm) [3, 4]. For example, exposure of O_3 can inflame lung airway and the photo of inflamed lung airway is shown in figure 1.1.

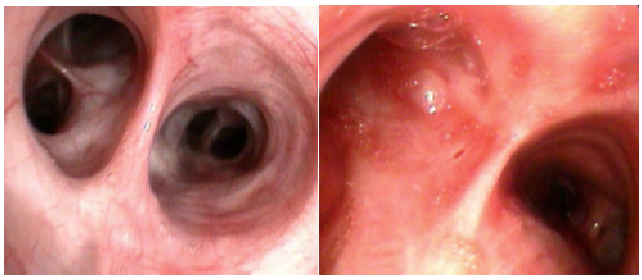

Figure1.1: Photos of healthy lung airway (left) and inflamed lung airway (right) [4]

Since the vibrational-rotational absorption lines of O_3 and NH_3 at mid-IR region are 1-2 orders of magnitude stronger than their absorbance at near IR region, and their absorption lines overlap as shown in figure 1.2, making their sensitive simultaneous measurement possible in mid-IR region [5, 6].

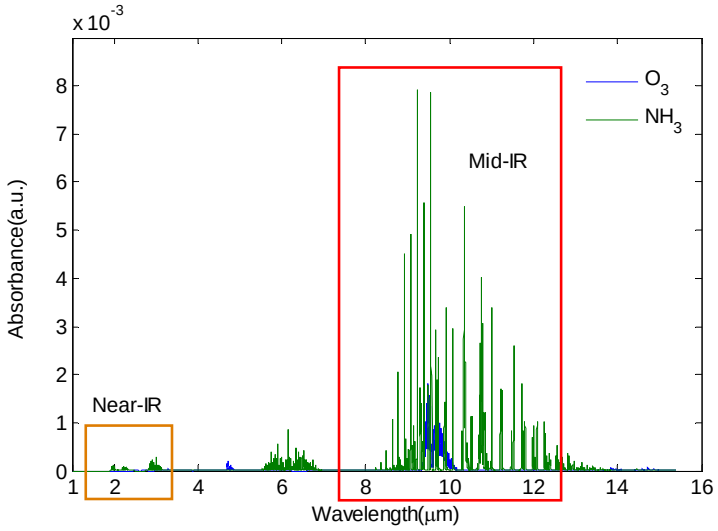

Figure 1.2: Comparison of absorbance spectra of O_3 and NH_3 in mid-IR and near-IR regions

The conventional instrument for open-path IR measurements is the Fourier Transform Interferometer (FTIR). The FTIR uses an incoherent light source that operates at 2 – 20 μm range and it can measure for path length of 100's m with low resolution, 0.5 cm^{-1} (open-path FTIR system by MIDAC). The FTIR works well for monitoring gases like CO_2 or H_2O, but for trace gases with weaker absorptions and concentrations in the ppb level, like O_3 and NH_3 in ambient concentration, it fails to provide accurate results [6].

Among mid IR light sources, the QCL can be operated in room temperature (RT) (with thermoelectrically cooled (TE) cooling) at conditions that are not possible to operate lead salt lasers. The QCL has higher brightness coherent light with much higher spectral resolution than light source used in FTIR instrument [7]. At present, there is a instrumentation gap between laboratory and open-path trace gas measurement with QCL [8]. The system layout of a traditional mono-static retroreflector system with QCL is shown in figure 1.3.

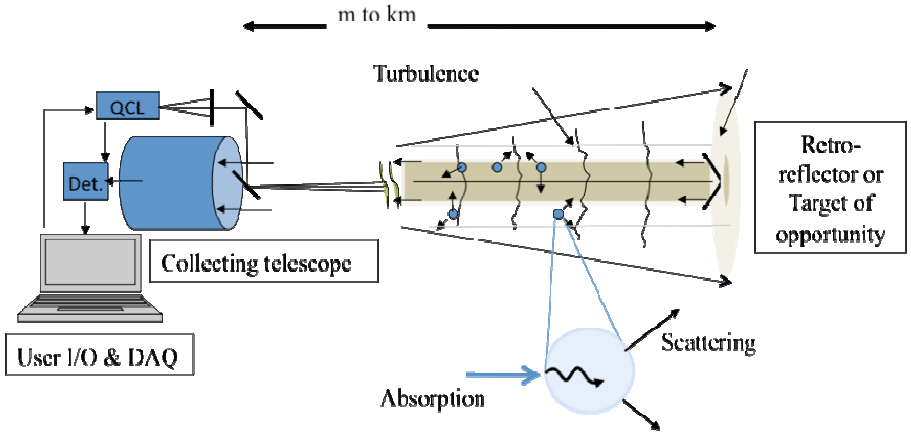

Figure 1.3: System layout of a Quantum Cascade Laser Open-path System

To begin our analysis, we first investigated the spectral transmission of all relevant gases, such as ozone (O_3), ammonia (NH_3), carbon-dioxide (CO_2), and water

vapor (H_2O) in the spectral range of currently available quantum cascade laser (QCL). Then, we determined detection possibilities, appropriate experimental setup and a method for calculating concentration from measured transmittance spectra and built a high resolution open-path trace gases sensor at the CCNY (Quantum Cascade Laser Open-path System, QCLOPS-CCNY). We implemented the retrieval algorithms using a least squares fitting technique for all species simultaneously simulated, and derived H_2O, O_3 and NH_3 concentrations from open-path measurements. Finally, a part of the system design and field measurement results were compared to other observations, as appropriate or available, and several case studies of particular events were undertaken.

The major goal of this research is to develop a high resolution, high sensitivity QCL based open-path system (QCLOPS) for monitoring trace gases, such as O_3 and NH_3. Since the lasers and detectors, which are used in the system, are small in size (mm to cm range) and cooled thermoelectrically, a portable and continuous measurement system may be possible using this technology.

Thesis Outline

Chapter 2 introduces the theoretical background of the open-path QCL absorption spectroscopy. The chemical composition of the lower atmosphere will be discussed along with O_3 and NH_3's impacts on the climate change. Then, we discuss how the mid-infrared laser absorption spectroscopy techniques can be applied to retrieve concentrations of O_3 and NH_3. Two basic open-path systems, mono-static retroreflector system and backscattering system are introduced. This chapter will conclude with the structural engineering of the mid-infrared laser source, QCL and how it was designed to obtain a single frequency light source.

Chapter 3 deals with the characterization of the open-path O_3 and NH_3 simultaneous detection system (QCLOPS-CCNY). The implementation of a previously existing GENSPECT codes, and the development of Matlab codes to construct the frequency response of gases including broadening and individual retrieval process will be explained. The hardware design and constructing of the QCLOPS-CCNY including a Newtonian telescope, a system chassis and optical setup will be presented in this chapter. Moreover, the link power analysis, an open-path system model (OPSM), was applied to the system. The detail of these works will be explained in chapter 3.

Since the original implementation is not possible at present, we decided to test our model on a simpler system where the source is available and validations are possible. **Chapter 4** describes the 5.3μm QCLOPS and this system is able to measure water vapor concentration, which is important factor for weather prediction. Then, the results of the link power analysis for the 5.3μm QCLOPS will be compared with the field

measurements. The final part of this chapter will be the validation of the open-path system from preliminary measurement results with simulation model.

As our initial system designs include retroreflector and backscattering targets, we would like to analyze backscattering properties of building materials. **Chapter 5** presents laboratory measurements of backscattering from the urban building materials using 5.3 μm QCL and Fourier Transform Infrared spectrometer, FTIR.

Chapter 6 summarizes the main conclusions of this thesis and provides recommendations for the future work.

References

[1] http://www.citymayors.com/environment/polluted_uscities.html

[2] D. Liu, and B. Liptak, “Environmental Engineers’ Handbook”, CRC Press (1999)

[3] J. Renard, S. Calidonna, and M. Henley, “Fate of ammonia in the atmosphere - a review for applicability to hazardous releases”, J. of Hazardous Materials, B108, 29-60 (2004)

[4] US EPA, “Ground-level Ozone Standards Designations”, and “Ozone and your Health” at http://www.epa.gov/ozonedesignations/, and http://www.epa.gov/airnow//ozone-c.pdf

[5] http://www.mirthecenter.org/research.aspx

[6] V. Vladutescu, B. Gross, F. Moshary, S. Ahmed, “Assessment of a QCL Laser Approach for the Simultaneous Measurement of Ambient Ammonia and Ozone” SPIE Proceedings, 6760-6768 (2007)

[7] F. D'Amato, P. Mazzinghi, F. Castagnoli, "Methane analyzer based on TDL's for measurements in the lower stratosphere: design and laboratory tests", Appl. Phys. B75, 195-202 (2002)

[8] M. Lwin, “Evaluation of Quantum Cascade Laser Open-path Systems”, thesis proposal (2008)

CHAPTER 2: MID-INFRARED LASER ABSORPTION SPECTROSCOPY FOR TRACE GAS DETECTION

Trace-gas detection system provides the basic understanding of the chemical evolution of the atmosphere at various spatial and temporal scales. The mid-infrared region has stronger fundamental vibrational bands for most chemical substances compared to near infrared over tone bands [1] and trace gas detection based on the mid-infrared laser absorption spectroscopy is a most effective technique.

2.1. The Composition of the Atmosphere and Impacts of Ozone and Ammonia on Human Health

The abundance of a gas in the Earth's atmosphere can be measured in the fractional unit of mixing ratios by volume, which refers to the fractional volume of a given gas per unit volume of air. For example, the mixing ratios of molecular Nitrogen (N_2) and oxygen (O_2) in the dry atmosphere are 0.78 and 0.21, respectively, meaning that these two gases make up 99% of air [2]. Furthermore, it is the trace gases, which make up the remaining 1% of the atmosphere, and are responsible for such high-profile environmental problems such as global warming and urban smog. For example, near the Earth surface the average mixing ratios of ozone (O_3) is ~20 x 10^{-9} or 20 parts per billion per volume (ppbv) and the average mixing ratios of water vapor (H_2O) is ~0.01 (10^4 ppmv) .

The troposphere is where greenhouse gases such as water vapor (H_2O), carbon dioxide (CO_2), methane (CH_4), nitrous oxide (N_2O), sulfur hexafluoride (SF_6), and

chlorofluorocarbons (CFCs) enter the atmosphere and heat the earth by trapping additional IR radiation that would otherwise escape to space. The tropospheric O_3, which is the next most important greenhouse gas after H_2O, CO_2, and CH_4, is produced entirely via photochemistry. Ammonia (NH_3) in atmosphere reacts with sulfur trioxide (SO_3), which is product of oxidation of sulfur dioxide (SO_2), to form crystalline particles of sulfuric acid. The rapid reaction of NH_3 with acidic components (nitric acid, hydrochloric acid) leads the formation of coarse particle aerosols (size 10-100 μm) and ammonium salts, which are main components of smog aerosols [3]. While all of the above gases have some natural sources, the anthropogenic contributing to their concentration is large and the atmospheric abundances of these gases are continuing to increase.

The exposure to O_3 can damage respiratory systems, such as aggravate asthma, and cause to premature death in people with heart and lung disease. The Environmental Protection Agency set 8-hour O_3 exposure of the national ambient air quality standard (NAAQS) to 75 ppb for ground level ozone [5].

2.2. Mid-infrared Laser Absorption Spectroscopy

2.2.1. Rotational-vibrational Transitions of Molecules

The mid-infrared absorption spectra of molecules in the atmosphere are a result of simultaneous rotational and vibrational energy level transitions of these molecules. Such spectra present themselves as bands of absorption with fine structure, where the central frequency of the band is determined by the type of vibrational transition taking place (fundamental, first overtone, etc.) while the band structure itself is determined by the allowed rotational transitions for that particular vibrational transition [6].

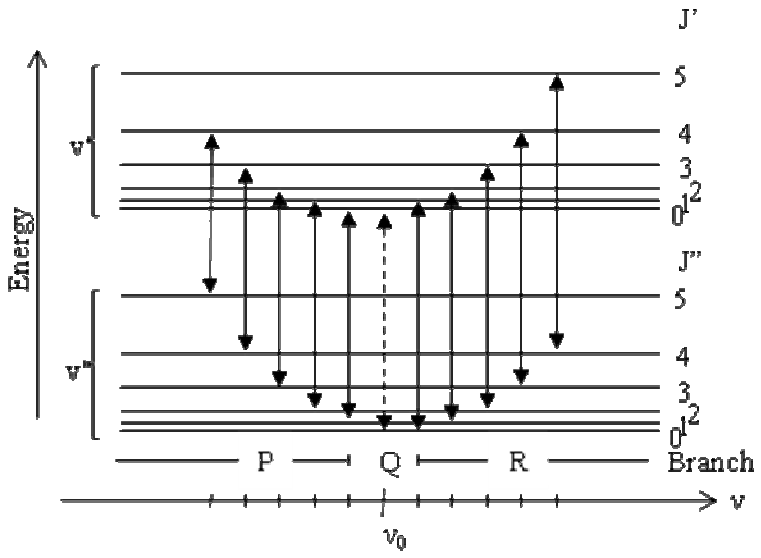

Figure 2.1: Relative positions of rotational-vibrational transitions in the absorption spectrum of a molecule where v and J are vibrational and rotational quantum numbers, v" has higher energy level than v'

The three branches of the resultant vibrational-rotational band shown in figure 2.1 are referred to as the P, Q and R branches, from left to right and they correspond to $\Delta J = -1$, $\Delta J = 0$ and $\Delta J = +1$, respectively. By convention, they are labeled as P1, P2, P3, ... and R0, R1, R2, ... away from the band center, with the numbers signifying the rotational quantum number in the lower vibrational state (J''). P0 does not appear because it would mean transitioning to a negative rotational quantum number in the higher vibrational state ($J' = -1$).

The intensity of an observed transition is proportional to the transition probability, the population and degeneracy of the initial energy state and the path length of the sample [6]. A molecule with N atoms has 3N degrees of freedom for its motion. Since two sets of three degrees of freedom are required to describe the translational and rotational motion of the center of mass of the molecule, this leaves 3N-6 degrees of freedom for vibration in the molecule (3N-5 for linear molecules since only two degrees of freedom are necessary to describe the rotational motion of the center of mass). Thus O_3 has three normal modes of vibration (v_1, v_2, v_3) while CO_2 (as a linear molecule) has four (but two of its bending modes are degenerate), and, furthermore, each normal mode is allowed its own set of overtone bands. Like rotational transitions, vibrational transitions are also only observed if the vibration causes a change in the dipole moment, e.g. the symmetric stretch of CO_2 (O=C=O) is infrared-inactive, and homonuclear molecules such as O_2 and N_2 still generally remain infrared-inactive [6].

Transitions from energy levels other than the ground state are known as hot bands because they only become significant at high temperatures when the populations of

higher energy levels increase [7]. The selection rules for simultaneous but independent rotational and vibrational transitions can be shown to be a combination of the selection rules for each transition.

2.2.1a. Ozone (O_3)

The O_3 molecule, composed from three oxygen atoms, in its electronic round state has an open isosceles triangular geometry with apex angle of 127˚ and two equal bonds with a length of 127.8 pm [8].

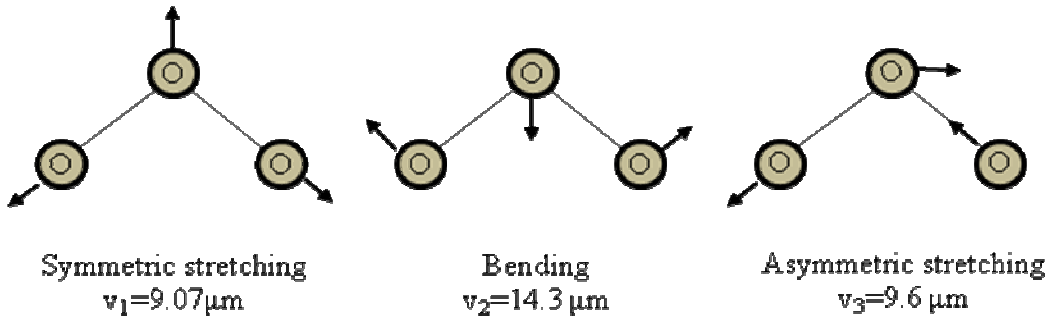

Figure 2.2: Fundamental vibrational modes of O_3 with its structures

The three normal modes of vibration ($v_1v_2v_3$) are all infrared active. Most common isotope ^{16}O ^{16}O ^{16}O has 99.28% abundancy of total isotopes and is important in atmospheric trace gas measurement. As shown in figure 2.3, the fundamental v_3 mode, which centered at 9.6 μm (1042.06 cm^{-1}) is the strongest among the fundamental modes (v_1 at 9.07μm (1103.14 cm^{-1}) and v_2 at 14.3 μm (700.93 cm^{-1})). The Q band ($\Delta J = 0$) is not allowed for O_3 at 1042.06 cm^{-1} band (asymmetric stretching mode and the two distinct branches of the resultant vibrational-rotational band shown in figure 2.3 (right) are referred to as the P and R branches, from left to right (also see figure 2.1).

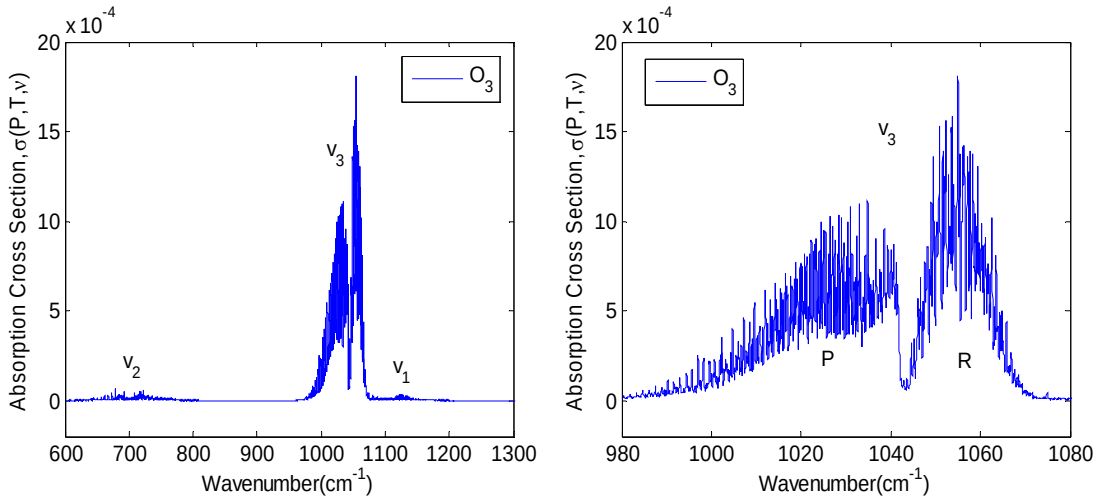

Figure 2.3: Absorption cross section of the symmetric stretching mode (v_1), bending mode (v_2) and asymmetric stretching mode (v_3) of O_3 in atmospheric pressure and temperature (left) and the close up view of strongest v_3 band showing P and R branches (right) [generated using GENSPECT simulation with HITRAN data]

2.2.1b. Ammonia (NH_3)

Ammonia has four infrared active fundamental modes: 1) symmetric bending and stretching mode (v_1) at 3335.9 and 3337.5 cm^{-1}, 2) asymmetric bending mode (v_3) at 3414 cm^{-1}; 3) strong (v_2) band at 931.58 and 968.08 cm^{-1} and 4) asymmetric stretching mode (v_4) at 1627.5 cm^{-1} [7]. The absorption cross sections of these four vibrational modes are shown in figure 2.4.

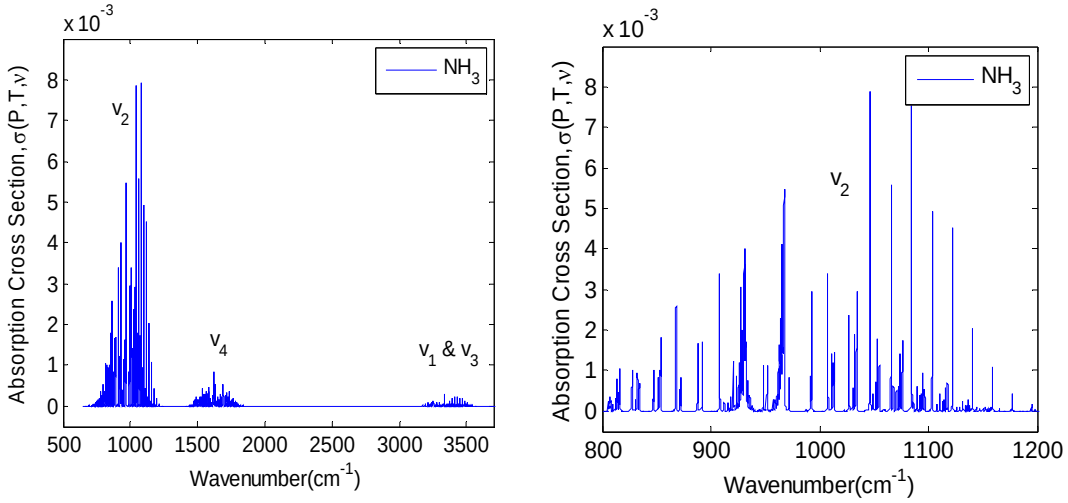

Figure 2.4: Absorption cross section of the fundamental vibrational modes, v_1, v_2, v_3, and v_4 of NH_3 in atmospheric pressure and temperature (left) and the close up view of strongest v_2 band (right) [generated using GENSPECT simulation with HITRAN data]

2.2.2. Transition Line Strength and Shape

The strength $S(v_0, T)$ [$cm^{-1}/(molec \cdot cm^{-2}) = cm \cdot molec^{-1}$] of an absorption line with a central frequency v_0 [cm^{-1}] (distinguished from the vibrational quantum number by the bar) in a rotational-vibrational band and at temperature T [K] is given by equation 2.1 [9].

$$S(v_0, T) = S(v_0, T_0) \frac{Q(T_0) \exp\left(-\frac{E''}{kT}\right)\left(1 - \exp\left(-\frac{hcv_0}{kT}\right)\right)}{Q(T) \exp\left(-\frac{E''}{kT_0}\right)\left(1 - \exp\left(-\frac{hcv_0}{kT_0}\right)\right)} \qquad (2.1)$$

where T_0 is a reference temperature of 296 K, Q is the partition function, E″ is the lower state energy of the transition, h is the Planck constant, c is the speed of light, and k is the

Boltzmann constant. The sensitivity of equation 2.1 to temperature is strongly influenced by E″.

The rotational-vibrational transition lines are broadened by two underlying mechanical processes: Lorentz broadening or pressure broadening and Doppler broadening. The pressure broadening occurs when gas molecules collide strongly with one another, which randomizes the time-domain phase of the simple harmonic oscillator (SHO) radiation emitted by the molecules. Since the Fourier transform of a truncated SHO emission is a sinc function a single truncated SHO emission will appear as a sinc function in the spectral domain. In the limit of many simultaneous truncated emissions and many molecules, the resultant superposition of sinc functions can be shown to reduce to the Lorentzian functional form

$$f(\nu - \nu_0) = \frac{1}{\pi} \frac{\gamma_L}{(\nu - \nu_0 - \delta_L)^2 + {\gamma_L}^2} \tag{2.2}$$

where

$$\gamma_L(T, p) = \left(\frac{T_0}{T}\right)^{n_{air}} [\gamma_{air}(T_0, p_0)(p - p_s)\gamma_{self}(T_0, p_0)p_s] \tag{2.3}$$

The pressure-dependent shift of the line center frequency, $\delta_L = \delta_{airp}$, is introduced in Equation 2.2 to account for the failure of the strong collision approximation at high pressures, where p is the pressure and δ_{air} is the coefficient of the air-broadened pressure shift [$cm^{-1} \cdot atm^{-1}$] measured at a reference temperature and pressure (T_0 = 296 K, P_0 = 1 atm). δ_L has a temperature dependence of the same form as γ_L, and n_{air} is used in the absence of other information. The Half-Width at Half-Maximum (HWHM) of the

Lorentzian, γ_L [cm^{-1}], is calculated according to Equation 2.3 given the different self and air-broadening coefficients γ_{air} and γ_{self} [$cm^{-1} \cdot atm^{-1}$], which are also measured at T_0 = 296 K and P_0 = 1 atm, the partial pressure of the gas, P_s, and the exponent of the temperature dependence of the broadening coefficients, n_{air}. Equation 2.3 assumes one temperature dependence for both the self- and air-broadening processes in the absence of other information (n_{air} takes on different values depending on the nature of the colliding partners and the particular transition).

Doppler broadening occurs when the mean free path of the gas molecules is large enough to allow their velocities to become high and Maxwell-Boltzmann-distributed. This leads to a smearing out of the absorption coefficient through the lineshape function which now has the Gaussian form of Equation 2.5, where M is the molecular mass and the HWHM is equal to √ln2γD [cm−1].

$$f(v - v_0) = \frac{1}{\sqrt{\pi}\gamma_D} \exp\left(\frac{(v - v_0)^2}{\gamma_D^2}\right) \tag{2.4}$$

where

$$\gamma_D(T) = \sqrt{\frac{2kT}{M}} \frac{v_0}{c} \tag{2.5}$$

The Doppler broadening linewidth does not vary significantly throughout the atmosphere since it is not dependent on pressure but on square root of temperature. It becomes much bigger than the Lorentz broadening halfwidth in the upper stratosphere and above, where the mean free path is large. Finally, the Doppler broadening halfwidth is reduced as the mean free path decreases with increasing pressure in a process referred to as collisional or Dicke narrowing [9]. Although this is a second-order effect compared

to Lorentz broadening in the troposphere, it is of some consequence in the stratosphere, where such small changes in the Doppler halfwidth are not obscured by the rapidly decreasing Lorentz halfwidth [9].

Since both broadening processes (Pressure and Doppler broadening) are important, in the case throughout the stratosphere, the Voigt line shape function is used as

$$f(x,y) = \frac{1}{\gamma_D}\frac{y}{\pi^{3/2}}\int_{-\infty}^{\infty}\frac{\exp(-t^2)}{(x-t)^2+y^2}dt \qquad (2.6)$$

where $x = (v - v_0)/\gamma_D$ and $y = \gamma_L/\gamma_D$. Equation 2.6 can be shown to be the convolution of the pressure (Lorentz profile) and Doppler (Gaussian function) line shape functions [9]. Collisional (Dicke) narrowing and collisional line-mixing are not usually accounted for in the Voigt formulation. Collisional line mixing refers to the case when neighbouring transitions cannot be considered independent of one another because the wings of the absorption features now overlap, as is the case under typical atmospheric pressures found at the surface. In collisional line mixing, the band strength is not altered, but rather it is redistributed as a function of frequency. The Voigt profile is used to represent absorption line shapes in the GENSPECT algorithm described in detail in chapter 3.

2.2.3. HITRAN Spectral Database

The HITRAN (HIgh Resolution TRANsmission) database is a research-standard database containing reference temperature and pressure line strengths ($S(v_0)$) and pressure broadening and shift parameters (γ_{air}, γ_{self} , δ_{air}, along with their temperature dependence exponent n_{air}) for the vibrational-rotational transitions of the 39 most

common atmospheric molecules. The database also contains lower state energy (E″) information necessary for the line strength calculation and several other quantum mechanical parameters.

HITRAN 1996 [10], HITRAN 2000 and 2001 [11], as well as HITRAN 2004 [12] exist concurrently, and new, more accurate measurements are continuously being compiled for future updates of the database. In addition to line-by-line parameters, cross-section data and aerosol indices of refraction are also included for some species in some pressure, temperature and wavenumber ranges.

2.3. Quantitative Analysis

The great advantage in speed that mid-infrared spectroscopy for quantitative analysis will greatly increase its popularity in the future. However, in order for mid-infrared spectroscopy to realize in full potential as a quantitative tool, it must be capable of handling problems encountered in many real samples.

2.3.1 The Retrieval Method of the OPQCLS

This section explains the retrieval method that we used to calculate the concentration of target gases from a measurement spectrum of an open-path system. The retrieval method has to meet the following requirements:

1. Multi-species detection
2. Spectral baseline correction

3. Fast and efficient programming implementation (for example, Matlab program), so that large amount of data can be collected in short intervals with high repetition rate.

The method has two main parts. The first is to generate a reference absorbance spectrum of known concentrations of target gases and other contaminating gases for the same atmospheric conditions (temperature and pressure) as those occurring during the measurement time. The second part includes the measurement of the absorbance spectrum which can be found as the negative logarithm of the transmission. Given the total measurement absorption and the theoretical spectra of each gas component, we can calculate the sample concentration of all target gases using linear least squares analysis as shown in figure 2.5.

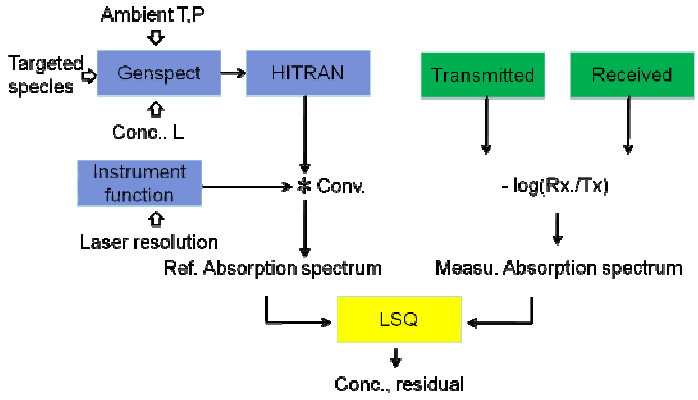

Figure 2.5: A block diagram of the retrieval method

The theoretical aspects of the relationship between absorbance and concentration of a gas and how we applied least squares analysis in the method are explained in detail.

2.3.2. Program Functions

Initially we assume that Beer's law is valid.

$$A(v) = \alpha(v).L.C \tag{2.7}$$

where A is absorbance at a given frequency, 'α' is frequency dependent absorptivity, 'L' is path length and 'C' is concentration. For multi-component sample we have each frequency 'i' in the spectrum.

$$A_i = \sum_{j=1}^{m} K_{ij} C_j + e_i \tag{2.8}$$

The K_{ij} terms represent the product of path length and absorptivity for species j at frequency i. The e_i terms are the random error in the measurement spectrum. The error is assumed to be normally distributed with a mean value of zero. The full spectrum then becomes a series of i equations where i is the number of frequency step. For example, 'i' will be 100 as we measure $1cm^{-1}$ window with $0.01cm^{-1}$ resolution. To account for possible scale parameters, we include a constant column attenuation into the model to fit. Therefore, equation 2.8 can be written with the baseline function as:

$$A_i = C_0 + \sum_{j=1}^{m} K_{ij} C_j \tag{2.9}$$

or combined in matrix representation

$$A_{(i,1)} = K_{(i,j+1)} C_{(j+1,1)} + e_{(i,1)} \tag{2.10}$$

where A is an (i x 1) matrix whose columns represent the spectrum of mixed compound absorbance at i^{th} frequency, and K can be written as

$$K = \begin{bmatrix} 1 & K_{11} & K_{12} & \cdots & K_{1j} \\ & \vdots & \vdots & \vdots & \vdots \\ 1 & K_{i1} & K_{i2} & \cdots & K_{ij} \end{bmatrix} \tag{2.11}$$

C is the (j+1) x 1 matrix of the ratio of sample and reference concentrations and e is the i x 1 matrix of random measurement errors in the spectra

The linear least squares (LSQ) solution [14, 15] is given as

$$C = (K^T K)^{-1} K^T A \tag{2.12}$$

Here, C is a matrix of coefficient values so that we can obtain concentrations of the j gases by taking the elements [j+1]. The value of the uncertainty or the variance of each species can be calculated from the diagonal matrix. [15]

$$\sigma^2(j) = j^{th} \text{ diagonal value of } (K^T K)^{-1} \times \sigma^2_{noise} \tag{2.13}$$

where σ^2_{noise} is the variance of the measurements which can be estimated from the residuals of the spectrum fit.

To simplify the calculation of the absorption spectrum over the extremely complex line information from the HITRAN database, we use the GENSPECT program, which collects all line-by-line data from the HITRAN database [13], to calculate monochromatic spectrum and then, convolute it with the instrument function to obtain reference absorbance spectrum. The left side of figure 2.5 describes the process to generate reference spectrum using GENSPECT and HITRAN database.

The linewidth (or instrument function) was ultimately based on the frequency chirp and will be explained in detail in chapter 3.

2.4 QCL based Open-path Trace Gas Sensor System

The QCL is an attractive source for atmosphere trace gases detection because it can operate in two atmospheric windows (3-5 μm and 8-13 μm) where the atmosphere is relatively transparent due to a lack of water vapor absorption. Single mode mid-IR coherence laser emission, tunability, and sufficient power to obtain a signal-to-noise ratio are advantages the QCL has for this application. Moreover, recent development of QCL allows it to operate in room temperature in pulsed and continuous wave (CW) modes so that they can be used in field deployable devices.

2.4.1 Mono-static Retroreflector and Backscattering Systems

The major parts of the designs in open-path sensor instrument include the transmitting light source, the receiving telescope, electronics control components and data acquisition system. We design our system as a mono-static system which means that the light source and collecting telescope are on one side and a reflecting object is the other side. The path-length is defined as the full round trip distance between the transmitter and the receiver.

Figure 2.6 shows the major components of a mono-static retroreflector system. The incident beam is reflected back by the retro-reflector and then part of reflected signal is collected by the receiving telescope. From the detected light signal of the reflected beam, the data acquisition system should ultimately derive the concentration levels for selected pollutants integrated along the optical path. On the other hand, if we do not have the means to have a separate retroreflector, we may try to use other as illustrated in figure 2.7, e.g.: barns, fields, bridges, chimneystack, or intersection.

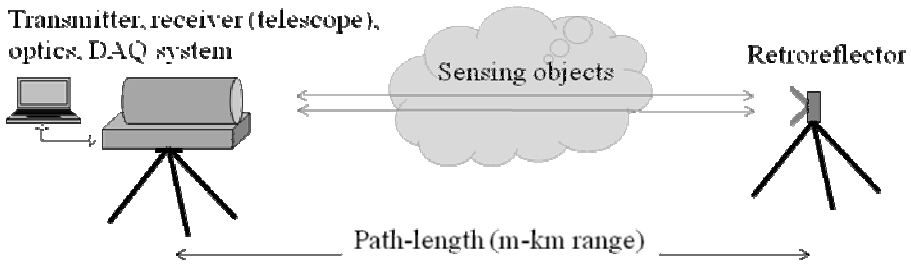

Figure 2.6: Schematic of monostatic open-path trace gas detection system using a retroreflector

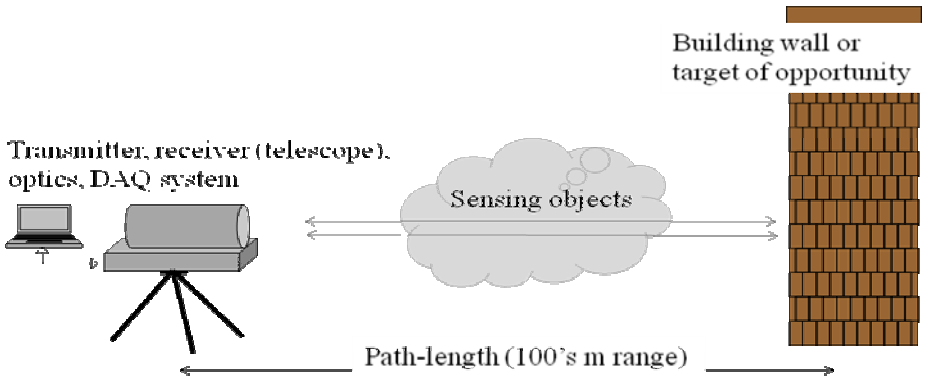

Figure 2.7: Schematic of monostatic open-path backscattering system

2.4.2 Quantum Cascade Lasers

The quantum cascade laser (QCL) was proposed by R.F. Kazarinov and R.A. Suris in 1971 that electromagnetic waves could be amplified in a semiconductor with a superlattice, material with periodically alternating layers of several substances. In 1994, scientists at Bell Laboratories demonstrated the first working QCL that used the quantized electronic states in a multiple quantum well structure for optical amplification. Some advantages of QCL include:

1. Tunability: QCL can be tuned frequencies externally by changing laser chip temperature and tuning range can be > 100 cm^{-1} with the external cavity.
2. Output power: QCL emits higher output power than lead-salt diode laser's (LSD) which also produces mid-IR light. (QCL: 2 – 20 mW, LSD: 0.1 – 0.5 mW) [1]
3. Operating temperature: pulsed or continuous wave (CW) QCL can be operated at room temperature or TE cooled temperature.
4. Size: QCL is typically mm size.

2.4.2a. Technology

The QCL is a semiconductor laser that emits coherent light in mid- to far infrared regions (3-250 μm) through the use of intersubband transitions in a repeated stack of semiconductor superlattices. Its capabilities, such as compact, high brightness mid-infrared coherence light source with tunability, room temperature operation, fulfill requirements in the applications of highly sensitive trace gas detection [1].

2.4.2b. Band Structure Design

QCLs are fundamentally different from conventional interband semiconductor lasers, which use active-region materials with suitable bandgaps for the emitted laser wavelengths.

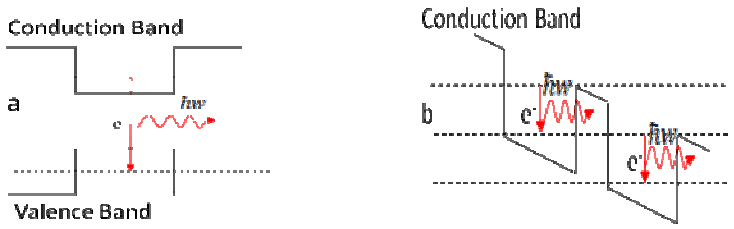

Figure 2.8: a) Interband transitions in conventional semiconductor lasers emit a single photon. b) In quantum cascade structures, electrons undergo intersubband transitions and photons are emitted. The electrons tunnel to the next period of the structure and the process repeats.

The wavelengths of QCL can be tailored by choosing the thickness of the materials in the active region but the composition of those materials does not have to change at all. For example, QCLs using active region layers of Indium Aluminum Arsenide (InAlAs) and Indium Gallium Arsenide (InGaAs) with lattice matched to an Indium Phosphate (InP) substrate and having suitable thickness for desired wavelength, have demonstrated emission wavelengths from 4 to 24 μm [16].

Optical transitions of the QCL do not occur in a bandgap (between conduction band and valence band) but in discrete electronics states in conduction bands (figure 2.8 b.). These states arise from quantization of electronics motion in nano-meter thick active

region layers. These layers are called quantum wells. Adjusting width and shape of quantum well, energy level difference can be designed and it emits light with desired wavelengths [17].

QCLs are fabricated by Molecular Beam Epitaxy (MBE) technology by depositing thin films at the thickness of a molecular layer can be done with MBE. Designs in intersubband structure and MBE technique are the main tools in developing QCLs that satisfy design criteria.

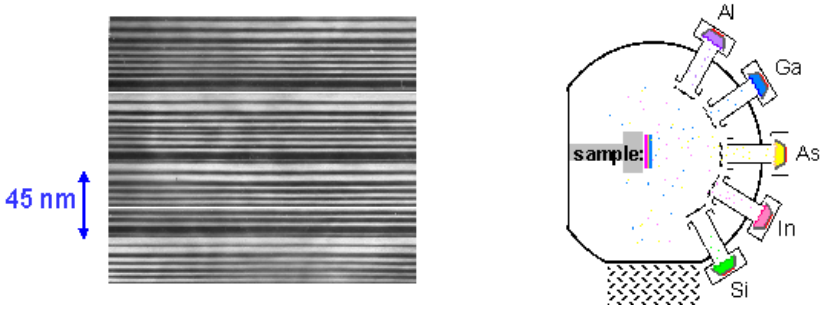

Figure 2.9: Micrograph of a cross section of a QCL with several stages of active and injector layers and MBE process [18]

The figure below shows the conduction band edge (black line) of the quantum-cascade structure that has a slope because of the electric field (10's-100's kV/cm). It is an energy diagram of three-level laser in which electrons are injected from left to right [18]. An electron is injected into adjacent identical active region after emitting a laser photon and each electron creates 'n' laser photons in traversing an n-stage cascade structure, thus the number of active region-injector stages of a QCL defines output power of the laser. These cascading emission of photons are achieved by alternating doped electron injector regions with active regions.

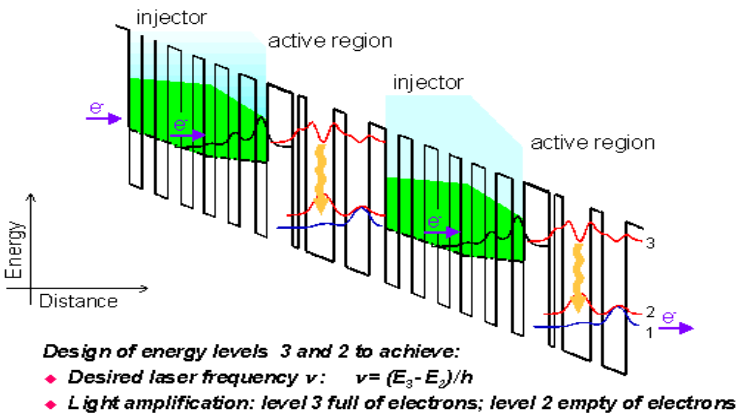

Figure 2.10: Scheme of convention band energy diagram of two QCL active regions based on a three-well vertical transition mechanism. The laser transition is indicated by the vertical arrows and the electron flow by the horizontal arrows [18].

Injector regions have been considered as an essential requirement for laser action in QC lasers. Like the active region, the electron injectors are also composed of quantum wells coupled by very thin barriers. Because of this superlattice structure, electronics states extend over many layers and form narrow energy minibands. In the active sections the photons are generated, while the miniband in the injector regions enables the transfer of the electrons from the lower levels of one active section into the upper level of the next section. By careful selection of material composition and thickness of each layer in the device, and the applied external electric field, an electric subband minimum in a given period of the device may be aligned with a higher energy subband minimum in the adjacent period.

An electron may take part in an optical transition between electronic subbands in an active region before tunneling into the next period of the structure and performing another optical transition. The thinnest well in the active region enhances tunneling of

the electrons from the injector into the upper state. The coupling of the two QWs (with difference QW width) produces three energy levels. The lasing will be due to the transition from level 3 to level 2 and the additional level 1 which is close in energy to level 2 will be the means to empty level 2 by phonon scattering. The depopulation process will ensure population inversion, as needed for lasing, and the electrons will keep moving through the device, giving high optical power output.

To prevent accumulation of electrons in level 1, the exit barrier of the active region is made thin, which allows rapid tunnelling into a miniband in the adjacent injector. The miniband allows the electrons to rapidly cross the injector and quickly relax the ground state, then, reinject into the next active region. Injector regions are n-typed doped, but the active regions are generally undoped to minimize broadening of the gain spectrum that would lead to large threshold current [19]. The laser can be designed for different wavelengths by choosing various nanometers layer thickness. High-performance 10.16 um high power low threshold QCL was reported by Hofstetter and et., al [20].

In a QCL, the mentioned quantum well structure is embedded in a waveguide (a spatially inhomogeneous structure for guiding light, i.e. for restricting the spatial region in which light can propagate). The laser resonator is most often a distributed Bragg reflector (DBR), where the laser resonator is made with at least one DBR outside the gain medium (the active region), or a distributed feedback (DFB) type, where the whole resonator consists of a periodic structure providing distributed in the wavelength range of laser action containing the gain medium.

Currently, the single mode RT or TE cooled DFB pulsed QCLs can be available from 844 to 2350 cm^{-1} with 2-20 mW average output power from the Alpes Lasers SA of Neuchâtel, Switzerland, which is the leading commercial manufacturer of quantum cascade lasers [21].

References

[1] F. Tittel, D. Richter, and A. Fried, "Mid-Infrared Laser Applications in Spectroscopy", Appl. Phys. **89**, 445-516 (2003)

[2] G. Stephens, "Remote Sensing of the Lower Atmosphere", Oxford University Press, New York (1994)

[3] J. Renard, S. Calidonna, and M. Henley, "Fate of ammonia in the atmosphere - a review for applicability to hazardous releases", J. of Hazardous Materials, B108, 29-60 (2004)

[4] http://www.osha.gov/dts/chemicalsampling/data/CH_218300.html

[5] US EPA, "Ground-level Ozone Standards Designations": http://www.epa.gov/ozonedesignations/

[6] J. M. Hollas, "Modern Spectroscopy", 4th ed., John Wiley & Sons, Inc., New Jersey (2004)

[7] G. Herzberg, "Molecular Spectra and Molecular Structure II: Infrared and Raman Spectra of Polyatomic Molecules", 7th printing, D. Van Nostrand Company, Inc., New Jersey (1956)

[8] R. M. Goody and Y. L. Yung, "Atmospheric Radiation: Theoretical Basis", Oxford University Press, New York (1989).

[9] G. Petty, "A First Course In Atmospheric Radiation", 2nd Ed., Sundog Publishing, Madison, WI (2006)

[10] L. S. Rothman, et al., "The HITRAN molecular spectroscopic database and HAWKS (HITRAN AtmosphericWorkstation): 1996 edition", J. Quant. Spectrosc. Radiat. Transfer, 60, 665–710 (1998)

[11] L. S. Rothman, et al., "The HITRAN molecular spectroscopic database: edition of 2000 including updates through 2001", J. Quant. Spectrosc. Radiat. Transfer, 82, 5–44 (2003)

[12] L. S. Rothman, et al., "The HITRAN 2004 molecular spectroscopic database", J. Quant. Spectrosc. Radiat. Transfer, 96, 139–204 (2005)

[13] B. M. Quine, J. R. Drummond, "GENSPECT: a line-by-line code with selectable interpolation error tolerance", Journal of Quantitative Spectroscopy & Radiative Transfer (74), 147-165 (2002)

[14] D. Haaland, and R. Easterling, "Application of New Least-squares Methods for the Quantitative Infrared Analysis of Multicomponent Samples" Appl. Spec. vol. 36, 665-673 (1982)

[15] S. Chapra, and R. Canale, "Numerical Methods for Engineers", 6th ed., McGraw-Hill Higher Education, Boston (2010)

[16] A. Kosterev and F. Tittel, "Chemical Sensors Based on Quantum Cascade Lasers" IEEE JQE vol. 38, no. 6, 582-591 (2002)

[17] R. Pierret, "Advanced Semiconductor Fundamentals" vol 6, 2nd ed. Prentice Hall, NJ (2003)

[18] Bell Labs technical information at http://www.bell_labs.com/org/physicalsciences/psr/qc/index.html

[19] J. Faist, F. Capasso, C. Sirtori, D. Sivco, A. Hutchinson, S. Chu, and A. Cho, "Narrowing of the Intersubband electroluminescent Spectrum in Coupled-Quantum-Well Hetrostructures" Appl. Phys. Lett., vol. 65, 94-96 (1994)

[20] D. Hofstetter, J. Faist, M. Beck and A. Muller, "Demonstration of high-performance 10.16 mm quantum cascade distributed feedback lasers fabricated without epitaxial regrowth" Appl. Phys. Lett. vol. 75 no.5, 665-667 (1999)

[21] DFB Pulsed Room-Temperature lasers at http://www.alpeslasers.com/lasers-on-stock/index.html

CHAPTER 3: CHARACTERIZATIONS OF THE QCLOPS DESIGN

The first challenge in the spectroscopic measurement is to identify a section of spectral ranges in which all of the species of interest have transitions that have comparable absorption paths with unavoidable interfering gases within the laser's tuning range. Once this is understood, all system components are analyzed to optimize the sensitivity of the system, and to achieve other system requirements; such as portability and continuous operation. Knowing where the limitations of performance and which components must be improved is crucial to obtaining repeatable and accurate results. This chapter that contains - the theoretical evaluation of the designed open-path system using the link power analysis that includes the characteristics of the atmospheric medium, optical transmitter, remote target and receiver.

3.1. Spectral Window Searching for Ozone and Ammonia Simultaneous Detection

Because the turning limit of the DFB-QCL is 2-5 cm^{-1}, we need to find the optimal window, which will result in the smallest retrieval error for both O_3 and NH_3 simultaneously. First, using HITRAN 2000 database and GENSPECT matlab tool box [1, 2, 3], we calculated synthetic, normalized transmission spectra for O_3 and NH_3 together with the interference gases- H_2O and CO_2 in the 950 – 1100 cm^{-1} region under standard temperature and pressure (297K, 1atm). The resolution limited spectrum was calculated by convolution of the absorption spectrum with the laser resolution of the chirp ($0.018cm^{-1}$ @ 25˚C, 2% duty cycle pulse) dependent Gaussian instrument function [3]. The effective line width of the system was measured in the lab and can be found in detail in

the chapter 4. We assumed that the noise to be uncorrelated White Gaussian Noise for the system [4]. The ambient concentrations of an urban environment (H_2O = 1 x 10^4 ppm, CO_2 = 370 ppm, O_3 = 20 ppb and NH_3 = 3 ppb) were used in this analysis.

We set laser output power, P_0 = 250mW (5mW average with 2% duty cycle) which was multiplied with the resolution limited transmission spectrum, S_j (j for each gas) as shown in equation 3.1.

$$P_T(\nu_i) = P_0 \prod_j S_j(\nu_i) \tag{3.1}$$

where $P_T(\nu_i)$ is received spectrum at each wavelength of (ν_i) without noise features. We then added different noise levels, which is related to the SNR, to the spectrum $P_T(\nu)$ and obtained noise corrupted signal, $P_{T'}(\nu)$.

$$P_T(\nu_i) = P_T(\nu_i)\left[1 + \left\{\frac{1}{SNR}\right\}\varepsilon_i\right] \tag{3.2}$$

where ε_i was the Gaussian random noise with zero mean and unit variance. From these noise corrupted signals we calculate the concentrations O_3 and NH_3 from $P_{T'}(\nu)$ using linear least squares method which was explained in chapter 2.3.2. Then, the fractional error (% accuracy) was defined as

$$Fractional\ error = \frac{\sigma(C_j)}{\sigma_j^0} \times 100 \tag{3.3}$$

Figure 3.1 which plots the minimum SNR needed for retrieval accuracy for each gas component shows that the minimum required SNR to obtain 1% accuracy measurement over the global band occurs in the 1045-1050 cm^{-1} micro-window. A more reined plot finds the true optimal window to be 1045-1047 cm^{-1} spectral window. In this

window, the required SNR for NH_3 and O_3 are ~$4x10^3$ and ~$8x10^3$ respectively for the 1km path-length measurement (figure 3.2).

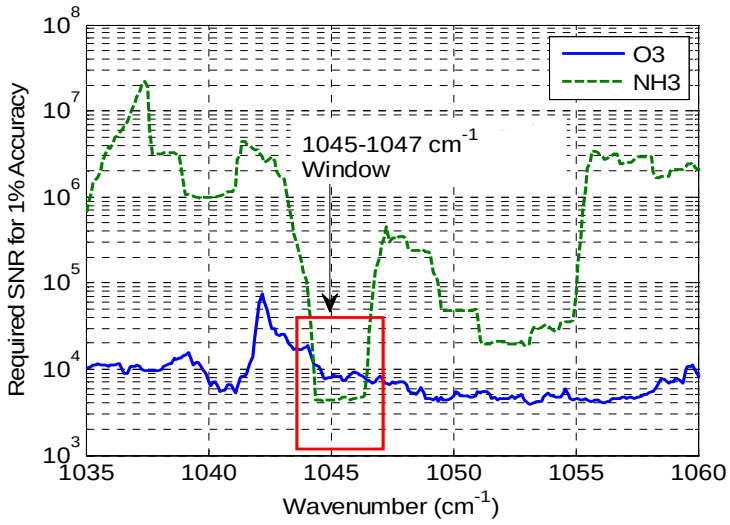

Figure 3.1: Theoretical result of optimum micro-window that requires minimum SNR for O_3 and NH_3 to obtain 1% accuracy measurement.

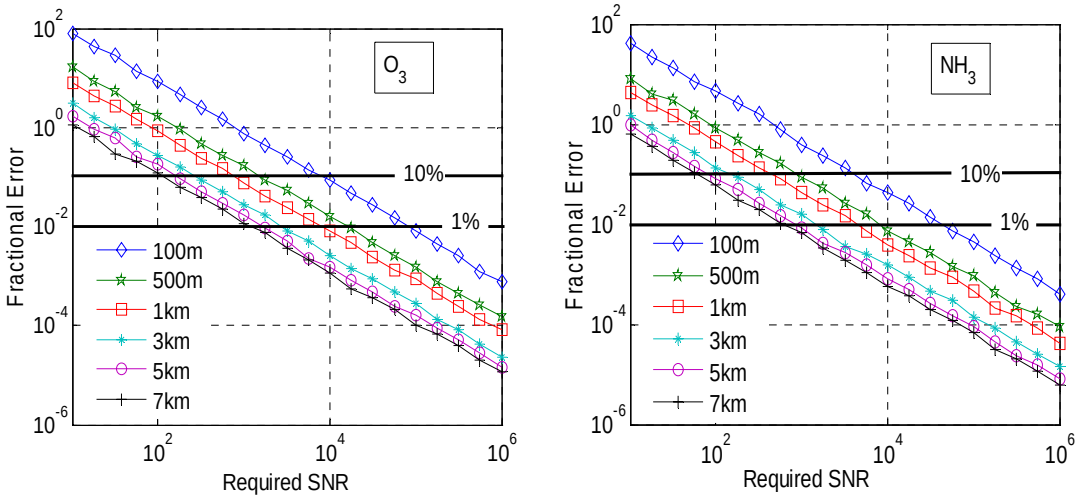

Figure 3.2: Required SNR with retrieval error (generated using the GENSPECT codes and HITRAN database)

The theoretical required SNR for the 1% and 10% accuracy measurements decreases with the path-length as shown in figure 3.2.

3.2 System Components

The main hardware components of the system are the DFB QCL *(*DQ9-M784I from Maxion Technologies, Inc), the laser driver system (LS-03-D from Cascade Technologies), the thermoelectrically cooled IR detector (PVI-3TE-10.6 from Vigo Systems), the pre-amplifier (Perry 481-200X from the Boston Electronics), and the 20.32 cm (8") Newtonian telescope with a light weight system body. The parameters of the relevant system components are listed in table 3.1.

Components	Value
DFB QCL	P_{out} = 200mW peak, 2% duty cycle Frequency range = 1045-1047 cm^{-1} Beam diameter = 4cm, beam divergence=0.4 mrad
IR Detector	D^* = 4.4x10^9 Jones($cmHz^{1/2}$/W) Rise time = 1ns (Δf=160MHz) Surface area = 1mmx1mm (2.56 mm^2 w/ lens) Responsivity = 1 A/W, Noise = 32 $pA/Hz^{1/2}$
Pre amplifier	Noise = 1.6 $nV/Hz^{1/2}$, Gain = 20
DAQ system	Rate = 2.5 GS/s, 8-bit, SINAD = 48 dB
Telescope	Diameter = 20.32 cm (8" primary), 5.7 cm (2.25" secondary), retroreflector diameter = 12.7 cm(5") F# (primary) = 3.69

Table 3.1: Main system components, QCL, detector and telescope parameters of the QCLOPS

3.2.1. The Quantum Cascade Laser and Controller Module

The QCL used in the QCLOPS was obtained from Maxion Technologies, Maryland U.S.A. Maxion provides a single mode DFB laser chip with side mode suppression larger than 20dB and frequency tuning range 1-5 cm^{-1} by the temperature or current changing on the laser chip [5]. The QCL chip was installed in the laser module made by Cascade Technologies, and the integrated system provided useful functionality of the laser including [6]:

a. Ease of use
b. Temperature control with integrated TE cooler and air cooling (-30˚C to 50˚C), and real time temperature monitoring
c. Easy control on operating voltage (0 to 48V), pulse width (20 to 10,000 ns) and pulse repeating rate (up to 5 MHz)
d. USB interface to control with a computer
e. Trigger out port and external trigger in port to synchronize with other components, such as detector or lock-in amplifier
f. Collimated laser output and integral tip/tilt adjustment for precision alignment

Figure 3.3 shows photos of DFB QCL chip in NS mounting, QCL module and Laser control module [5, 6].

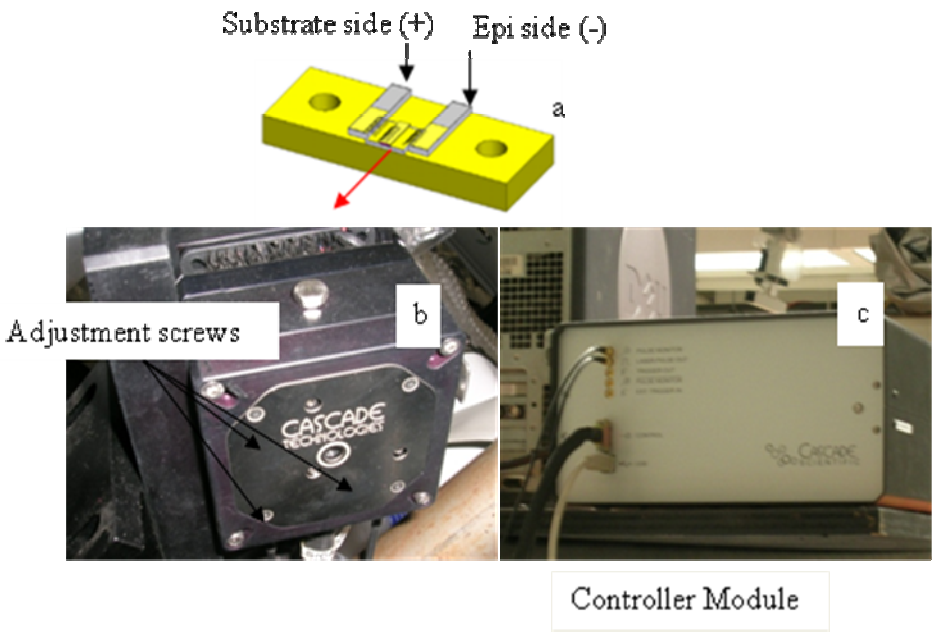

Figure 3.3: a) QCL on SN mounting, b) Cascade QCL module, and c) Cascade QCL controller module

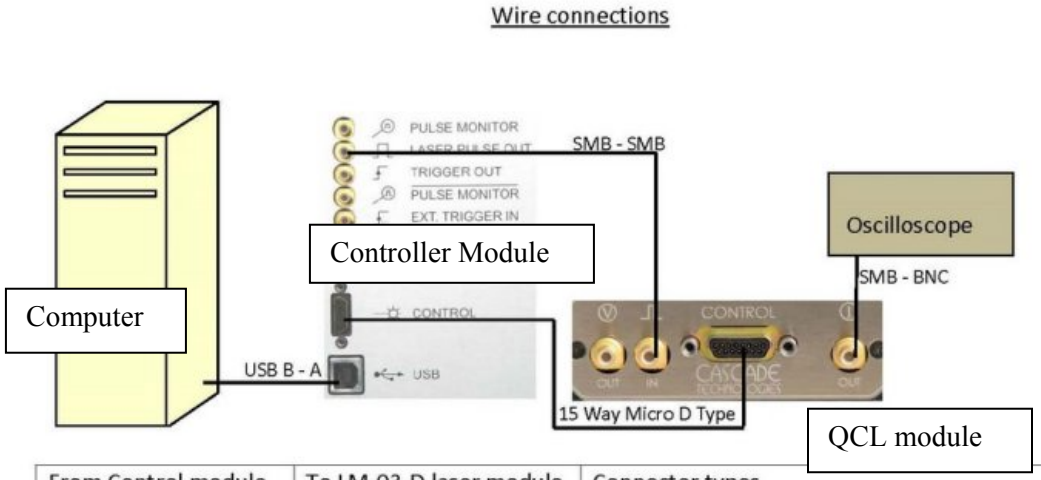

From Control module	To LM-03-D laser module	Connector types
Control	Control	15 Way Micro D type
Laser pulse out	Pulse in	SMB - SMB
USB to USB in PC		USB B-A
	I – out to Oscilloscope	SMB - BNC

Figure 3.4: Interface connections among QCL module, laser controller module and computer

3.2.1a Characterization of the QCL, DQ9-M784I from Maxion Technologies, Inc

We tested the laser in two conditions: 1.) T_{laser} = 35˚C, and 2.) T_{laser} = 10˚C with following components using a MCT IR detector (PVM 10.6-RT from Vigo System, Responsivity ≥ 0.1 Vmm/W) and the laser controller (LS-03-D from Cascade Technologies).

1. Laser Temperature 35˚C, Pulse width = 1000ns, Frequency = 50 kHz

Applied Voltage at laser controller(V)	Current on the laser chip(mA)	Output voltage(mV)
9	300	.01
10	350	0.40
11	450	0.75
12	570	1.10
12.5	600	1.20
13	620	1.30

Table 3.2: Applied voltage, current on the laser chip and output power of DQ9-M784I QCL when laser temperature is 35˚C

We measured applied current on the laser chip and emitted power of the laser with various input voltages. We did not see any output signal until the supplied voltage reached 9V. Measurements were taken with output voltages of 9, 10, 11, 12, 12.5, and 13V. The measurement results were plotted in figure 3.5 and figure 3.6.

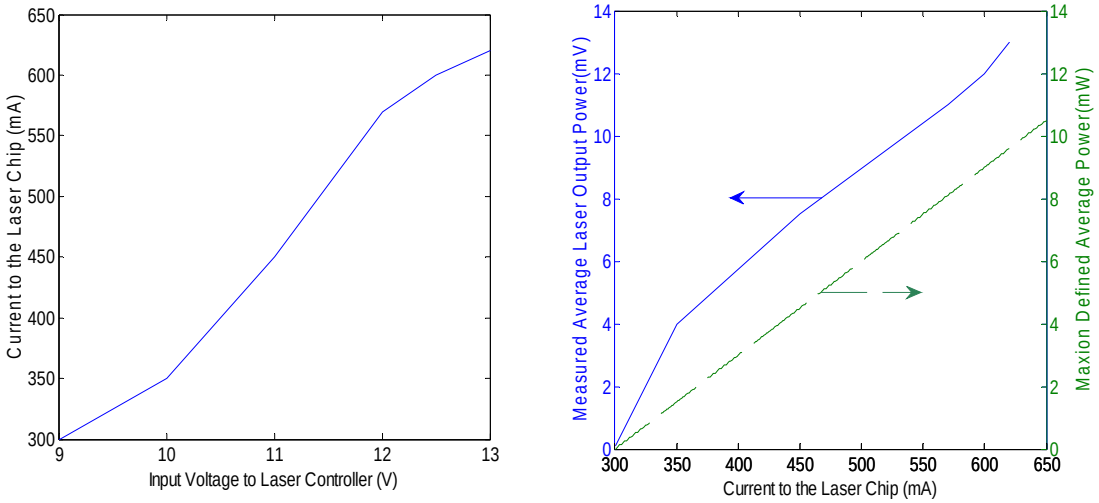

Figure 3.5: Applied voltage to laser controller and effected current on the laser chip (left) and comparison of measurement and data provided by manufacture (right)

According to measurement data, threshold voltage is 9V (300mA) and the laser's emitted power is 12mW when the applied voltage is 12.5V. We also took measurements with a lower temperature for our experimental reference.

2. Laser Temperature 10˚C, Pulse width = 200 ns, Frequency = 100 kHz

Applied Voltage at laser controller(V)	Current on the laser chip (mA)	Output voltage(mV)
9	300	.05
10	375	0.6
11	450	1.1
12	600	1.6
13	700	2.0

Table 3.3: Applied voltage, current on the laser chip and output power of DQ9-M784I QCL when laser temperature is 10˚C

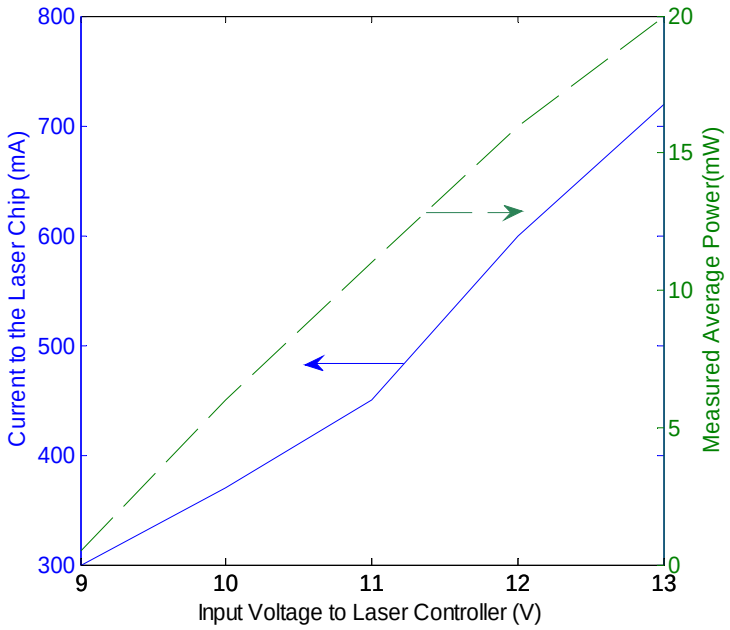

Figure 3.6: Current on the laser chip and emitted average power as a function of applied voltage in 10˚C operating temperature

In conclusion, this QCL produced the average output powers of 12 mW and 20 mW when laser chip temperatures are 25˚C and 10˚C respectively. However, the laser frequency, 1049.65 cm^{-1}, is higher than our ozone-ammonia system required frequency range (1045 – 1047 cm^{-1}) and it is not possible to be used in our designed system.

3.2.2. Thermoelectrically Cooled HgCdT Infrared Detector

The detector for the QCLOPS is a three-stage TE-cooled IR photovoltaic detector (PVI-3TE-10.6) made by Vigo System S.A., Poland. It is optically immersed to a high refractive index GaAs hyper-hemispherical lens (1.6 mm diameter) and BaF_2 window [7] and comes in TO-8 packages. The responsivity and response time are 1A/W at 9.6μm and ~1ns respectively. The D^* values of the PVI-3TE-10.6 can be seen in figure 3.7 with

corresponding wavelength. We built a housing module for the detector including heat-sink, cooling fan and input/output interfaces. Figure 3.8 shows the detector in the TO-8 package, wire connections in a heat-sink housing, and completed module.

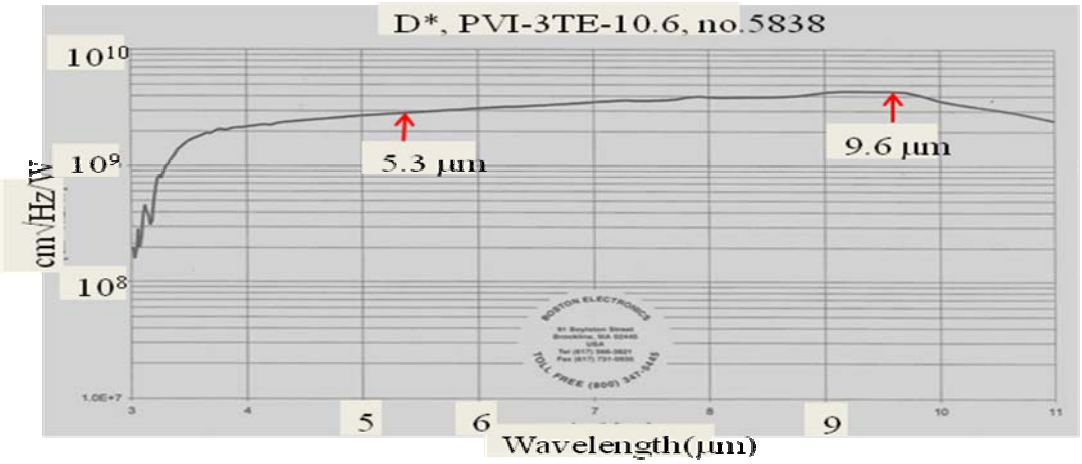

Figure 3.7: Detector performance, D^* value with corresponding wavelength (Provided by Boston Electronics)

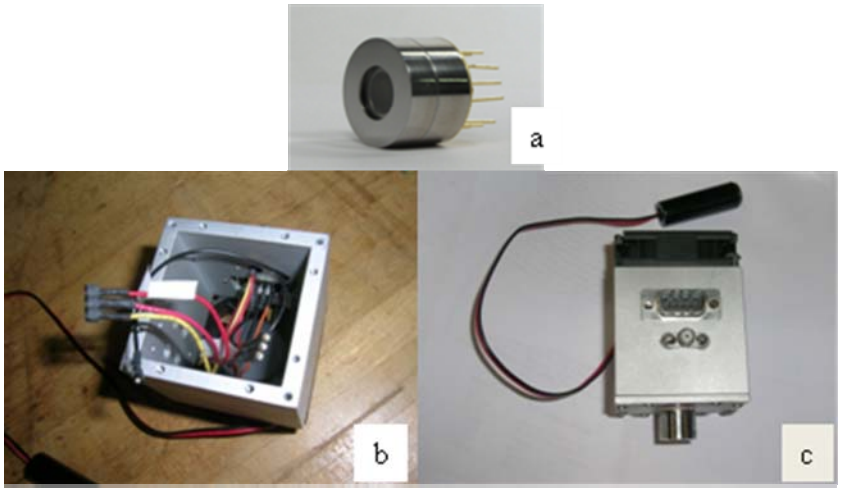

Figure 3.8: (a) PVI-3TE-10.6 detector in TO-8 package, (b) wire connection and (c) completed detector module with DB9, SMA interfaces and air cooling fan attached

3.2.3. Telescope and Chassis Design

The main concerns of the MIR QCL based telescope sensor chassis design are portability and field deployability. Therefore, the structure of the telescope system was constructed using considerably light materials such as anodized aluminum rails (XE25 series construction rails from Thorlabs) to build a chassis on an ultra light aluminum bread board base (part # PBG 11103 from Thorlabs). We designed a Newtonian telescope which is the simplest among different types of telescopes for our first system. An 8" diameter spherical mirror as primary and a 2.25" longitudinal diameter 45˚ angle mirror as a secondary mirror are installed in a 32" length, 10.5" wide and 10.5" height aluminum rail chassis which is attached on the 36" x 12" x 1" aluminum bread board base. The other system components: the QCL module, an infrared detector, alignment system and optics are located on a 24"x 10.5" carbon fiber board (part #: 8181K36 from McMaster Carr) that was fixed on the aluminum rail chassis as shown in figure 3.9. The telescope structure is enclosed with cast acrylic sheets and upper level components and optics are secured inside a 4.5" height top cover. This design allows the user to access upper level components for minor adjustment.

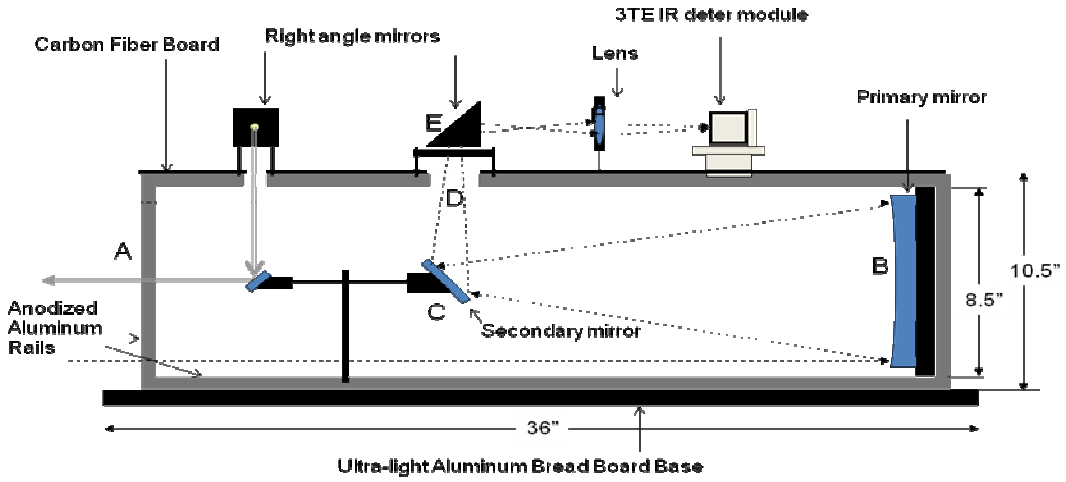

Figure 3.9: The schematic of the telescope and system components (not scaled)

We used an 8" diameter (f# 3.69) primary mirror due to mirror weight, cost and availability. A smaller secondary mirror needs to be further from the primary to collect all radiation reflected from the primary mirror and a large secondary mirror would block more radiation entering onto the primary. Our choice of a 2.25" diameter secondary mirror caused 7.9% obstruction and the 0.5" diameter post on which it was mounted contributed 2% and it made a total of 9.9% obstruction, which was 3 times less than the limited value, 30% obstruction [8]. It means that we are able to optimize the returned signal with very little loss. The location of the secondary mirror was obtained using the following equation.

$$d = \frac{a}{N} + b - \frac{a.b}{f} \tag{3.4}$$

where d is the diameter of secondary mirror, a is the distance from the optical axis of the secondary mirror to the focal surface, b is focal surface diameter, and f and N are the focal length and focal length to diameter ratio of the primary mirror respectively. Figure

3.10 shows the distance between optical axis of secondary mirror and focal surface, 'a' against the secondary mirror diameter, 'd' using equation 3.4. The solid blue line indicates the minimum diameter of the secondary mirror for various a values and the dotted green line defines the secondary mirror diameter if the focal surface diameter is 0.7 inch (45˚ angle 1" diameter mirror give 0.7" of focal surface diameter). In our system, the diameter of secondary mirror is 2.25" and we choose 7.25" for the distance of 'a'.

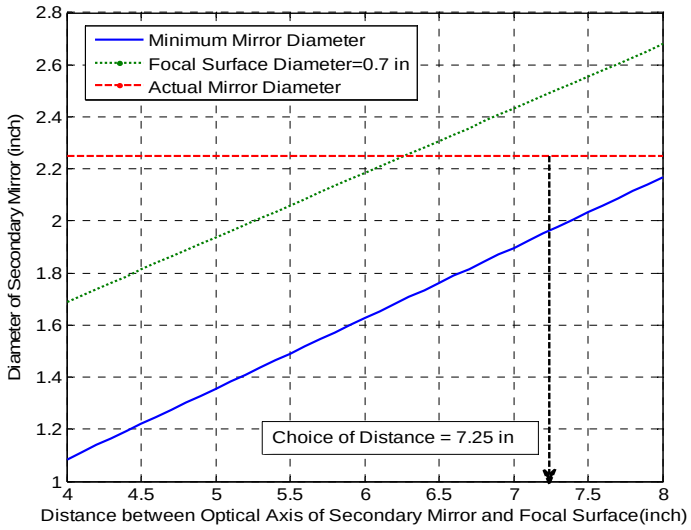

Figure 3.10: Design choice of secondary mirror location with mirror diameter

The following list and table 3.4 show the telescope component parameters and designed parameter values which optimize the telescope performance. The location of each component (A, B, C, D, E, and F) can be seen in figure 3.9. The Newtonian telescope was successfully collimated using the procedure described in reference [9].

- Primary mirror: 8" diameter, focal length = 750mm (29.527"), f# = 3.69
- Secondary mirror: 45˚ angle mirror, 2.25" diameter along optical axis

- The height of optical axis at the lower level = 5.25”
- The height of laser beam at the upper level = 2.00”
- Distance between primary and second mirrors = 21.22”

Components, location	Beam or required diameter	Available component diameter
Telescope aperture, A	N/A	8.5” x 8.5”
Primary mirror, B	8.00”	8.00”
Secondary mirror, C	2.24”	2.25”
Upper level hole, D	0.828”	1.500”
45˚ angle mirror, E	0.286”	0.707”
Focus lens, F	0.286”	1.000”

Table 3.4: List of required values and designed values of telescope parameters along with their locations

3.2.4. Optical setup

The challenging part of the QCL based open-path chemical detection instrument was its optical design. The major goals for the instrument's optics are:

1. To design and build an instrument to create a single "probe" beam from QCL and alignment laser beam
2. To propagate the probe beam to a retroreflector at a distance (m-km path-length) and
3. To collect a portion of the reflected probe beam for detection.

The optical setup of the system was installed on the upper level (top of the telescope) of the system chassis on the carbon fiber board. We made two 1” and 1.5”

diameters holes on the upper carbon fiber board to send transmitted laser beams from upper level to the 45˚ mirror which is attached with the lower level pole and the received signal from telescope to the detector. These locations of holes were indicated as #9 and #10 in figure 3.11.

We were able to maximize the distance between the two irises by placing them 18” apart along the length of 24” carbon board. The longer distance between these irises provide the more accurate alignment of the lasers. First, a room temperature IR detector (#8 in figure 3.11) was used at the end of second iris to align the QCL beam along the apertures of two irises and adjusting two mirrors, #3 and #4, we can align the visible laser beam through these irises. Therefore, the QCL beam and visible laser beam were passing together after the second iris and we can locate QCL beam, which is invisible, by looking at the visible laser beam. The returned signal from the retroreflector that is on the other side of our measurement is collected through the primary mirror and is sent to the upper level with a 45˚ angle secondary mirror. Finally, it is directed onto the detector surface by a 45˚ angle mirror (#10) through focusing lens (#11). The detector was placed on a XYZ state to collect optimal signal power. Table 3.5 shows the components on the upper level and their location on the board.

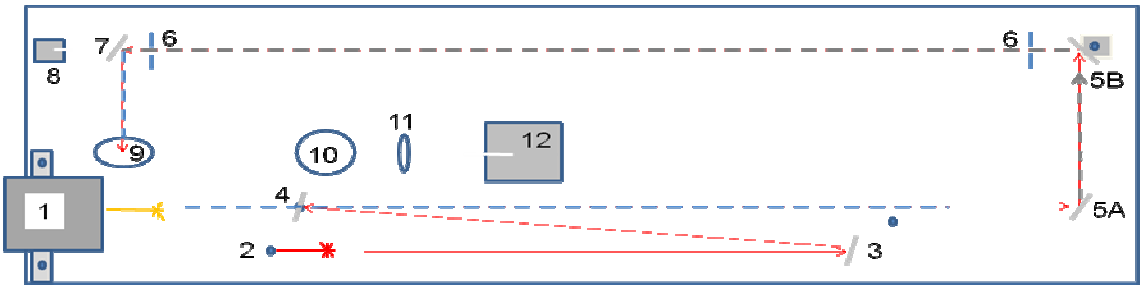

Figure 3.11: Schematic diagram of optical setup of the system on the second level board

#	***Component name, description***	***Position(x, y)***
1	QCL, mounted on a base block, beam height(z) 2”	(2.50, 3.25)
2	Alignment laser, fixed z 2”,	(7.00, 1.50)
3	Mirror, position adjustable (clamped), w/ 2 adjuster mirror mount	(5.00, 1.50)
4	Cold mirror (beam splitter) fixed z 2”, w/ 2 adjuster mirror mount	(8.50, 3.25)
5A, 5B	Mirrors w/ 2 adjuster mirror mounts, 5A on a clamped pole, 5B – on a flip mount	(23.0, 3.25), (23.0, 8.50)
6	Iris, fixed position and height, z= 2”	(22.0, 8.50), (4.00, 8.50)
7	Mirror, clamped pole, w/ 2 adjuster mirror mount, on a flip mount	(2.75, 8.50)
8	RT-detector, on removable magnetic base	(0.50, 8.50)
9	1” dia. Hole, right angle mount on 30 mm cage system rods, z=2”	(2.75, 5.25)
10	1.5 dia. Hole, right angle mount w/ an adapter on 60 mm cage sys.	(8.67, 5.25)
11	Lens, 1” dia., f=2”, on fixed pole, z=2”	(10.67, 5.25)
12	3TE detector module, mount on a XYZ translator	(12.67, 5.25)

Table 3.5: Locations and position description list of QCL, detector and optics components on the system upper level board

3.3. Resolution Limit

The spectral resolution of the intra-pulse QCL system, which was used in our system, is limited by the chirp rate of laser and temporal resolution of the detection system. The bandwidth-duration product,($\Delta\nu\Delta\tau$) of the system can't be less than a certain minimum value C, which is stated as 0.866 for rectangular time window and 0.441 for Gaussian time window [10]. Minimum achievable resolution and detector bandwidth are plotted with chirp rate of the laser are shown in figure 3.12.

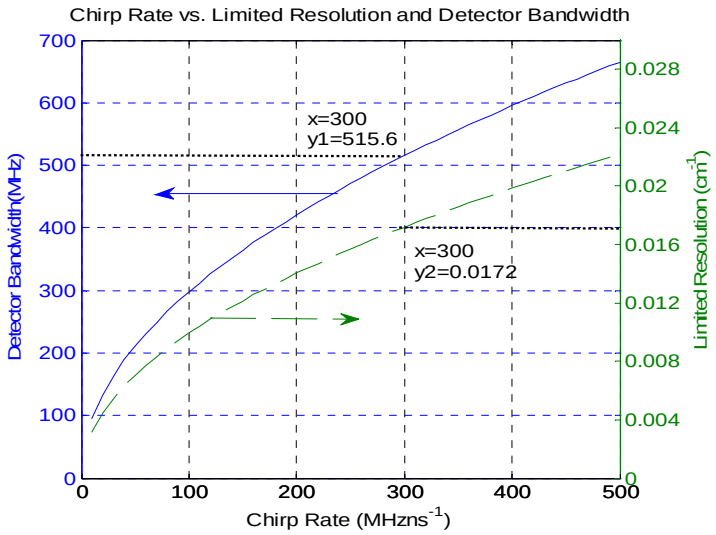

Figure 3.12: Resolution limit and detector bandwidth with chirp rate of QCL tuning mechanism

The chirp rate can be obtained from measurements of intensity modulated light transmitted through an etalon. Values for the parameters describing the chirp are obtained by fitting the measurement data to a theoretical model. The experimental measurement to define our system resolution was explained detail in chapter 4.

3.4. Link Power Analysis (Open-path System Model)

Link budget analysis evaluates the laser performance in the atmosphere and the capability of the receiver in registering a backscatter signal. Link budget analysis gives a result that is used to calculate optical efficiency and SNR of an open-path system. When combined with the theoretical SNR needed to retrieve gases at a given concentration, the link budget which provides a per pulse SNR can be used to obtain the integration time needed for given performance which ultimately determines the feasibility of the system. We performed link budget analysis for two field deployable QCL schemes; classical mono-static retro-reflector system and backscattering system.

The link budget analysis calculates total loss or the system efficiency from the individually calculated power attenuation by particles scattering, atmospheric turbulence, molecular absorption, free space laser beam propagation and system optics. These mechanisms can be cascaded as illustrated in equation 3.5 and 3.6.

$$\alpha_{tot} = \alpha_{scatt}\alpha_{turb}\alpha_{abs}\alpha_{FSL}\alpha_{opt.} \tag{3.5}$$

$$\eta_{RR} = \alpha_{tot} \; or \; \eta_{BS} = \alpha_{tot}\beta\Omega \tag{3.6}$$

$$P_R = P_0\eta \tag{3.7}$$

where α_{tot} is total attenuation, α_{scatt} is loss by particle scattering, α_{turb} is loss by atmospheric turbulence, α_{abs} is loss by absorption, α_{FSL} is free space loss and $\alpha_{opt.}$ is loss due to system optics, such as mirrors and lenses. η_{RR} which is defined by the total loss, is the optical efficiency for retroreflector system and η_{BS} is optical efficiency for backscattering system. η_{BS} is calculated by multiplying total loss with albedo β of

diffused surface, which we use as a target and the solid angle, Ω. Then, the optical system efficiency is multiplied with the laser output power, P_0 to obtain the received power, P_R on the detector.

3.4.1. Power Loss due to Scattering

When the laser beam propagates through atmosphere, some of its power re-radiate to random directions because of scattering by atmosphere particles, such as aerosols and attenuation due to scattering depends on laser wavelength (λ), atmosphere particle's size distribution (q), and visibility (V_m).

$$\alpha_{scatt} = \frac{3.91}{V_m}\left[\frac{\lambda}{550}\right]^{-q} \tag{3.8}$$

where λ is the laser wavelength in nm, V_m is visibility in km and q is the atmosphere particle's size distribution, which parametrically depends on V_m following [11, 12, 13] where visibility is measured at 550 nm. The q parameter is then simply interpreted as an angstrom coefficient providing a phenemological description of the wavelength dependence for realistic particles.

$$q = \begin{cases} 1.6 & (V_m > 50 \text{ km}) \\ 1.3 & (6 \text{ km} < V_m < 50 \text{ km}) \\ 0.585 V_m^{1/3} & (V_m < 6\text{km}) \end{cases}$$

The equation 3.8 shows that power loss due to particle scattering is smaller for longer wavelengths making this mechanism less of a problem for the long wave system.

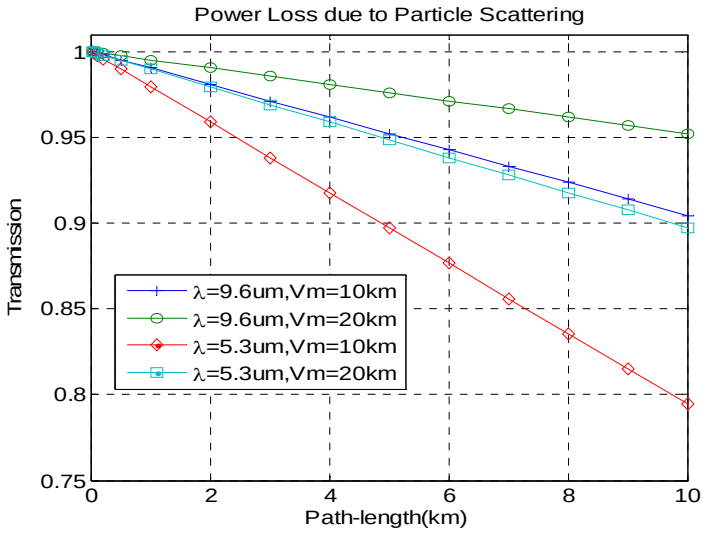

Figure 3.13: Power loss due to scattering

As shown in figure 3.13, transmittance is ~.98 for 9.6 μm system with 20 km visibility, but in 10 km visibility condition, transmittance decreases to ~.96 at 4 km path distance.

3.4.2. Power loss due to Atmospheric Turbulence

Turbulence is the effect of an irregular atmospheric motion and the temperature difference in atmosphere causes wind and convection process which generates erratic air movement. This distorts to laser beam profile after light propagate through the atmosphere. First, we calculated Rytov variance, σ_R^2 with the atmospheric structure function, C_n^2 (C_n^2 varies between 10^{-13} and 10^{-17} and we chose 10^{-14} for mild condition), which depends on the temperature, wind strength, altitude, humidity, and atmospheric pressure [13].

$$\sigma_R^2 = AC_n^2 k^{7/6} L^{11/16} \tag{3.9}$$

where *A* is 0.5 for the spherical wave and 1.23 for the plane wave, which is the case of our system's collimated laser beam, k = 2π/λ, and L is the path-length. Using aperture averaging phenomenon, we calculate the power scintillation index σ_p^2.

$$\sigma_p^2 = \sigma_I^2[1+1.062(\frac{kD^2}{4L})]^{-7/6} \tag{3.10}$$

where σ_I^2 is scintillation index and $\sigma_I^2 = \sigma_R^2$ for plane wave, D is receiver diameter. Then, we calculate power loss using equation 3.11 [11].

$$\frac{P_{in}}{P_{out}} = \exp[erfcinv(2\times10^{-4})\sqrt{2\ln(\sigma_p^2+1)}]\sqrt{\sigma_p^2+1} \tag{3.11}$$

We note from eq. 3.9 and 3.10 that the power loss is significantly reduced as the wavelength increases.

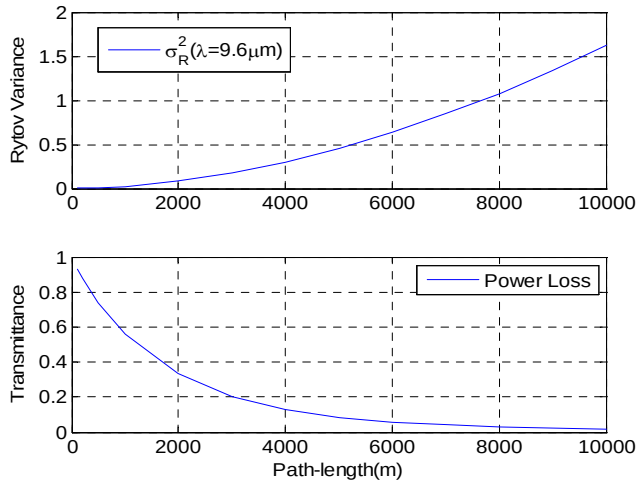

Figure 3.14: Rytov Variance of the 9.6μm laser transmission using the atmospheric structure function $C_n^2 = 10^{-14}$ (top) and power loss due to turbulence (below)

3.4.3. Power Loss due to Molecular Absorption

In our link model, the power loss due to background absorption has to be included. Power loss due to absorption depends on, the wavelength of the laser, the concentration of the gases involved and the open-path's distance. The OPSM can be used

for any frequency window and target gase of an open-path system, but in this study, we used ambient concentrations of H_2O (10^4 ppm), CO_2 (370 ppm), O_3 (20 ppb) and NH_3 (3 ppb) and transmittance values were obtained at the wing or background (transmittance at 1045.5 cm^{-1} in figure 3.15) of the absorption feature. For, example, the total absorption coefficient of these species in ambient concentration at the wing is given as $7.04x10^{-6}$.

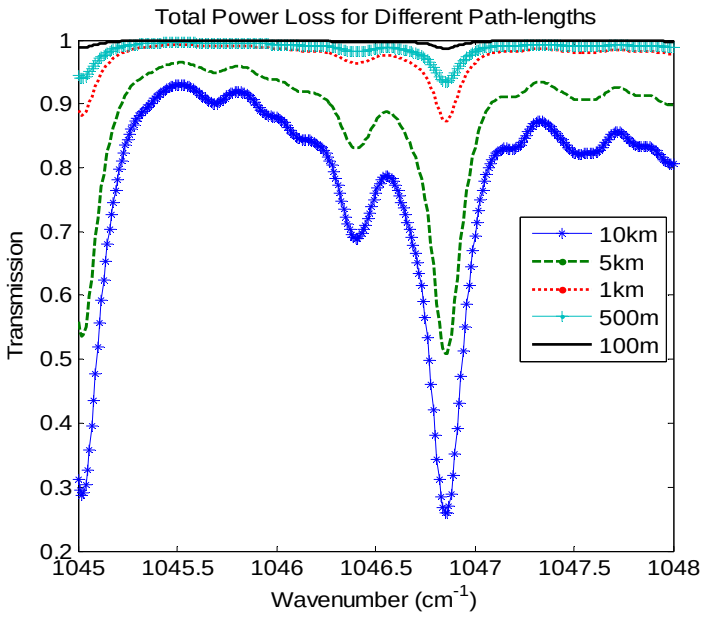

Figure 3.15: Power loss due to ambient gases (H_2O+CO_2+O_3+NH_3) absorption (generated using GENSPECT and HITRAN database [1, 2])

3.4.4. Free Space Loss due to the Laser Beam Divergence

The calculation of power loss due to beam divergence has two parts; 1) power loss between laser module and retroreflector when the laser beam diameter at the retroreflector is larger than retroreflector diameter, 2) power loss between retroreflector and telescope when the laser beam diameter at the telescope is larger than telescope diameter and additional loss by the secondary mirror blockage.

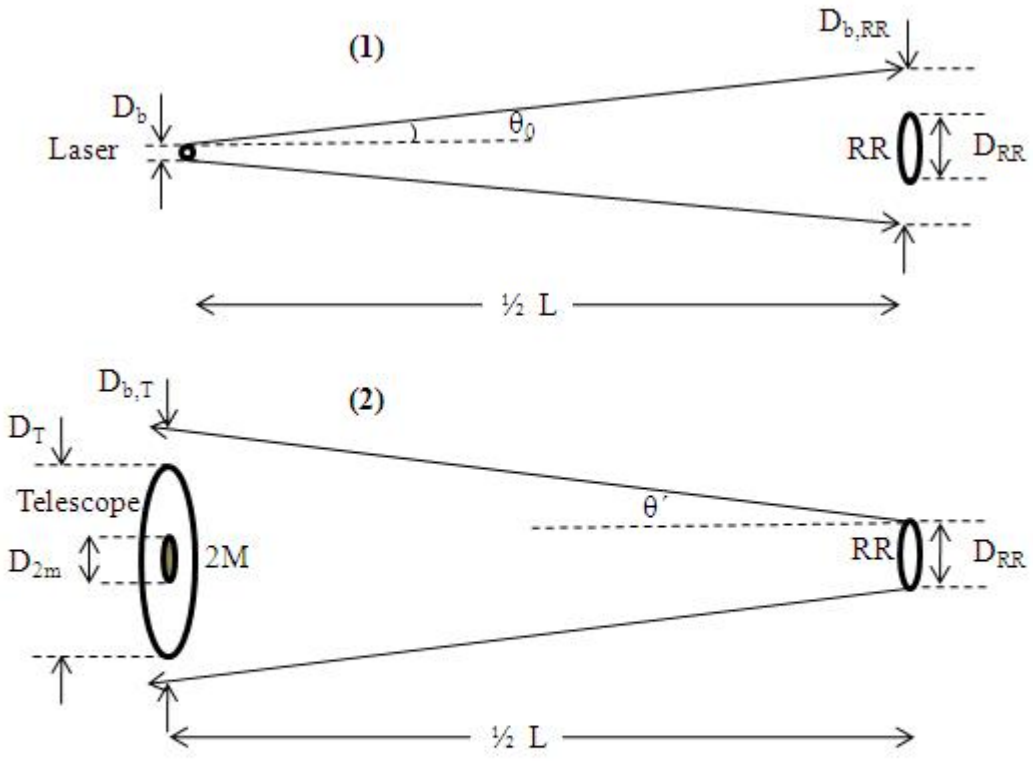

D_b = dia. of laser beam, RR = retroreflector, D_{RR} = dia. of RR
$D_{b,RR}$ = beam dia. at RR, θ_0 = half divergence angle, L = path-length
θ' = half divergence angle from RR to telescope, D_T = dia. of telescope
2M = secondary mirror, D_{2m} = dia. of 2M, $D_{b,T}$ = beam dia. at telescope
Note: not scaled

Figure 3.16: Geometry of the mono-static retroreflector open-path system to calculate divergences for 1) from laser module to the retroreflector and 2) from the retroreflector to the telescope

First, we calculated the laser beam size at the locations of retroreflector (20m, 30m, 50m, and 60m), which is half of the total path-length, using beam spot size at the laser module (4mm) and beam divergence (4mrad) which is critical parameter for free space loss. While measurements using a liquid crystal sheet at different distance may give an experimental estimate, we used estimates based on a theoretical minimum divergence

ofa Gaussian beam as a first estimate. In particular, for a Gaussian beam, the effective diameter (~86% of total power contained) along the distance z is defined as [14]

$$W(z) = W_0 \sqrt{1 + (\frac{z}{z_0})^2} \tag{3.12}$$

where W_0 is the beam width at z=0, and z_0 is where beam width becomes $\sqrt{2}$ W_0 and $z_0 = \pi W_0^2 / \lambda$ (Rayleigh range) . For $z >> z_0$, the equation 3.12 can be rewrite as

$$W(z) \approx \frac{W_0}{z_0} z = \theta_0 z \tag{3.13}$$

where θ_0 is half-angle of Gaussian function cone and the divergence of the beam Θ is defined as

$$\Theta = 2\theta_0 = \frac{4}{\pi} \frac{\lambda}{D} \tag{3.14}$$

where D is diameter of laser beam and λ is wavelength. If we calculate the Gaussian beam divergence angle which contains 99% of the total power, the equation 3.14 becomes

$$\Theta = \frac{6}{\pi} \frac{\lambda}{D} \tag{3.15}$$

Once the divergence is estimated, the far field diameter of the beam is easy to calculate for any path range and the power loss due to the size of retroreflector is calculated as the ratio of retroreflector area to the laser beam area at the retroreflector as the function of distances.

For the loss mechanism from the retroreflector to the telescope, we need to redo the above calculation but using the modified divergence Θ' due to cutting off of the angular modes by the retroreflector. Therefore, the divergence of the laser beam from the

retroreflector to telescope is modified by the ratio of retroreflector diameter D_{RR} and beam diameter at the retroreflector $D_{b,RR}$ (i.e. $\Theta' = \Theta \times (D_{RR}/D_{b,RR})$). There are two situations in the calculation of the power loss in this part. When diameter of beam at the telescope $D_{b,T}$ is smaller than the telescope diameter D_T, there is no power loss due to the telescope size but the loss due to the secondary mirror (dia. D_{2M} = 2.25 in) blockage is included. This loss is calculated from the ratio of beam area $A_{b,T}$ and unblocked area (A_b-A_{2M}) by the secondary mirror (i.e. loss=$(1-(A_{2M}/A_{b,T}))$. The other situation, when $D_{b,T} > D_T$, the power loss due to the telescope size (i.e. telescope area A_T / $A_{b,T}$) and the power loss due to the secondary mirror (i.e. $1-(A_{2M}/A_T)$. are included in the calculation of power loss from the retroreflector to the telescope.

3.4.5. Power Loss due to System's Optics

Efficiency factors are simple to obtain based on the mirror coatings. Our system's optics is comprised of gold and aluminum coated components but after cascading, attenuation due to transmitter and receiver of the system is estimated to 0.80 and 0.78 respectively.

3.4.6. Quantifying System Noise

The three main sources of the system noise were included [15, 16].

1. Noise from IR-detector
2. Noise from pre-amplifier
3. Noise from data acquisition system

The system noise level was defined by vector sum of the root mean square (RMS) voltages of each component as:

$$V_{N,total} = \sqrt{[G \times (V_{N,\det} + V_{N,amp})]^2 + V_{N,DAQ}^2} \tag{3.15}$$

where G is the gain of the amplifier, $V_{N,det}$ is detector noise voltage, $V_{N,amp}$ is preamplifier noise voltage and $V_{N,DAQ}$ describes noise voltage from the data acquisition system. They can be calculated using equation 3.16, 3.17 and 3.18.

$$V_{N,det} = N_{0,det} \times \sqrt{\Delta f} \times R_{det} \tag{3.16}$$

$$V_{N,amp} = N_{0,amp} \times \sqrt{\Delta f} \tag{3.17}$$

$$V_{N,DAQ} = \left(\frac{V_{sig}}{2^{bit} \times \sqrt{12}}\right) + \left(\frac{V_{sig}}{10^{SINAD/20}}\right) \tag{3.18}$$

where $N_{0,de}$ and R_{det} are detector noise spectral density and resistance respectively, Δf is detector and amplifier bandwidth, $N_{0,amp}$ is pre-amp noise spectral density. The data acquisition system in this study is 8-bit with signal-to-noise-and-distortion ratio (SINAD) 48 dB. V_{sig} is received signal voltage as DAQ noise depends on the input signal level [17, 18]. We used preamplifier when the returned signal < 0.1 V and we included gain factor (Gain = 20) to the $V_{N,det}$ and $V_{N,amp}$ as preamplifier was used.

This model does not account for the possibility of scintillation noise due to turbulence conditions. While the common understanding is that because of the small pulse times such fluctuations are not expected to be of concern, such mechanisms may be relevant for long pulse time averaging where the experiment time can be on the order of seconds. Therefore an analysis based on the weak fluctuation theory was made to

investigate the need to include this mechanism, and the results are given in **appendix A.** The main point is the RMS noise from turbulence (including receiver averaging) is negligible in comparison to the main mechanism of equation 3.15-3.18.

3.4.7 The Open-path System Model Simulation Results for O_3-NH_3 System

It is clear that for the experimental divergences from the QCL ~4mrad will cause long path detection to be impossible since so much of the signal will be lost due to free space loss mechanisms. Therefore, efforts must be made to improve this and we plan to implement a 10x beam expander, which expands beam diameter and clearly, if the beam diameter is to be increased, the far field divergence will be decreased by expander power MP [19].

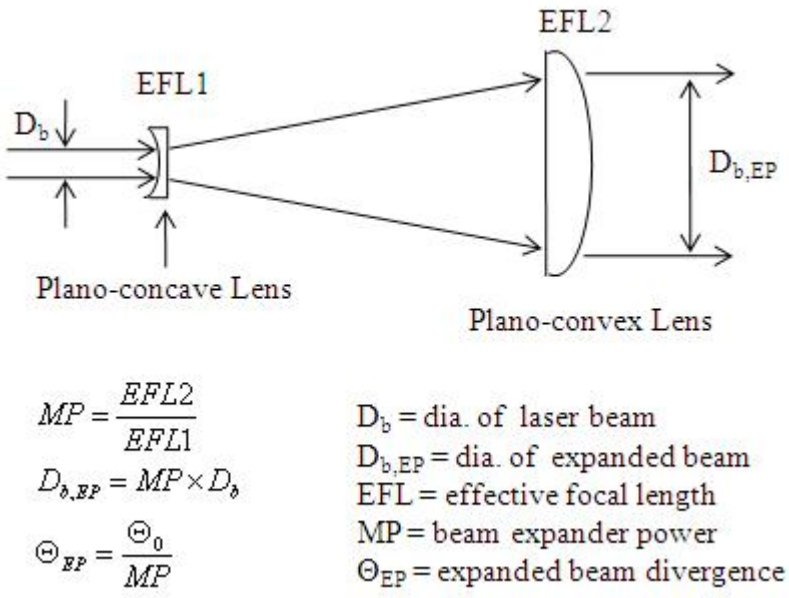

Figure 3.17: Diagram of the Galilean beam expander

As shown in figure 3.17, a Galilean beam expander has a negative lens and a positive lens. The beam diameter is first increased in size by the beam expander power

MP then the beam divergence is reduced by the MP. Based on the numbers after the 10x beam expansion, the SNR and the measurement time to achieve target accuracy can be calculated.

Figure 3.18 shows the optical efficiency or total power loss of the retroreflector system and the backscattering system.

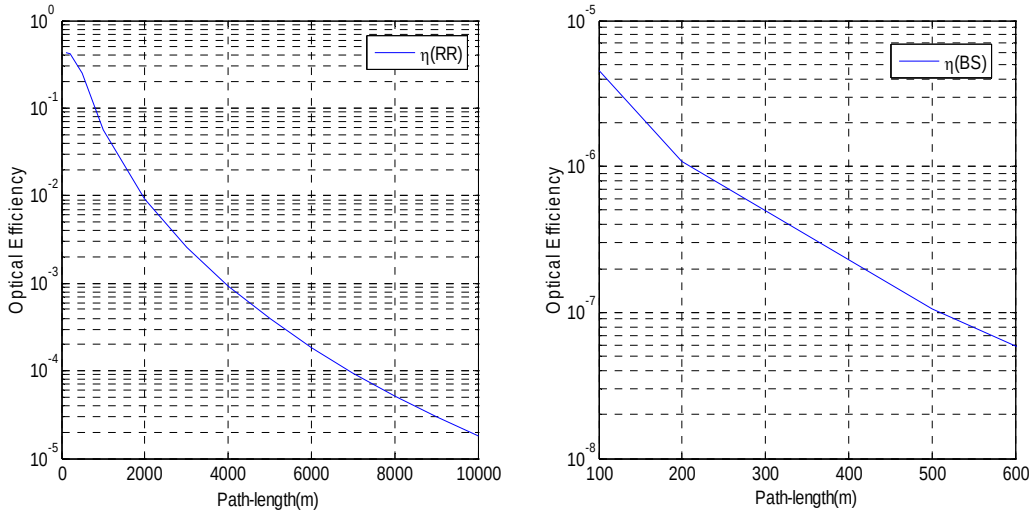

Figure 3.18: Optical efficiency of reflector system (left) and backscattering system (right) using 10x beam expander (D_b=4cm, Θ_{div}=0.4mrad, D_{RR}=12.7cm, D_T=20.3cm)

Since the total power loss for the backscattering system is $4.5\text{x}10^{-6}$ at L =100m, it is not possible to design O_3-NH_3 backscattering system because the received signal is below the system noise level when $\eta_{BS}<10^{-5}$ as shown in figure 3.19 (P_{QCL}=200mW). The SNR of the retroreflector and backscattering systems were defined by received signal power divided by sum of the component of noise power as in equation 3.19.

$$SNR_{RR(BS)} = \frac{P_0 K_{det} R_{det} \eta_{RR(BS)}}{V_{N,total}} \qquad (3.19)$$

where P_0 - laser transmitted power, η – optical efficiency of retroreflector system or backscattering system, K_{det} – the detector current responsivity, R_{det} – detector resistance, and $V_{N,total}$ is total RMS noise as equation 3.15. The SNR of QCLOPS using retroreflector is shown in figure 3.19.

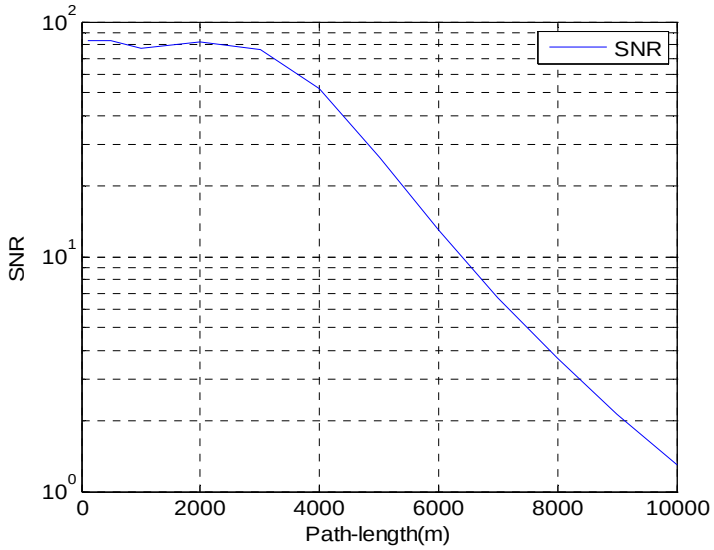

Figure 3.19: SNR with path-length for the retroreflector system (DAQ noise, which depends on the signal, is dominant so that the SNRs do not change much from L=100m to 3km. Then, the preamplifier noise, which is a constant for the specific gain, makes the SNRs decrease from 50 for L=4km to 1.5 for L=10km (D_{RR}=12.7cm, D_T=20.3cm)

Real time measurement is one of main concern in system design. To get a high accuracy measurement, we need a sufficiently high SNR value which may not be achievable with a single shot. The SNR increases with the square root of averaged samples as the following equation.

$$SNR_n = SNR_1 \times \sqrt{n} \tag{3.20}$$

where SNR_n is SNR after averaging n samples, and SNR_1 is a per pulse SNR. That means we have to take many samples and average them and the measurement time needed is clearly the issue. Investigation on limitation or requirements of SNR improvement by averaging samples is explained detail in the **Appendix B**. The required SNR and pulse repetition rate are used to calculate the system temporal resolution.

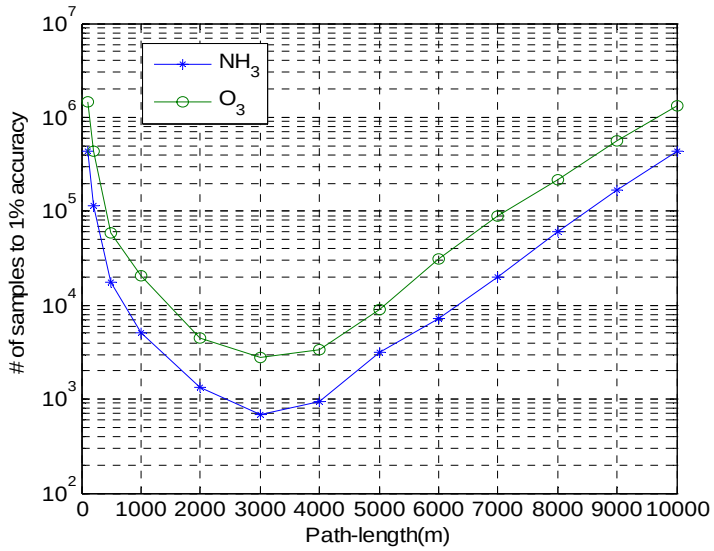

Figure 3.20: Number of samples required to achieve 1% accuracy result with 10x beam expander, and D_{RR}=12.7cm

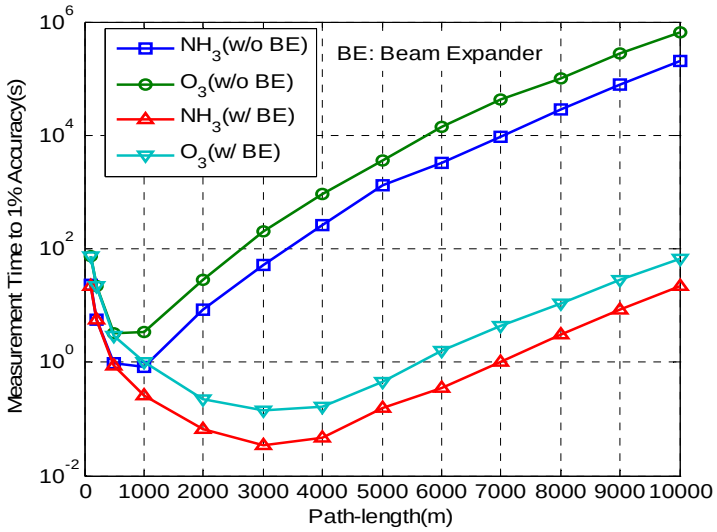

Figure 3.21: The measurement time to achieve 1% accuracy result (P_{QCL} = 200 mW, pulse rate = 20 kHz)

The results show that the system using a 10x beam expander can simultaneously detect O_3 and NH_3 with 1% accuracy in < 1min when L = 100 m, but if we increase L = 1 km, we will be able to get the results in < 1 s. If we don't use the beam expander, the measurement time increases from L=500m and it takes >3min for L=3km and ~17min for L=4km. Moreover, the result also shows that the optimal path-length of this system with the 10x beam expander is 3 km where there is some trade-offs we can do for other system parameters, such as laser output power, detector D*, and optics.

References

[1] B. M. Quine, J. R. Drummond, "Genspect: a line by line code with selectrable interpolation error tolerance", JQSRT **74** 147-165 (2003)

[2] L.S. Rothman, A. Barbe, D.C. Benner, L.R. Brown, C. Camy-Peyret and M. Carleer et al., "The HITRAN molecular spectroscopic database: edition of 2000 including updates through 2001, JQSRT **82** 5–44 (2003)

[3] V. Vladutescu, B. Gross, F. Moshary, S. Ahmed, "Assessment of a QCL Laser Approach for the Simultaneous Measurement of Ambient Ammonia and Ozone" SPIE Proceedings, 6760-6768 (2007)

[4] F. Tittel,D. Richter, and A. Fried, "Mid-infrared laser applications in spectroscopy" Springer Berlin, **89**, 458-529 (2003)

[5] http://www.maxion.com/singlemode.html

[6] "User Manual for LS-03-D Laser System", Cascade Scientific, Document Number D-7010-0003 (2007)

[7] www.vigo.com.pl, from VIGO System, S.A., Warsaw, Poland

[8] V. Rutten, ¨Telescope Optics; A Comprehensive Manual For Amateurs¨, WIllmann-Bell, Inc., Virginia (2003)

[9] http://www.galacticfool.com/collimate-newtonian-telescope

[10] G. Duxbury, N. Langford, M. McCulloch, and S. Wright, "Quantum Cascade Semiconductor Infrared and Far-infrared Lasers: from Trace Gas Sensing to Non-linear Optics", Chem. Soc. Rev., **34**, 921-934 (2005)

[11] Z. Bielecki, W. Kolosowski, J. Mikolajczyk, “Free-space Optical Data Link Using Quantum Cascade Laser”, PIERS Proceedings, Cambridge, USA, July 2-6 (2008)

[12] A. Biswas and M. Wright, “Mountain-Top-to-Mountain-Top Optical Link Demonstration: Part I”, IPN Progress Report, 42-149 (2002)

[13] A. Prokes, “Atmospheric effects on availability of free space optics systems”, Optical Engineering 48(6), 066001 (2009)

[14] B. Saleh, and M. Teich, “Fundamentals of Photonics”, 2nd ed., Wiley-Interscience (2007)

[15] P. Corrigan, M. Lwin, B. Gross, F. Moshary, “Design of an ozone and ammonia open-path sensor with a quantum cascade laser”, prepared to submit to a technical journal

[16] P. Corrigan, “Quantifying QCL System Noise”, presentation slides

[17] W. Kester, “Understand SINAD, ENOB, SNR, THD, THD + N”, Mt-001 Tutorial, Analog Devices (2009)

[18] L. Kristensen, P. Kirkegaard, “Digitization Noise in Power Spectral Analysis”, Journal of Atmospheric and Oceanic Technology, **4**, 328-335 (1987)

[19] http://64.106.166.130/techSupport/resource_center/downloads/wp-understanding-lasers-and-laser-optics.pdf

CHAPTER 4: VALIDATION MEASUREMENTS

Since the original implementation of ozone-ammonia detection system is not possible at present, we decided to test our model on a similar system where the source is available and validations are possible. In this chapter the QCLOPS system with 5.3μm wavelength QCL (model #: DQ5-M575R from Maxion Technologies, Inc.) will be utilized. The laser output power is calculated from the measurement while other components, such as the laser driver, detector, pre-amplifier, collecting telescope, and optics, are the same as that originally designed for the 9.6μm O_3 and NH_3 simultaneous detection system, which was characterized in chapter 3. The theoretical absorption features of the relevant trace gases (H_2O, CO_2, NH_3 and O_3) will be analyzed in the laser spectral range, 1895-1902 $cm^{-1}$with the aim of demonstrating suitable water vapor retrieval with minimal problems due to interfering gases.

4.1 Introduction

We installed the 5.3 μm QCL in the QCLOPS because our originally intended 9.6μm QCL is not currently available and efforts at modeling this system will provide the means to perfect the modeling of the 9.6 μm system. In addition, the 5.3μm system can measure the concentration of water vapor, which is an important greenhouse gas and the most abundant trace gas in the atmosphere [1]. Measurements can be validated based on local measurements of RH and complementary Fourier Transform Infrared (FTIR) system. Therefore, this effort serves two purposes: 1) demonstrating ambient retrieval of

trace gas using chirped pulse QCL techniques and 2) assessing the link power model so that we have confidence to predict the per-pulse SNR for a given system.

In particular, the system modeling (link power analysis) provides estimates of the receiving power, noise level and SNR of an open-path system with corresponding path-lengths using inputs from system components, and atmospheric conditions, such as visibility and atmospheric structure function [2] and it is the model that should be validated. To assist in these efforts, our recently built 5.3µm QCLOPS was deployed in the field for system characterization measurements including frequency tuning rate, output power measurements, noise level measurement and open air water vapor concentration measurements in various path-lengths, laser chip temperatures, and continuous measurements for hours. The results of these measurements will be presented in chapter 5.

Detector Responsitivity

The normalized detector detectivity D* value is defined as [3]:

$$D^* = \frac{R_i \sqrt{\Delta f}}{I_n P \sqrt{A}} \tag{4.1}$$

where R_i is responsivity, I_n is noise current, Δf is the noise bandwidth, and A is the active area of the detector. Since we used the same detector for 5.3µm system, all variables are the same except D* and R_i. The detect responsivity for 5.3µm was calculated from equation 4.2.

$$R_{i,(5.3)} = \frac{D^*_{(5.3)}}{D^*_{(9.6)}} \times R_{i(9.6)} \tag{4.2}$$

The detector responsitivity at 5.3µm is 0.644 A/W.

Laser Output Power

The output power of 5.3µm QCL was measured in the lab with the laser temperature -5˚C, pulse width 1µs, pulse repeating rate 20 kHz, laser driver (Cascade System) supply voltage 12V. The detected output signal of the laser using 3-TEC PVI-10.6 (Vigo System) detector and the 8-bit oscilloscope (Tektronix DPO-4054) is shown in figure 4.1.

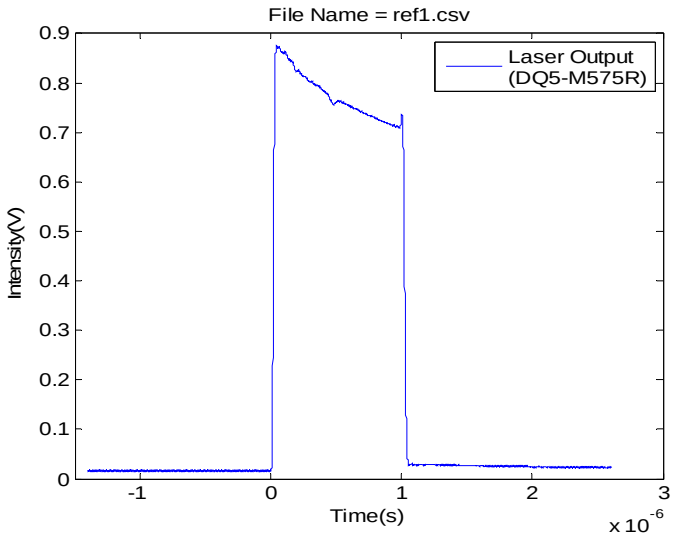

Figure 4.1: Measured pulse signal of 5.3µm QCL (DQ5_M575R)

The output power was calculated from measured signal voltage and the detector's parameter values.

$$P_{(5.3)} = \frac{V_{sig}}{G_{amp} R_{det} R_{i\,(5.3)}} \tag{4.3}$$

where $P_{(5.3)}$ is the output power of 5.3µm QCL, V_{sig} is measured laser pulse voltage, G_{amp} is pre-amplifier's gain, R_{det} is detector resistance, and $R_{i(5.3)}$ is responsivity of detector at 5.3µm. The average output power of 2% duty cycle 5.3µm QCL pulse is 6.03mW (power on the detector with a immersion lens (D_{lens}=1.6mm) = 2.41mW and D_{beam}=4mm).

Absorption Features at 5.3µm Region

We generated absorption spectra of H_2O, CO_2, NH_3, and O_3 in their ambient concentrations, atmosphere pressure and temperature, for 1m path-length using GENSPECT program at the 5.3µm QCL range (1895-1902 cm^{-1}).

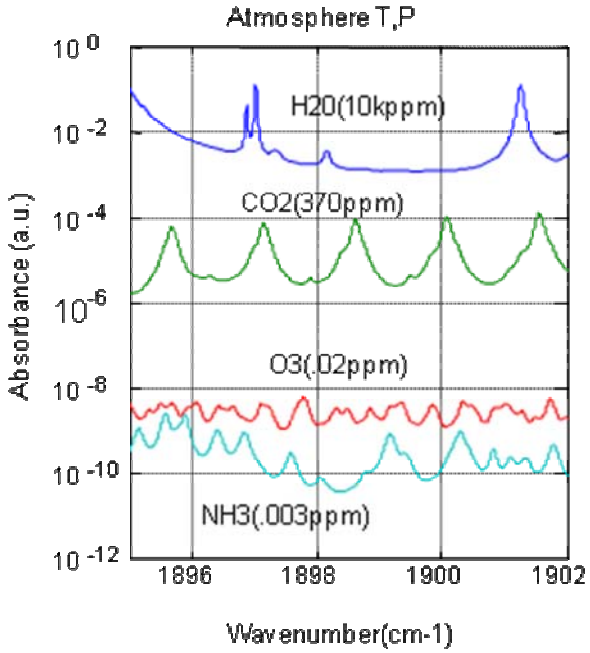

Figure 4.2: Absorbance spectra of H_2O, CO_2, O_3 and NH_3 in ambient concentration and atmosphere temperature and pressure for 1m path-length (generated using GENSPECT and HITRAN 2000 database)

As shown in figure 4.2, the absorbance of H_2O is 3 and 8 orders of magnitude higher than CO_2 and NH_3 respectively. Therefore, using this QCL we are not able to see absorption features of CO_2, O_3 and NH_3 because of the strong H_2O absorption, but making it useful for clean water vapor measurements.

The alignment procedures for the system and for the field measurements

The system alignment procedures were performed before the field measurements and during the field measurements when we changed different path-lengths.

Pre-field measurement alignment

The purpose of this work was to make sure that the QCL beam and the red "trace" diode laser beam were collinear over the distance of interest. First, the QCL beam was aligned through two irises, which were fixed on the system ~20 inches apart as shown in figure 4.3, by using a room temperature detector which was positioned two inches after the second iris. The red laser beam was co-aligned after it was reflected by a cold mirror which transmitted the QCL beam. The co-alignment is guaranteed by passing both red and QCL beam through the apertures of two irises which would be opened to the maximum available diameter ~2cm during measurements to avoid the appearance of interference fringes. The QCL beam and co-aligned red laser beam were transmitted from the center of the telescope along optical axis of telescope by a 45˚ angle mirror which was attached at the back of secondary mirror (see figure 3.9: the schematic of the telescope and system components). The co-alignment of the QCL and red beams and the parallel propagation with the optical axis of the telescope were verified by moving the retroreflector to a distance of 16m path-length inside the room.

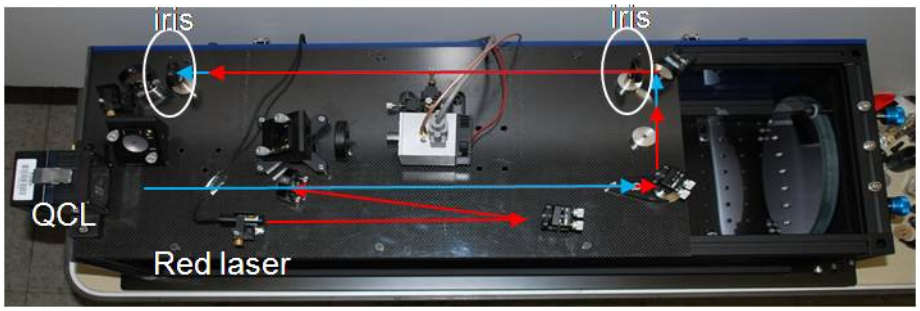

Figure 4.3: Top view of the system showing the QCL beam trace and red laser beam trace

Alignment Procedures during field measurements

Before we make any alignment for the field measurement, first, the system was adjusted to be leveled. The retroreflector was set at the designated location which is 20m, 30m, 50m or 60m away from the telescope and the red laser beam spot was incident on the center of the retrorflector. We moved the system horizontally to obtain maximum returned signal power on the detector. The alignment procedures were repeated when we made measurements for different path-lengths.

4.2. Laboratory Measurements

This chapter concerns the wavelength calibration of the QCL and development of the algorithm software for the QCLOPS-CCNY, an open-path ambient monitoring system. After characterizing of 5.3µm-QCL system, based on intra-pulse tuning mechanism, multi-pass gas cell configuration, the results of the laboratory experiments are analyzed and discussed in detail at the end of each section.

4.2.1. Laser Tuning Rate Measurements

Introduction

The tuning rate of the intra-pulse DFB QCL is depended on the laser temperature, and laser pulse width. The two reasons of doing this experiment are to calculate the spectral resolution of the laser which is needed in calculating the filter-function (instrument function) and to match the time domain measurement data to the frequency domain reference absorption spectrum.

Theoretical background

The finite spectral resolution of a pulsed laser can be defined from the uncertainty relation which states that the time-bandwidth product ($\Delta\nu.\Delta\tau$) cannot be less than a constant value, C [4]. The upper limit of the intra-pulsed QCL spectral resolution is calculated from equation 4.4 [5, 6].

$$\Delta\nu.\Delta\tau = C \tag{4.4}$$

where C=0.886 for a rectangular time window and C=0.441 for a Gaussian time window (in our cause C=0.886). From the chirp rate (frequency tuning rate) which we can

obtained from the measurement, we calculate the resolution of the QCL using equation 4.5.

$$\Delta\nu = \sqrt{C \times \frac{d\nu}{dt}} \tag{4.5}$$

where (dν/dt) is the tuning rate of the laser.

Experimental setup

Two measurements, a reference spectrum measurement and an etalon fringe pattern measurement, were taken to calculate tuning rate of the QCL. In these experiments, we used the 5.3 µm DFB QCL (DQ5_M575R from Maxion) with two different detectors; a room temperature detector (PVM-10.6, D*=1x10^{7} Jones @ 10.6µm) and a thermoelectrically cooled detector (PVI-3TE-10.6, D*=2.9x10^{9} Jones @10.6µm) both from Vigo Systems. The Germanium etalon was obtained from Boston Electronics and its free spectral range (FSR) is 0.048 cm^{-1}.

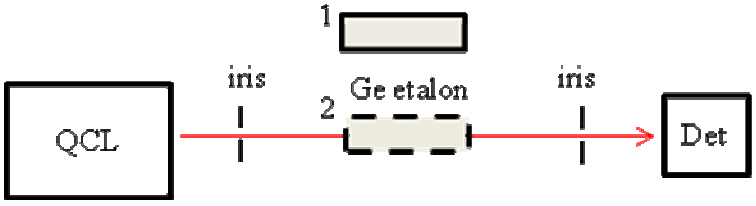

Figure 4.4: Experimental setup for QCL tuning rate measurements; 1) reference spectrum measurement when the etalon is out of laser beam path and 2) etalon fringes measurement when the etalon is installed on the laser beam path

The measurements were performed under the following operational conditions; QCL temperature 10˚C with 500 ns pulse width and laser temperature -5˚C with 1µs

pulse width because the T_{QCL}=10˚C covers 1897.5 cm^{-1} peak while T_{QCL}=-5˚C covers 1901.8 cm^{-1} peak of the H_2O absorption spectrum.

Result and Discussion

The experimental results showing reference signal, etalon fringes and normalized fringes are presented in figure 4.5. For visualization purpose, the normalized fringes are zoomed and placed in a box at the bottom part of the figure.

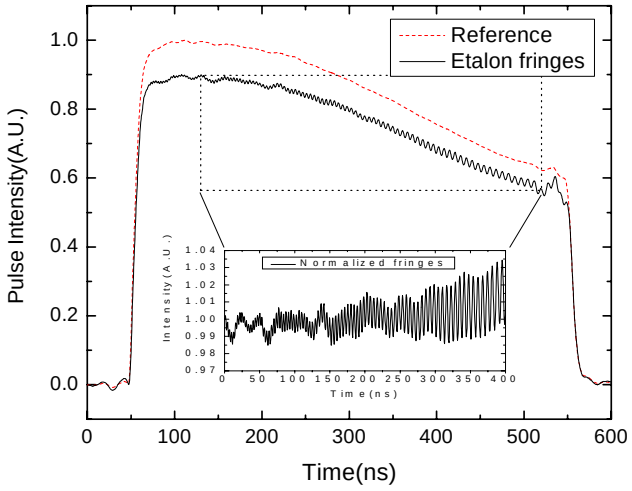

Figure 4.5: Reference signal, etalon fringe pattern and normalized fringes of the DQ5-M575R with T_{QCL}=25˚C and pulse width=500ns

The time and frequency range between two peaks of etalon fringes were calculated by the time interval of them and FSR of the etalon respectively. Then, the frequency tuning rates were calculated as:

$$\frac{dv_i}{dt} = \frac{FSR}{t_{i+1} - t_i} \tag{4.6}$$

where dv_i/dt and t_i are the tuning rate and time value at i^{th} time. As shown in figure 4.6 and 4.7 the frequency tuning rates decrease with the time, for example in figure 4.6 chirp

rate is 0.013 cm^{-1}/ ns at t=170 ns and the chirp rate is 0.007 cm^{-1}/ns at t=450 ns. Based on these measurements we calculated the resolution of the QCL using equation 4.6, and it is ~ 0.017 cm^{-1}. The frequency calibration point is based on matching the time of the peak absorption signal to the frequency of GENSPECT generated absorption peak (1897.5 cm^{-1} for T_{QCL}=10˚C, and pulse width = 500ns). From the calibration point, the time domain of measurement signal was converted to frequency domain using the above calculated frequency tuning rate at each point. The time-frequency calibration results of two different QCL operation condition are shown in figure 4.6 and 4.7.

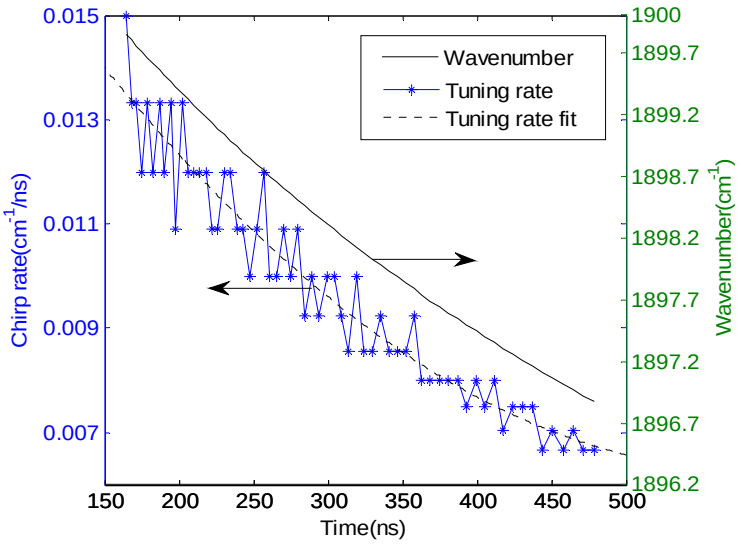

Figure 4.6: Laser tuning rate and tuning range at T_{QCL}=10˚C and pulse width = 500ns

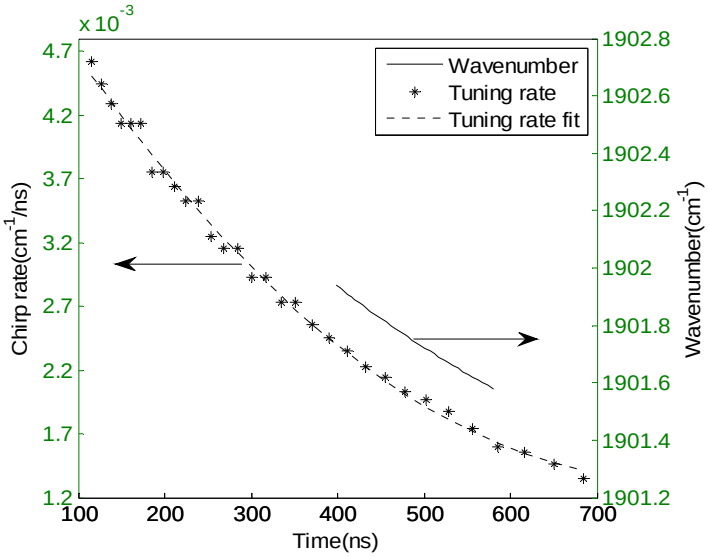

Figure 4.7: Laser tuning rate and tuning range at T_{QCL}=-5˚C and pulse width = 1μs. Its average tuning rate is 0.022 cm^{-1}/ns and the calculated spectral resolution is 0.008 cm^{-1}.

4.2.2. Multi-pass Gas Cell Measurements

Introduction

As explained in chapter 2, the concentrations of target gases were calculated by obtaining the transmission spectrum from the ratio of measurement spectrum and the reference spectrum, which was generated using GENSPECT and HITRAN database in the same conditions with measurement. Testing our retrieval method and calibrating wavelength of the QCLOPS are difficult due to pressure, temperature and instrumental (resolution, line shape, frequency shift) effects of the reference spectra. To address this problem, we first applied the retrieval algorithm to a simple experiment in a multi-pass gas cell configuration. Field measurements are discussed in chapter 4.3.

The Multi-pass Gas Cell

A Herriott cell (off-axis resonator) is typically formed with two spherical mirrors reflecting several times an incident laser beam before letting it out of the cell and it offers long path-lengths in a small volume [7]. The QCLOPS system was designed to detect low concentration levels of trace gases, such as ppt to ppb concentrations of O_3 and NH_3 by increasing signal to noise ratio with long path-length. The astigmatic mirror multi-pass absorption cell (AMAC-200 from Aerodyne Research Inc.) gives 210 m path-length from 238 laser beam paths inside the cell with in-out half-angle 2.5˚. The cell has a BaF_2 window which allows us to make efficient infrared spectroscopy measurements over the 3-11μm band [8].

Experimental Setup

The experimental setup is shown in figure 4.8. We present a laboratory analysis of H_2O concentration using the 5.3 μm DFB-QCL (DQ5-M575R from Maxion Technologies Inc.), an astigmatic multi-pass absorption cell (AMAC-200 from Aerodyne Research), a room temperature photovoltaic IR detector (PVM 10.6 from Vigo Systems) and an 8-bit resolution oscilloscope (DPO 4054 from Tektronix). We operated the QCL with T_{QCL} = 0˚C, pulse width = 500ns, pulse repeating rate = 40 kHz, and supply voltage = 13V. A strong H_2O absorption peak was observed between frequencies of 1899 cm^{-1} and 1902.5 cm^{-1}.

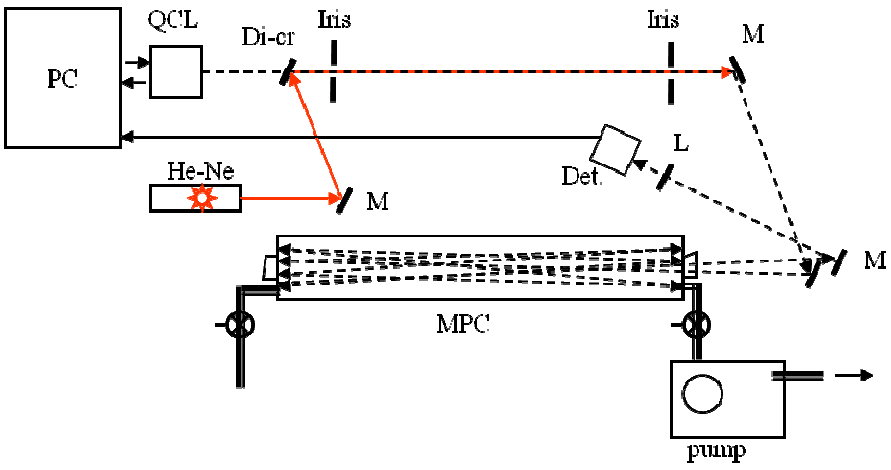

Figure 4.8: Experimental setup of 5.3 μm DFB QCL with a 210 m multi-pass gas cell (M: gold coded mirror, L: lens, Di-cr: dichroic filter or cool mirror, MPC: multi-pass gas cell, Det.: IR detector, He-Ne: alignment laser

Results and Discussions

We took a 213 m absorption path-length measurements with air filled cell (gas absorbed signal) and vacuum cell (reference signal) and calculated normalized absorbance signal from the ratio of these two measurements (figure 4.9) using equation 4.7 and 4.8.

$$T(t) = \frac{\frac{I_{abs}(t)}{\max(I_{abs}(t))}}{\frac{I_{ref}(t)}{\max(I_{ref}(t))}} \tag{4.7}$$

$$A_{meas.}(t) = -\log(T(t)) \tag{4.8}$$

where $I_{abs}(t)$ is gas absorbed signal, $I_{ref}(t)$ is reference signal, $T(t)$ is transmission signal and $A_{meas.}(t)$ is absorbance signal.

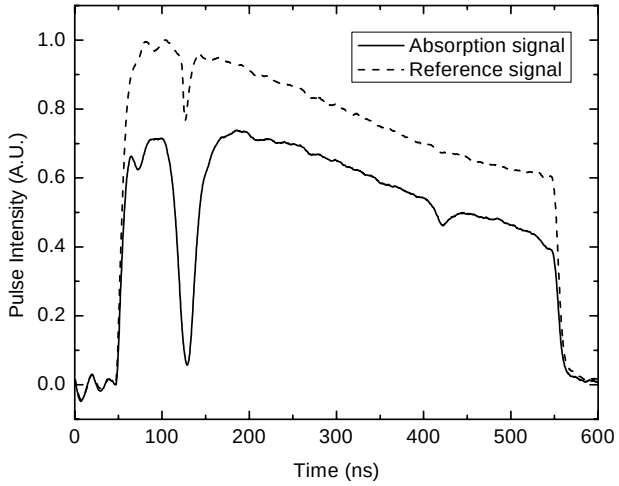

Figure 4.9: Reference signal and absorption signal of the 213m multi-pass gas cell measurement

The time sampling domain can be converted to the wavelength based on the chirp conversion discussed in chapter 4.2.2. In order to analyze these measurements we need to match the measurement spectrum to the theoretical absorption spectra [9]. To do this the atmospheric pressure and temperature broadened monochromatic absorption spectrum (1ppm and 1m path-length) was generated using GENSPECT toolbox with HITRAN2000 database. The Gaussian instrument function, whose width was calculated based on the chirp analysis of section 4.2.2, was convoluted with the monochromatic absorption spectrum to obtain the relevant per unit concentration synthetic spectrum. Once convert to absorbance, the path-length of measurement was included in reference spectrum as a simple multiplication as shown in equation 4.9.

$$A_{ref}(v) = [A_{mono}(v) \otimes f_{ILS}] \times L \tag{4.9}$$

where $A_{ref}(v)$ is reference absorbance spectrum, $A_{mono}(v)$ is monochromatic absorption spectrum, f_{ILS} is instrument function, and L is the path-length.

Using generalized linear model regression, measurement spectrum was compared with reference spectrum to calculate H_2O concentrations. Figure 4.10 shows the measurement absorbance spectrum and reference absorbance spectrum.

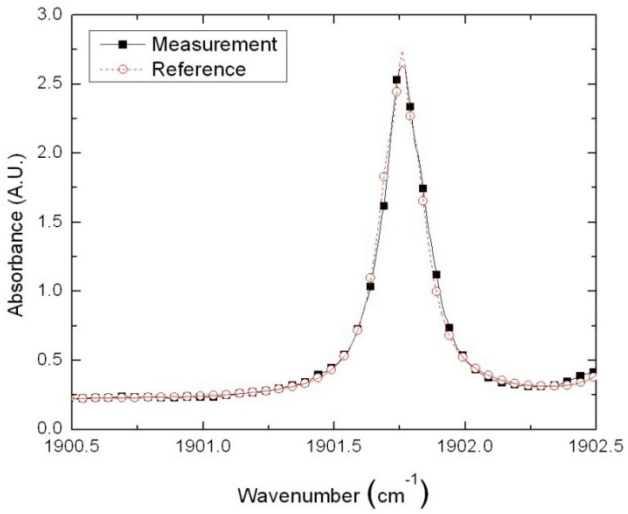

Figure 4.10: Spectral fitting of measurement spectrum with synthetic reference spectrum

Figure 4.10 shows the fitting of the measurement spectrum with theoretical reference spectrum and it has R^2>.99 (R^2 value range from 0 to 1). In this particular experiment, a nonlinear fitting (extension of Beer's law) gave better retrieval due to H_2O strong absorption peak with long path-length which gave >2.5 absorbance signal. From the calculation the resulting the H_2O concentration in the laboratory room was $9.9x10^4$ ppm.

4.3. Field Measurements

The 5.3 μm QCLOPS-CCNY was tested in a number of field measurements as shown in table 4.1. These measurements were performed over absorption path-length from 13 m to 120 m with a 3.64 mW of QCL average peak power. Based on accumulated observations, it can be stated that the optimal absorption path-length for this system using QCL with 50mW output power (14 times current QCL output power) is ~ 1.5km.

Date	Purpose	Location	T_{QCL}(°C)/ L(m)
April 15, 2010	T* and L* configuration	Roof of Steinman	-5, 0, 5, 10, 15, 20/20, 40, 60
April 29, 2010	Different L, 2½ hr continuous measurement	Roof of Steinman	-5/20, 40, 60
May 8, 2010	System noise analysis	Lobby of Steinman	-5/40
May 16, 2010	Long path-length, system noise analysis, 2½ hr continuous measurements	140th St. & St. Nicholas Park	-5/40, 60, 100, 120
May 25, 2010	Side-by-side measurements (QCLOPS vs. OP-FTIR), 5½ hr continuous measurement	Roof of Steinman	-5/40 (QCLOPS) 20 (OP-FTIR)

Table 4.1: Summary of field measurements using QCLOPS-CCNY (T* means temperature of QCL chip and L* means the absorption path-length)

4.3.1. Operating Temperature and Path-length Configuration

Introduction

These measurements were carried on to define laser operating temperature and receiving signal strength in various absorption path-lengths. We set up the QCLOPS at the roof of the engineering building (Lat. 40.8215N, Long. 73.9479W) at the City College and recorded several sets data under different conditions (different path-lengths: 20m, 40m and 60m, and different laser chip temperature: -5, 0, 5, 10, 15, 20 and 25˚C) that allow us to observe the different absorption spectra in various frequency ranges. Because of the available QCL's frequency range, the instrument, from this measurement, provided the concentration of water vapor up to 60 m line-of site distance (L=120m).

Pre-measurement analysis

We run the GENSPECT codes for the transmission of H_2O in the frequency range of 1890-1910 cm^{-1}. As shown in figure 4.11, we can sweep the QCL along ~1897.5 cm^{-1} peak (labeled as 1) and 1901.8 cm^{-1} peak (labeled as 2).

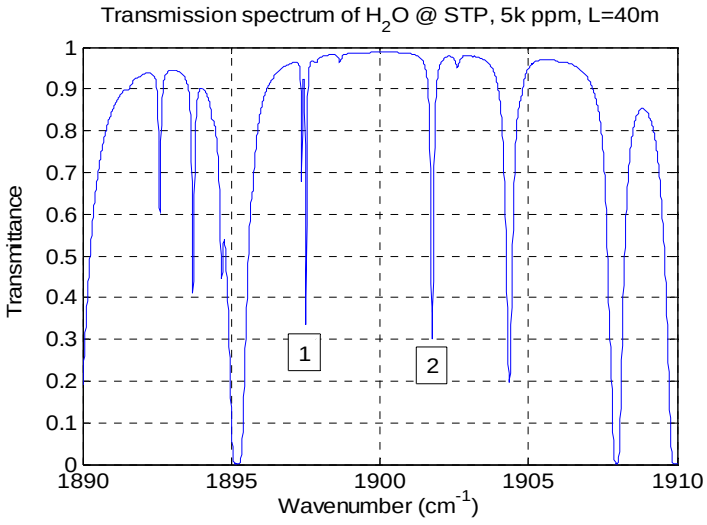

Figure 4.11: GENSPECT generated theoretical transmission spectrum of water vapor

Instrument Setup

The instrument and its accompanying control electronics, power supply and data acquisition and analysis computer were set up at the building roof and the retroreflector was placed 60 m away from the instrument. Figure 4.12 is a photo of the instrument location and surroundings.

Figure 4.12: Photo of the instrument setup

The alignment was made for the QCL and visible trace beams by repositioning to obtain maximum returned signal when we move the retroreflector to the given target distances.

Measurement results and discussion

Measurement spectra were obtained using fast sweep direct absorption spectroscopy with the following QCL parameters.

QCL = DFB pulsed QCL (model#: DQ5-M575R from Maxion)

Temperature on QCL chip = -10˚C, -5˚C, 0˚C, 5˚C, 10˚C, 15˚C, 20˚C, and 25˚C

Pulse width (frequency) = 500ns (40 kHz), 1µs (20 kHz)

Applied voltage = 12V

Each scan consisted of 1000 individual points with 250MS/s sampling rate and we averaged 512 pulses for each recorded data. First, we found that some background features appeared at the front and end of the laser pulse in the measured signals as shown in fig. 4.13A. To remove these fluctuations, we saved the background signal (fig. 4.13B) which could be seen when the QCL beam was blocked. Subtracting the background signal from measured signals eliminated nearly all such features from the measurements illustrating that the background ringing is mainly systematic. Figure 4.14 shows the background eliminated signal of figure 4.13A.

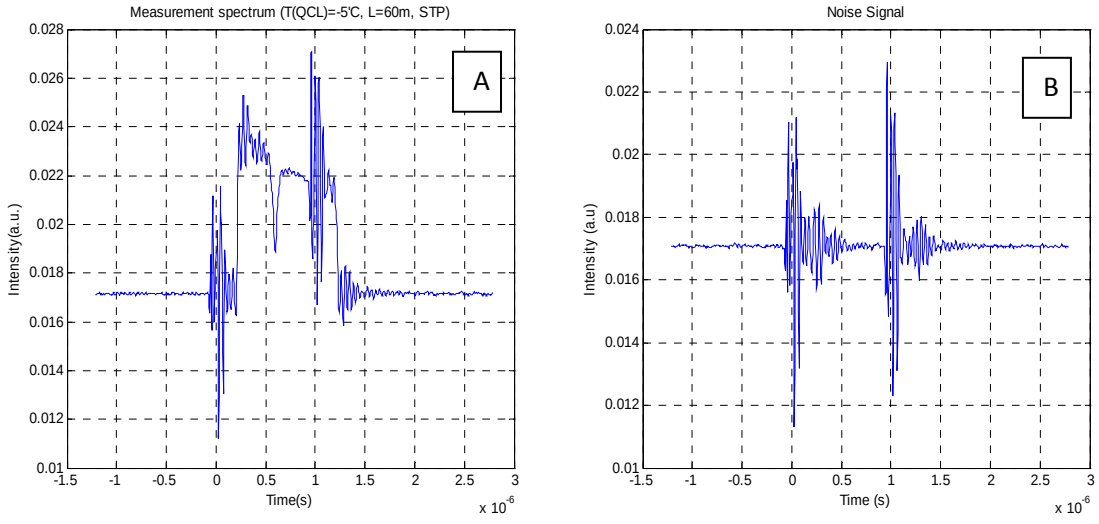

Figure 4.13: Measurement spectra, (A) received signal with 60m path-length, (B) recorded background signal

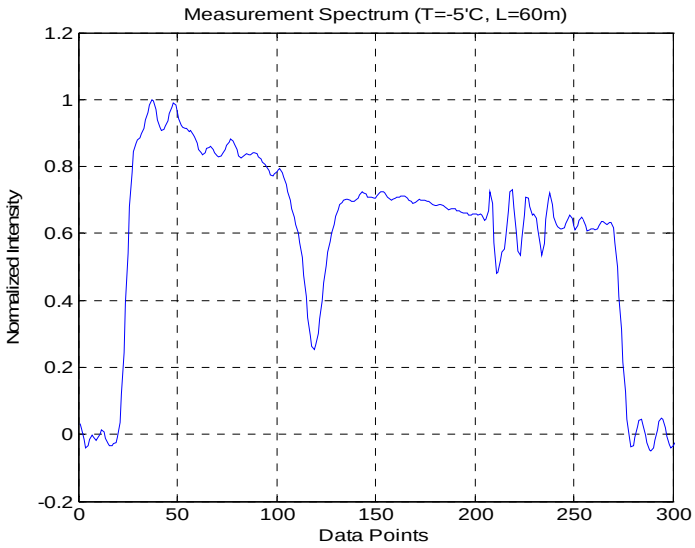

Figure 4.14: Background eliminated signal of fig. 4.13A

We recorded several signal data during the measurements and we found that frequency ranges of the two set of measurements with QCL temperature 25˚C and -5˚C covered water vapor absorption peaks at 1897.5 cm^{-1} (fig. 4.15) and 1901.8 cm^{-1} (fig. 4.14). However, we chose the measurement with -5˚C because its absorption dip appeared in the middle of the pulse and was less effected by the unusual ringing features of the signal background.

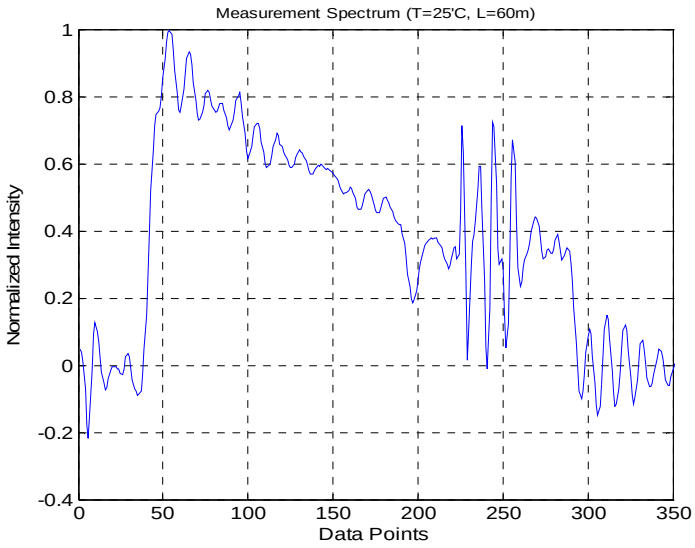

Figure 4.15: Measurement absorption spectrum using laser temperature of 25˚C. An absorption peak can be seen near 200th data point.

We used measurement data with the laser temperature -5˚C and path-lengths 40m and 60m to calculate the water vapor concentration in the air.

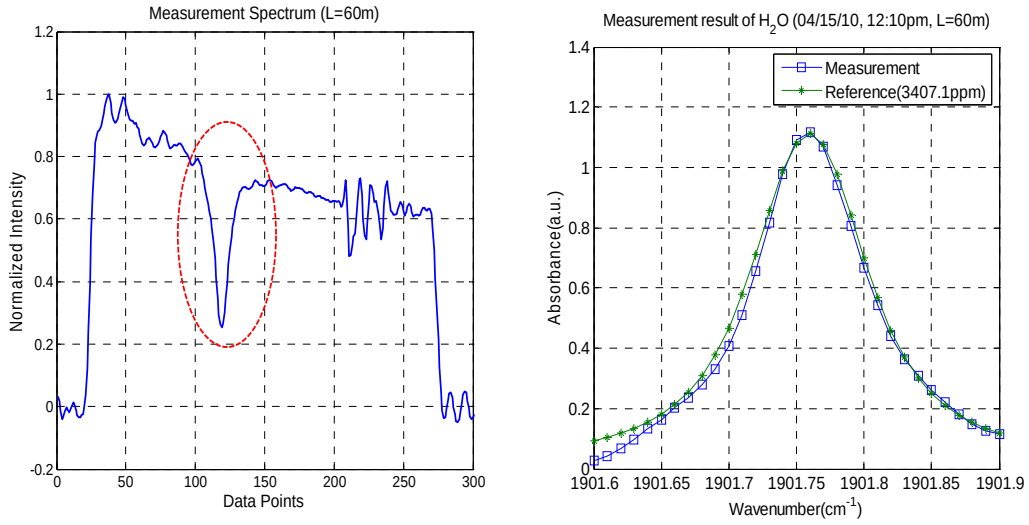

Figure 4.16: The measurement signal (left), absorption spectra of (L=60m) measurement and (L=60m, concentration =3.4071x10^{3} ppm) reference (right)

Figure 4.16 and 4.17 show the measured absorption spectra with reference spectra of 3407.1ppm and 3376.1ppm H_2O concentration for 60 m and 40 m path-lengths respectively.

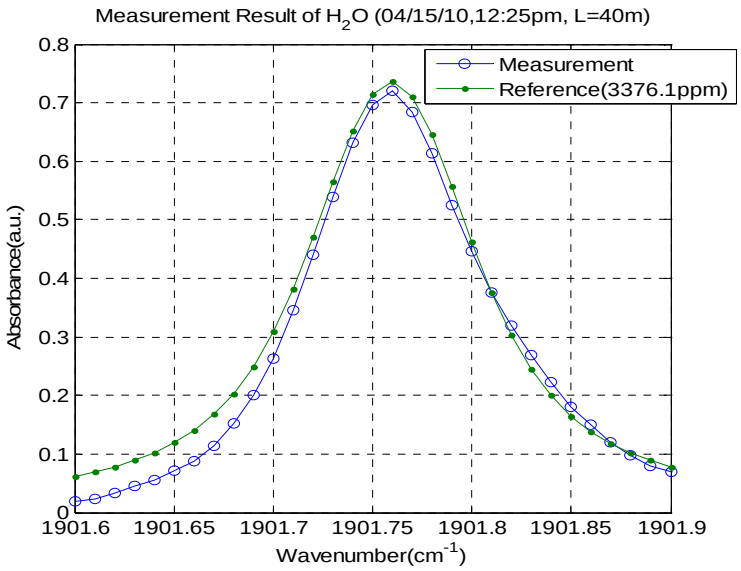

Figure 4.17: Absorption spectra of (L=40m) measurement and (L=40m, conc. =3.3761 x 10^3 ppm) reference

The linear least squares (LSQ) analysis was applied to L= 60m and L=40m measurements to calculate the H_2O concentrations (the process was explained in chapter 2.3.2). The fits are quite good as shown in figure 4.16 and 4.17 at the higher wavenumber end and around the peak of the absorption spectra, but some difference at the lower frequency end of the signal. The reason is that the QCL's frequency tuning rate is not constant (slower at pulse or lower wavenumber) along the pulse, but a fixed tuning rate (0.0025 cm^{-1}/ns) with 250 MS/s sampling rate (4 ns interval) was used in this analysis.

Confirmation of this water vapor concentration could be obtained by comparing to weather data. In particular, given the temperature and relative humidity RH at the time of measurement, which was obtained from the collocated CCNY weather station located ~350m to the south of our QCL measurement site and on a ~15m higher than rooftop, we calculated concentration of water vapor in the air [10, 11]. The calculated H_2O concentration from the weather station data and calculated H_2O concentration from QCLOPS measurements are listed in table 4.2.

Time	**Data from CCNY Weather Station**					**QCLOPS measurement**
	Wind Speed(m/s)	T(□C)	R.H. (%)	Air Press. (mbar)	H_2O Conc. (ppm)	H_2O Conc. (ppm)/L(m)
12:10pm	100.4	18.87	15.29	1011.7	3253.47	3407.1/60
12:25pm	100.8	18.43	15.33	1011.7	3173.30	3376.1/40

Table 4.2: Comparison of results based on data from CCNY weather station and data from QCLOPS measurements

The analysis shows that the QCLOPS's result is higher than results using weather station data with less than 5% and 6% for the 60 m and 40 m path-length measurements respectively.

4.3.2. Comparison between QCLOPS and OP-FTIR measurements

Introduction

These measurements deserve particular attention for several reasons:

1. Side-by-side measurements by the two systems, QCLOPS-CCNY and open-path Fourier Transform Infrared System (OP-FTIR) were performed over comparable absorption paths
2. Measurements were carried over a continuous 5½ hours time period
3. The results from these two systems were compared with the closest weather station data.

Experimental Setup

The measurements were undertaken during the warm, windy conditions of May 25, 2010 at the roof of the Steinman building, CCNY. A shelter, (10ft-square tent) was built to protect the systems, particularly the QCLOPS, against the direct Sun light for a 5½ hour long measurement period. The performance of OP-FTIR from MIDAC [12] was tested several times in previous studies [13], and its H_2O concentration measurements were suitable to compare with the QCLOPS measurements. Figure 4.18 shows the setup of two system telescopes direction and light source paths to them. The retrieval method of H_2O concentrations from OP-FTIR and QCLOPS measurements were explained detail in reference 13 and chapter 2.3.1 respectively.

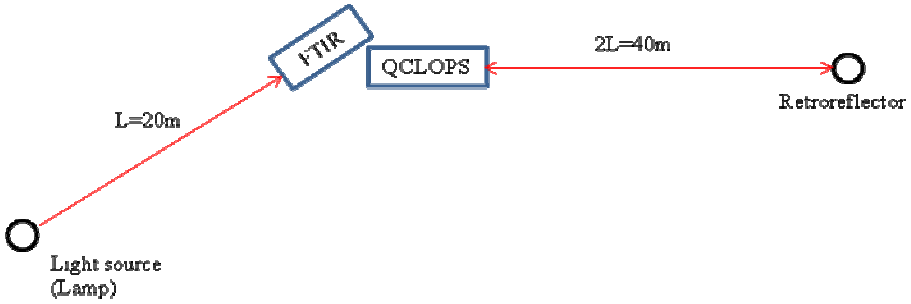

Figure 4.18: The positions of two systems, QCLOPS and OP-FTIR, and their absorption path-lengths (20m for OP-FTIR and 40m for QCLOPS)

Figure 4.19: Photos of two systems (QCLOPS and OP-FTIR) describing system telescopes and light source/retroflector positions with optical path-lengths

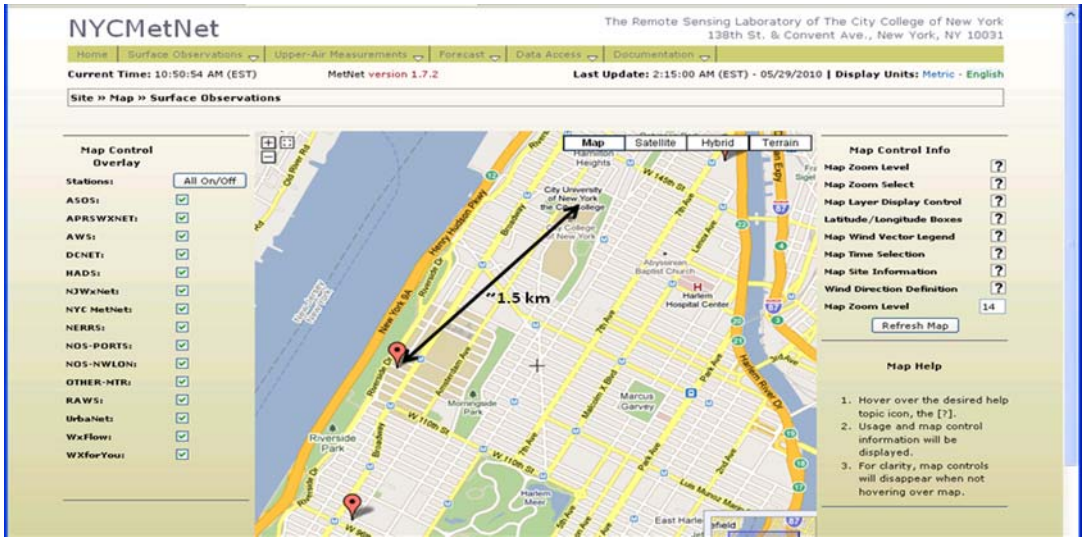

We downloaded measurement day's weather data, such as ground level

temperature, air pressure, and relative humidity (RH) from the closest weather station (ID: NWSTH) [3] which is ~ 1.5 km away from our measurement site and located near the Hudson River. Then, we calculated H_2O concentrations [4] using these data for the comparison of QCLOPS and OP-FTIR results. However, the data with sudden large changes of RH (>5%), wind direction (>50˚) and wind speed in a short time (<15 min) were not included in this analysis.

Results and Discussions

The absorbance spectra of H_2O calculated from measurement signals using QCLOPS-CCNY and OP-FTIR are presented in figure 4.20 and 4.21. The fits between measurement and reference spectra for QCLOPS appeared to be better than those in OP-FTIR system where the combination of H_2O and CO (carbon monoxide) absorption was used in spectrum fitting at 2152-2166 cm^{-1} range.

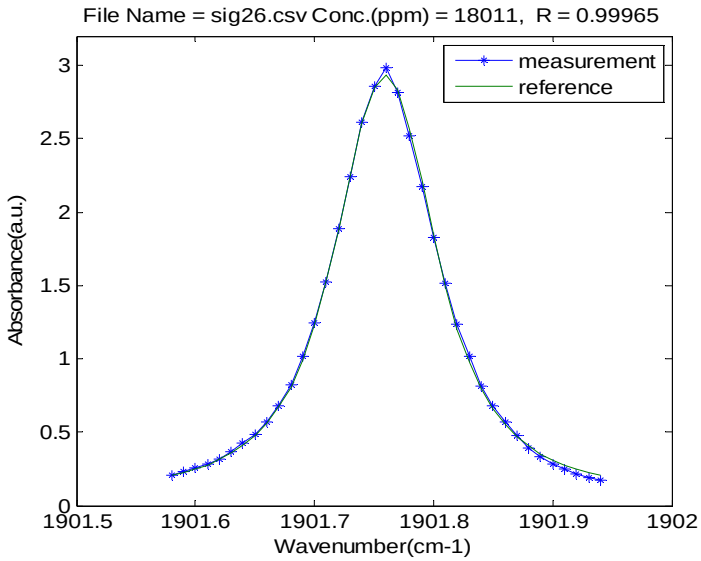

Figure 4.20: The measurement result, H_2O concentration and spectrum fitting of measurement and reference absorption spectra

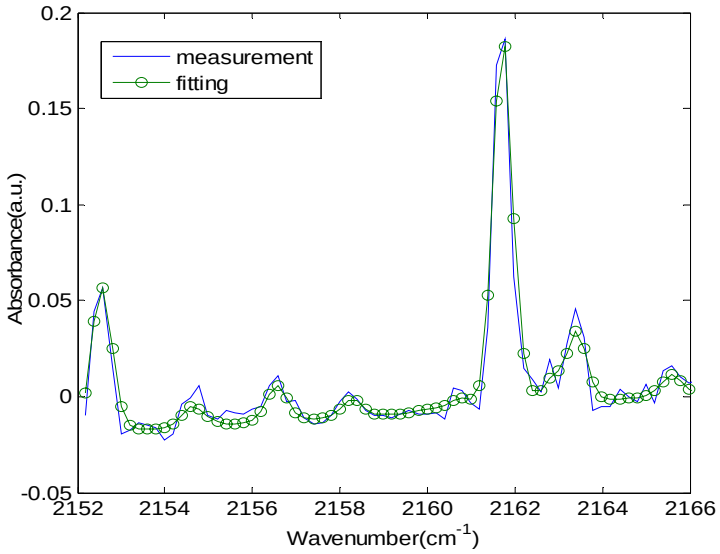

Figure 4.21: OP-FTIR measurement and reference fitting spectra

The results from QCLOPS and OP-FTIR are shown in figure 4.22 along with the weather station result.

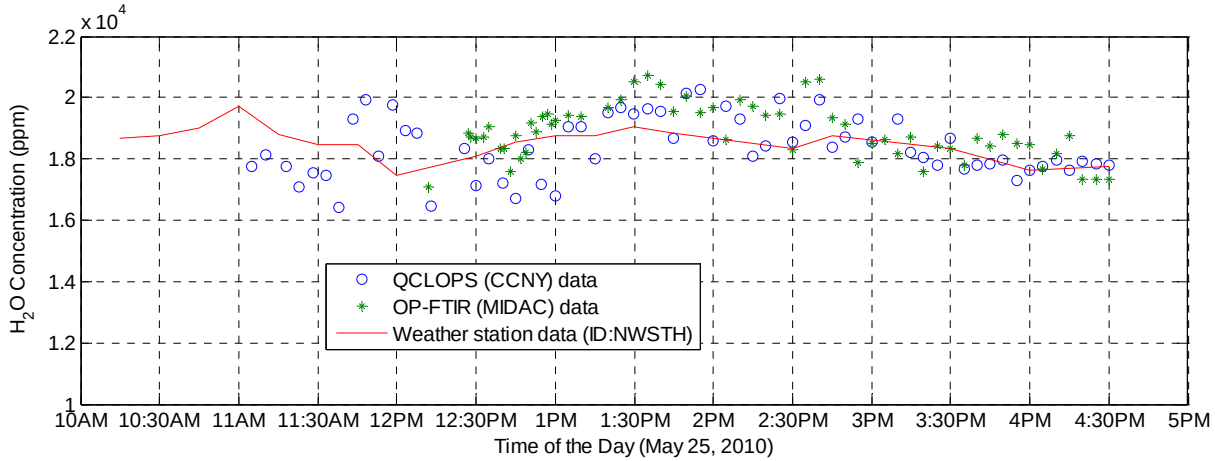

Figure 4.22: Comparison of QCLOPS, OP-FTIR and the weather station data results

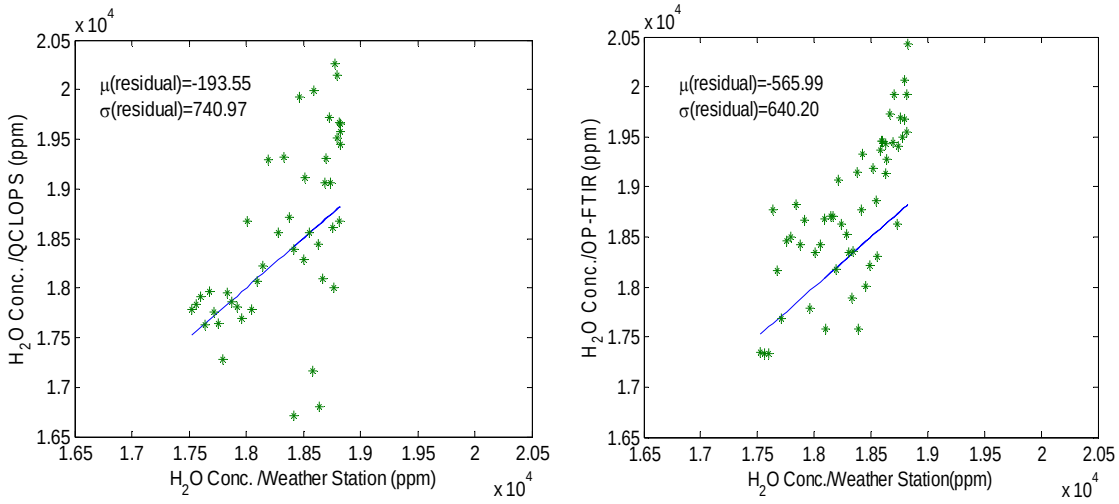

Figure 4.23: Scatter plots weather station result against QCLOPS result (left), and weather station result against OP-FTIR result (right)

We analyzed QCLOPS result and OP-FTIR result against weather station data, and statistics of the results were presented in figure 4.23. Residuals were calculated from the difference between weather station result and QCLOPS result/OP-FTIR result, then, calculated mean and standard deviation of the residuals. The result shows that means of residuals for QCLOPS and OP-FTIR system are 194 and 566 respectively. However, OP-FTIR gave smaller standard deviation values than QCLOPS's. The reason may be the better stability of the system or larger spectral range.

In conclusion, our results demonstrate the comparable performances of the QCLOPS-CCNY with a commercially developed open-path FTIR system. Because current QCLOPS has higher resolution (0.018 cm^{-1}) than OP-FTIR MIDAC system's (0.5 cm^{-1}), the QCLOPS-CCNY will have ability to detect ozone and ammonia concentrations which needs high resolution sensor system when used QCL with a suitable frequency range (1045-1047 cm^{-1}).

4.3.3. Measurements to Quantify QCLOPS System Noise

Introduction

The QCLOPS takes advantage of longer path-length to decrease limit of detection of the gas concentration. The maximum path-length of the system is defined when the SNR is large enough to retrieve the gas concentration in required accuracy. Therefore, quantifying system noise level at a per-pulse is needed to assess the QCLOPS system. The analysis must recognize noise from many sources, such as detector, pre-amplifier, power supply, cooling system, and data acquisition card. Detail of theoretical noise level calculation was explained in chapter 3.4.6.

Using component parameters in table 3.1, we calculated our QCLOPS system has total noise level of maximum 1.0 mV at 40 m or a longer absorption path-length. The noise depends on path-length because the quantization noise and SIND are dependant on the signal level.

Experimental Setup

We set up the QCLOPS system at the lobby of the Steinman Hall at the Engineering building on May 8, 2010 with the following system parameters. We arranged to get small collected signal (<50mV) so that the intensity of noise and signal can be simultaneously observed in a small dynamic range.

QCL: T_{chip} = -5˚C, pulse width = 1μs, pulse repeating rate = 40 kHz

Path-length = 20 m with 2.5” retroreflector

The outdoor measurements were done in front of the Steinman Hall using the same QCLOPS operating parameters but longer absorption path-length (120m).

Results

In indoor measurement, we recorded total of 422 measurements of individual samples with 10,000 sampling points and example of first two measurements are shown in figure 6.8. We use two techniques (using only two sets of signal measurement data [7] and using numbers of measurement data, e.g. 422 or 512 samples at three points of the signal) to define noise level and SNR of our system. The first two indoor measurements with difference between the signals can be seen in fig. 4.24.

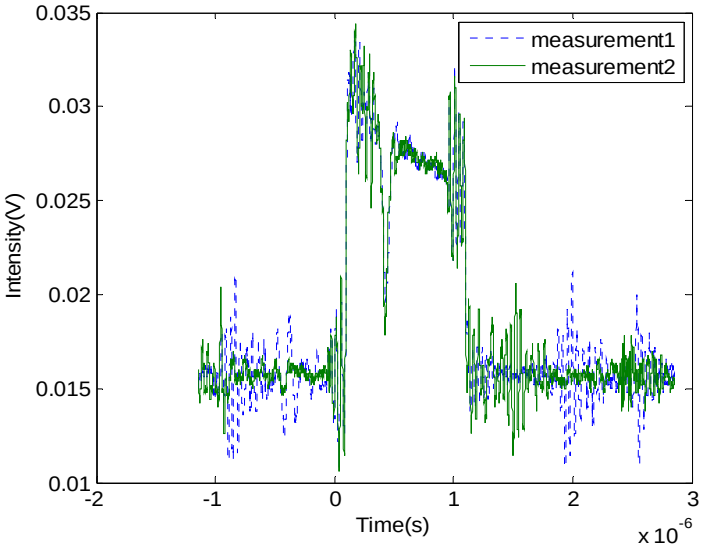

Figure 4.24: Measured signals of first two samples using QCLOPS

The signal to noise ratios (SNR) of the measurements was calculated using the method, which is explained in reference 14, where the SNR is defined as the instrument's ability to obtain the same measurement result if the same measurement conditions are repeated in different time. The noise level is calculated as

$$N(\nu_i) - 1 - \frac{I_1(\nu_i)}{I_2(\nu_i)} \tag{4.10}$$

where I_1 and I_2 are measurement intensities at the frequency of ν_i and then the N_{RMS} becomes

$$N_{RMS} = \sqrt{\frac{1}{n}\sum_{t=1}^{n}[N_t(v_i)]^2} \tag{4.11}$$

where t is repeated number of time for the same measurement conditions. Finally, we calculate SNR as

$$SNR = \frac{1}{N_{RMS}} \tag{4.12}$$

and noise voltage

$$V_n = \frac{V_{sig}}{SNR} \tag{4.13}$$

The portion of the signal which we used in this analysis is shown with a red box in figure 4.25 (from 50 ns to 950 ns). We calculated SNR and noise voltage from the indoor measurements. We also analyzed noise level at the beginning, minimum, and at the end of the absorption feature and they were labeled as P1, P2, and P3 in figure 4.25.

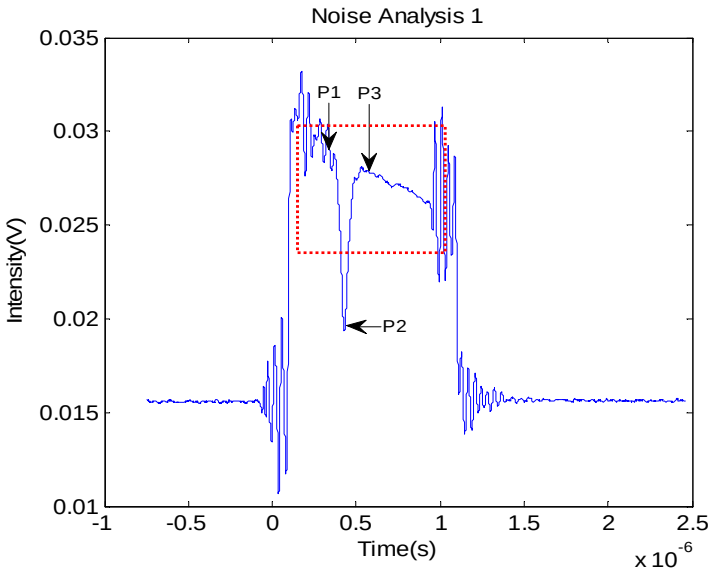

Figure 4.25: The positions of three points (P1, P2 and P3) and analyzed signal part (red box)

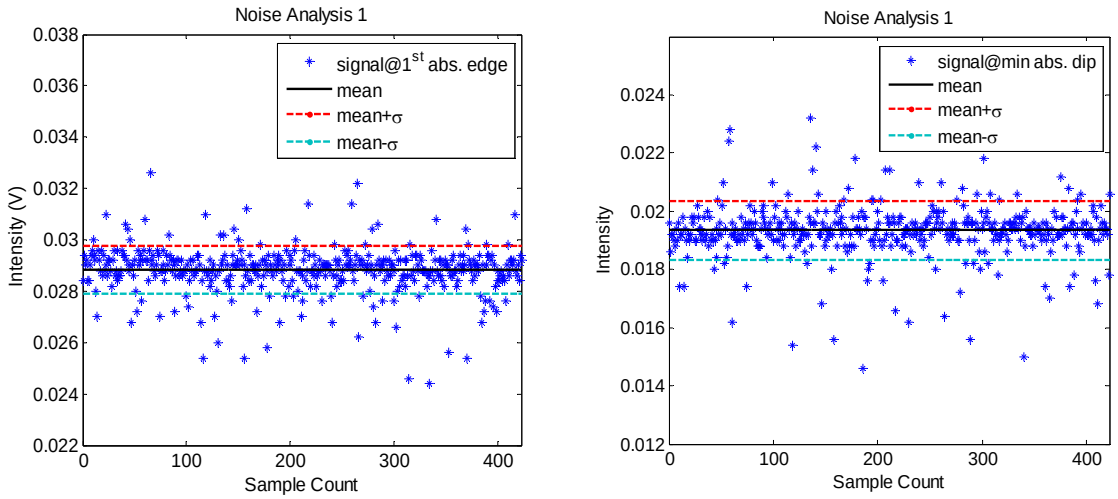

Figure 4.26: Mean and standard deviation of indoor measurement signal at P1 (left) and P2 (right) (see fig. 4.25)

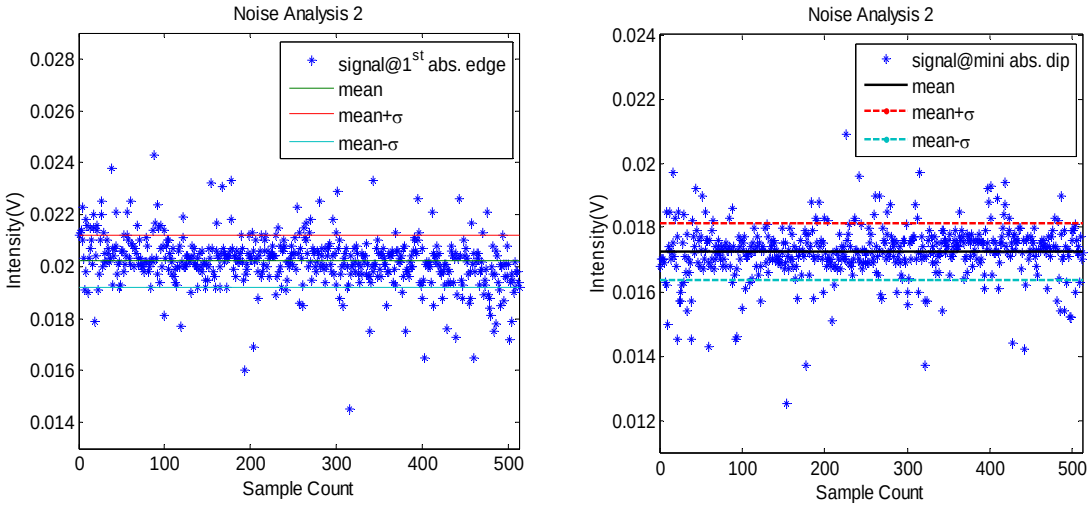

Figure 4.27: Mean and standard deviation of field measurement signal at P1 (left) and P2 (right) (see fig. 4.25)

The results of indoor and outdoor noise analysis measurements are summarized in table 4.3.

	Indoor meas.(mV)				Outdoor measu.(mV)			Theoretical(mV)
Types	**Averaged over area**	**P1**	**P2**	**P3**	**P1**	**P2**	**P3**	**Of the System**
μ	28.0	28.8	19.3	28.1	20.2	17.3	20.0	26.9
σ	1.4*	0.9	1.0	1.0	1.0	0.9	1.0	1.0**
SNR	20.4	30.5	19.3	29.0	19.9	19.8	20.5	26.9

Table 4.3: Comparison of noise level from QCLOPS indoor and field measurements (1.4*: noise voltage calculated using technique 1, 1.0**: noise voltage at L=40m)

Discussions

The theoretical result and both indoor and outdoor measurement results of noise voltages are almost the same level (0.9 – 1 mV). The noise voltage calculation using part of the two individual signals gives 1.4 mV (table 4.3, column 2) and provides an upper limit of the noise. We can also improve SNR by sample averaging which reduces random noise (white noise) as shown in equation 4.14 [14].

$$SNR_n = SNR_0 \times \sqrt{n} \tag{4.14}$$

where 'n' is number of averaging samples, and SNR_n is SNR value after 'n' time averaging. For example if we use 512 times averaging for per pulse SNR = 20.4, SNR_{512} becomes 462.

In conclusion, the QCLOPS-CCNY system noise was quantified through both by simulation and observations. The measurement values have a good agreement with our previously calculated theoretical results; however, there may be some background noise

during outdoor measurements. These measurements allow us to understand the system performance and to improve the sensitivity of the QCLOPS and predict the performance for the ozone-ammonia system.

4.4. Validating the Link Power Analysis Model using QCLOPS Field Measurements

4.4.1 Required SNR for 5.3 µm Window

First, the GENSPECT simulation with multivariate least squares analysis was performed to calculate ambient concentration retrieval error as a function of SNR (called required SNR) for water vapor (H_2O), carbon dioxide (CO_2), ozone (O_3), and ammonia (NH_3) based on spectral values from the HITRAN database [chapter 3.1].

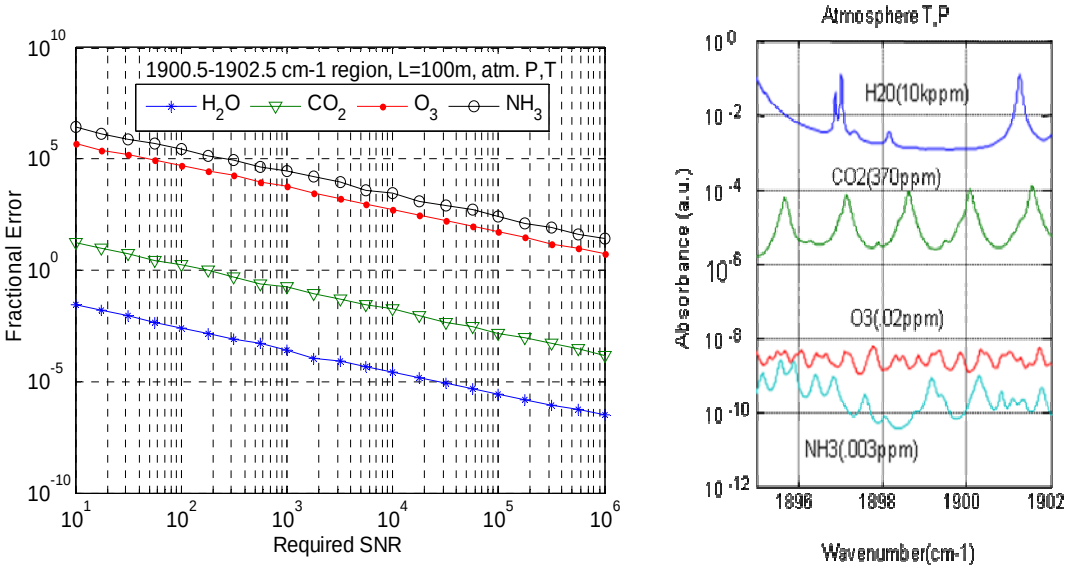

Figure 4.28: Required SNR for H_2O, CO_2, O_3 and NH_3 vs. fractional error (left) and absorbance spectra of H_2O, CO_2, O_3 and NH_3 in ambient concentration, atmosphere temperature and pressure (right)

Figure 4.28 shows that the analysis of O_3 and NH_3 concentrations in this spectral region (1900.5 – 1902.5 cm^{-1}) is not possible, but the concentration of H_2O can be retrieved in 1% accuracy with SNR of 30.

4.4.2. Model Simulation

The absorption loss was calculated from the transmittance, which was generated using GENSPECT and HITRAN database, at the wing of the strong absorption feature of H_2O near 1901.8 cm^{-1} as shown in figure 4.29. At the 40 m path-length absorption loss is ~0.8974 and at 120 m path-length, absorption loss becomes 0.723.

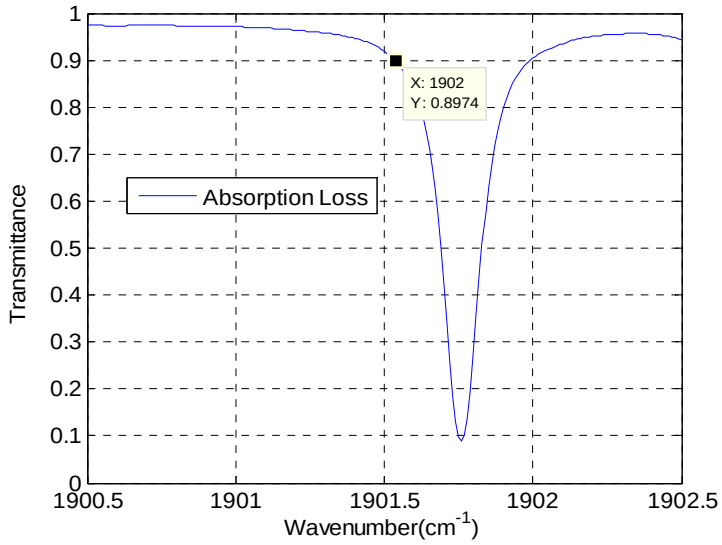

Figure 4.29: Absorption feature of H_2O in L = 40 m

The particle scattering loss and atmospheric turbulence loss are shown in figure 4.30 as a function of path-length. The maximum loss due to scattering and turbulence are 0.997 and 0.969 respectively at path-length of 120 m. Since the QCL beam which we used in the QCLOPS has 4mm diameter and the calculated divergence limit was 2.53mrad (divergent limit was explained in chapter 3.4.4), it was reasonable to apply laser beam divergences of 3mrad and 4mrad (18% and 58% above the divergence limit)

to see if it explained the power drop-off observed in the Water Vapor QCL measurements.

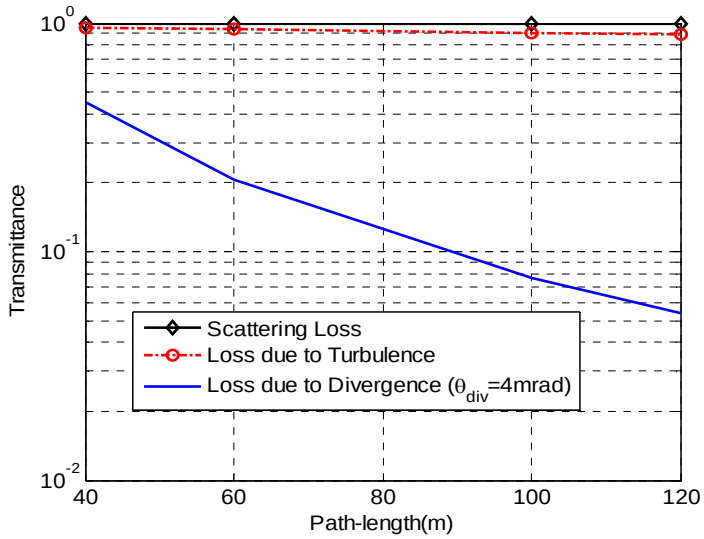

Figure 4.30: Particle scattering loss, turbulence loss and free space loss as the function of path-lengths

Total loss was calculated by multiplying all those losses (scattering loss, atmospheric turbulence loss, absorption loss, free space loss and system optics loss) and finally, returned signal voltages were obtained using laser output power and total loss of the system. The model was also used to calculate the system noise and as explained in chapter 3.4 and total system noise voltage is calculated as in equation 4.15.

$$V_{N,total} = \sqrt{[G \times (V_{N,\det} + V_{N,amp})]^2 + V_{N,DAQ}^2} \tag{4.15}$$

The result of the noise analysis is shown in figure 4.31 as the DAQ noise is dominant for L ≤ 100m.

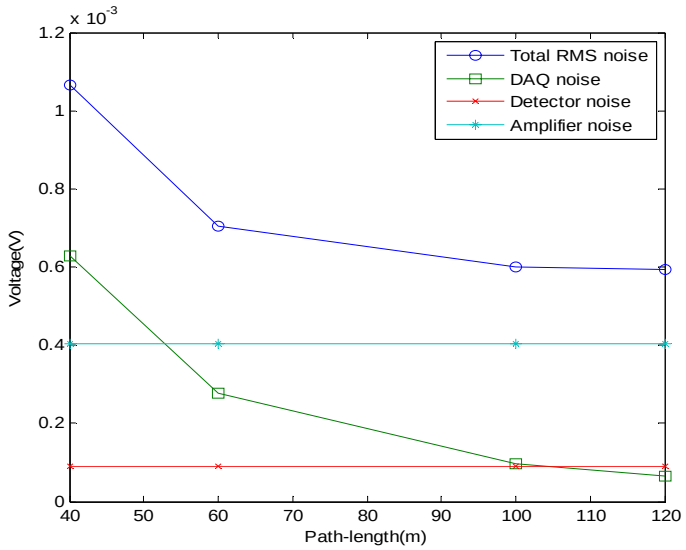

Figure 4.31: The model simulation result of total RMS noise and noise voltages from detector, pre-amp and DAQ system as the function of path-length. The noise voltage curves (total RMS noise and DAQ noise) are not continuous because they are calculated from the noise voltage of received signal for 40m, 60m, 100m, and 120m path-length (coarse interval).

4.4.3. Comparison of OPSM and Measurement Results

The returned voltages from the OPSM and QCLOPS-CCNY field measurement are plotted in figure 4.32.

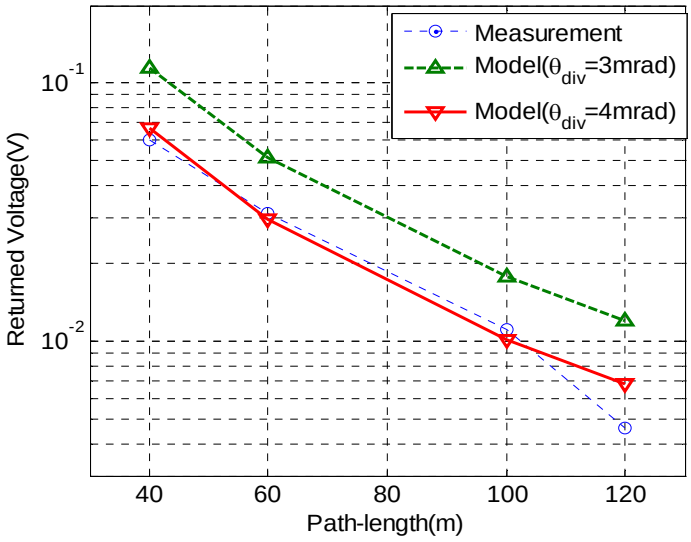

Figure 4.32: Comparison of 5.3μm measurement and model results (4 mrad and 3 mrad QCL beam divergences on model calculation)

From the results, we see that the 4 mrad divergence best explains the power drop and as such will be used in all analysis of the 5.3μm QCLOPS. Table 4.4 compares the calculated per pulse SNRs using the model and from measurement data for 40 m, 60 m, 100 m and 120 m path-lengths.

Path-length(m)	SNR(meas.)	SNR(3mrad div.)	SNR(4mrad div.)
40	60.37	68.38	60.88
60	44.36	55.18	40.27
100	22.97	26.92	16.11
120	6.57	18.87	11.00

Table 4.4: Comparison of SNRs calculated by the model and measurements

It is interesting to see that the best fit to the noise data occurs when we use the 4mrad value which is a nice consistency check.

In conclusion, this analysis provides confidence on the open-path system model because the results from the model have good agreements with measurements. And it also leads to prove assessment of open-path ammonia-ozone detection system using this model.

References

[1] T. Ball, "Water vapor is the most powerful greenhouse gas", at http://www.skepticalscience.com/water-vapor-greenhouse-gas.htm

[2] P. Corrigan, M. Lwin, B. Gross, F. Moshary, "Design of an ozone and ammonia open-path sensor with a quantum cascade laser", prepared to submit to a technical journal

[3] Infrared detector catalog from Vigo System S.A. at http://www.vigo.com.pl/index.php/en/english_menu/products/ir_detectors

[4] F. Pedrotti, L. Pedrotti, L. Pedrotti, "Introduction to Optics", 3rd ed., Benjamin Cummings, (2006).

[5] E. Normand, M. McCulloch, G. Duxbury, N. Langford, N., "Fast, real-time spectrometer based on a pulsed quantum-cascade laser", Optics Letters **28**, 1 (2003).

[6] M. McCulloch, E. Normand, L. Langford, G. Duxbury, D. Newnham, "Highly sensitive detection of trace gases using the time-resolved frequency downchirp from pulsed quantum-cascade lasers", J. Opt. Soc. Am. B **20**, 8 (2003).

[7] J. McManus, P. Kebagian, M. Zahniser, "Astigmatic mirror multipass absorption cells for long-path-length spectroscopy", Applied Optics, 34 (18), 3336-3348 (1995)

[8] http://www.aerodyne.com/products/amac/astigmatic_absorpt.htm

[9] P. Corrigan, M. Lwin, R. Huntley, A. Chhabra, F. Moshary, B. Gross and S. Ahmed, "Portable open-path chemical sensor using a quantum cascade laser", Proc. SPIE 7312, 73120P (2009)

[10] The NYCMetNet surface data by the Remote Sensing Laboratory of The City College of New York at http://nycmetnet.ccny.cuny.edu/Data-Download_Surface.asp

[11] R. Heinsohn, and J. Cimbala, "Indoor Air Quality Engineering: Environmental Health and Control of Indoor Pollutants (Drugs and the Pharmaceutical Sciences)", 1st ed., CRC Press (2003)

[12] Open-path FTIR Air Monitoring System, Supplement Manual by MIDAC Corporation

[13] V. Vladutescu, B. Gross, F. Moshary, and S. Ahmed "Assessment of a QCL Laser Approach for the Simultaneous Measurement of Ambient Ammonia and Ozone" SPIE Proceedings, 6760-6768 (2007)

[14] V. Saptari, "Fourier-Transform Spectroscopy Instrumentation Engineering", SPIE Press, Washington, (2004)

[15] P. Griffiths and J. Haseth, "Fourier Transform Infrared Spectrometry", 2nd ed., John Wiley & Sons, Inc., New Jersey (2007)

CHAPTER 5: SUPPLEMENTAL STUDY

5.1. Backscattering Measurements of the Urban Building Materials

5.1.1. Introduction

In chapter 3, an analysis of the Ozone-Ammonia system based on retroreflector target was implemented. However, we would like to explore the feasibility of using targets of opportunity instead of having to deploy retroreflectors. The system layout using this idea for a traditional mono-static backscattering system with QCL is shown in figure 5.1.

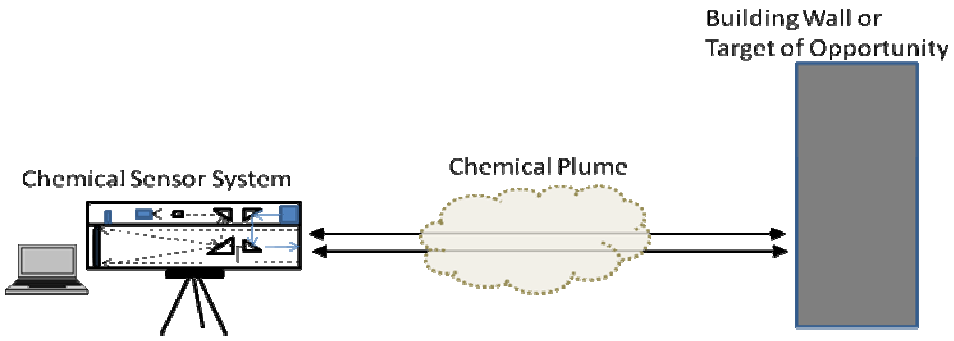

Figure 5.1: Schematic diagram of an active chemical sensor system. Transmitted QCL beam is reflected back by a building wall or a target of opportunity through chemical plume and collected onto a receiver of the system.

As we discussed earlier, the potential of a QCL open-path backscattering ozone and ammonia detection system was analyzed [1], but this analysis did not take into account realistic reflection properties of possible targets of opportunity. This section fills that hole by making practical measurements of the angular reflectance that can be used to calculate the effective albedo of a reflecting target.

5.1.2. Theoretical Background

The albedo or reflectivity of a surface depends on the material, the incident and outgoing geometries, surface roughness and the frequency of incident beam. In Lambertian (diffuse) reflection, under normal illumination, the scattered light is a function of the angle between the surface normal and observer's line of sight and can be stated as

$$I_\theta = I_0 \cos\theta \tag{5.1}$$

where I_θ is reflected intensity, I_0 is reflected intensity normal to the surface and θ is the angle between the observing direction and normal to the surface. In reality, no surface is a perfect Lambertian reflector but for sufficiently rough surfaces, the Lambertian model can be used as a first approximation [2, 3]. On the other hand, specular reflection will occur from a highly polished surface, similarly to a mirror. Realistically, materials will tend to reflect as a combination of specular and diffuse reflectors with different proportions [4, 5].

5.1.3. Experimental Setup

The experimental arrangements of backscattering measurements are shown in figure 5.2 and figure 5.3. In figure 5.2, the DFB pulsed QCL (DQ5-M575R from Maxion) at λ = 5.3μm was driven with a Cascade Technologies QCL control system which stabilized substrate temperature at 0˚C and produced a 1μs pulse at 20 kHz pulse repetition rate. The QCL beam was directed onto the sample with 20˚ incident angle (θ_i) and backscattering signals were detected using a Vigo thermoelectrically cooled mercury-cadmium-telluride (MCT) photovoltaic detector (area 1.6 mm x 1.6 mm, PVI-3TE-10.6)

and recorded with a lock-in amplifier (SR530 from Stanford Research Systems). The laser beam and field of view (FOV) of the detector 9mrad (FOV=D_{det}/path-length) were oriented in the same plane (plane of incidence). The measurements were taken along a 35 cm diameter arc shown in figure 2 with 2˚ steps, and viewing angle from -90˚ to +10˚.

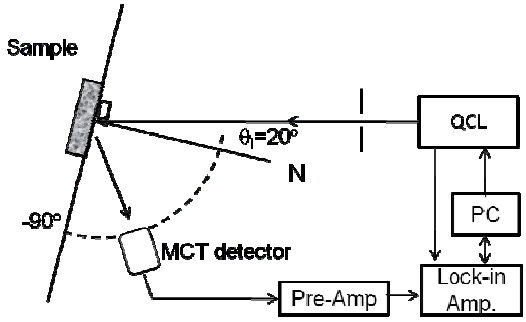

Figure 5.2: Schematic diagram of backscattering measurement setup with QCL and Lock-in amplifier

The setup for backscattering measurements with the FTIR system is shown in figure 5.3. The infrared (IR) source (IR-30 from Hawkeye Technologies) was collimated with a 1 in diameter lens before it reached onto sample surface. The incident angle to the sample surface and reflected angle onto the detector of FTIR system (MIDAC FTIR system) were set to 35˚. We used the reflected signal from the gold coated mirror as a reference and reflectivity for all other sample measurements as stated in equation 5.2.

$$R_{BS,FTIR} = \frac{I_{bk\,scatt}}{I_{ref.,gold}} \tag{5.2}$$

where $R_{BS,FTIR}$ is the reflectivity of the sample using FTIR system, $I_{bk.\,scat.}$ is the measured intensity from the sample and $I_{ref.,\,gold}$ is the reference intensity from gold coated mirror.

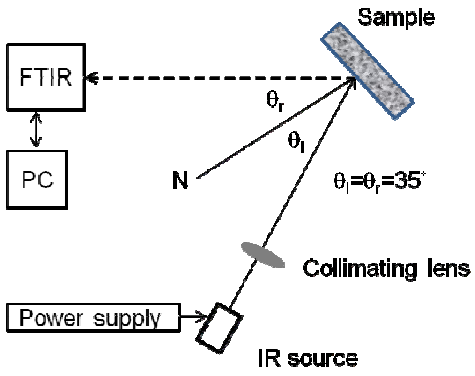

Figure 5.3: Experimental setup with IR source and FTIR

5.1.4. Measurement Samples

A variety of urban building materials, unpolished aluminum (alloy 6061, unpolished mill, ASTM B221, from McMaster Carr), polished natural wall stones - granite (RYG-4XNAPO, Solieque), marble (THDWI-T-GRE, MS International), white ceramic wall tile (U072-44-1M, U.S. Ceramic Tile Co.), aluminum sheets (model # 85068, Amerimax Home Products, Inc.), concrete block and textured wall tile (concrete block and textured wall tile were from a CCNY building construction site) were used in this study. To obtain diffused surfaces with different roughness, three aluminum surfaces were roughened using #220 grit (very fine), #150 grit (fine), and #100 grit (medium) sandpapers (#48132, Norton). We also applied white paint (7790 Flat White, Rust-Oleum) on white ceramic wall tile and textured ceramic wall tile and used them as samples.

5.1.5. Results and Discussion

The reflectivity or backscattering for common urban building wall materials is shown in figure 5.4. Unpolished aluminum exhibits much greater dispersion in reflection as function of angle (i.e. quasi-Lambertian reflection), but as expected, the reflection off of polished granite, polished marble and white ceramic wall tile are much more peaked exhibiting strong specular reflection tendencies. We calculate the peak reflectivity of unpolished aluminum in the specular direction to be 0.154 at 20˚ viewing angle (θ_r) with gradual decreases in reflection of 13% when viewed ±2˚ from θ_r. On the other hand, reflectivity of polished granite, polished marble and white ceramic wall tile have maximum values of 0.029, 0.045, and 0.030 respectively in the specular direction. However, because of their highly specular reflection, reflectivity of white ceramic wall tile decreases ~38% and reflectivity of polished granite and marble decreases up to 94% at the viewing angles of ±2˚ away from θ_r.

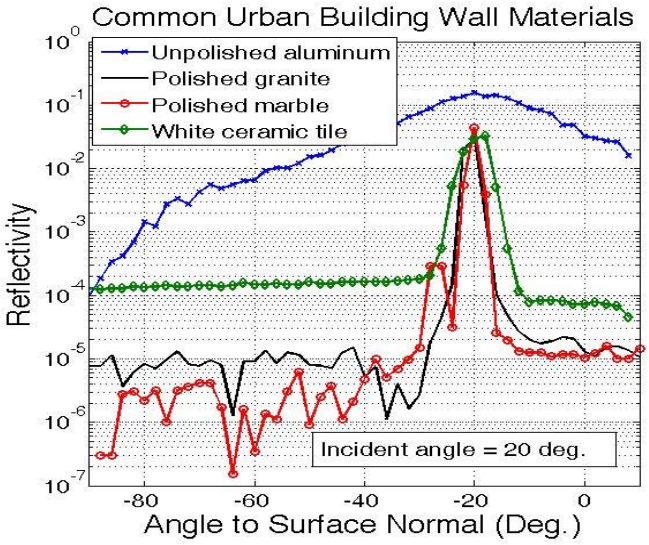

Figure 5.4: Reflectivity of common urban building wall materials with viewing angle from -90˚ to +10˚

In figure 5.5, we present the reflectivity of textured wall tile, concrete block, white painted white ceramic tile, and white painted textured wall tile. This group of materials is very weakly reflective with values of $\leq 6.5 \times 10^{-4}$ at 20˚ viewing angle.

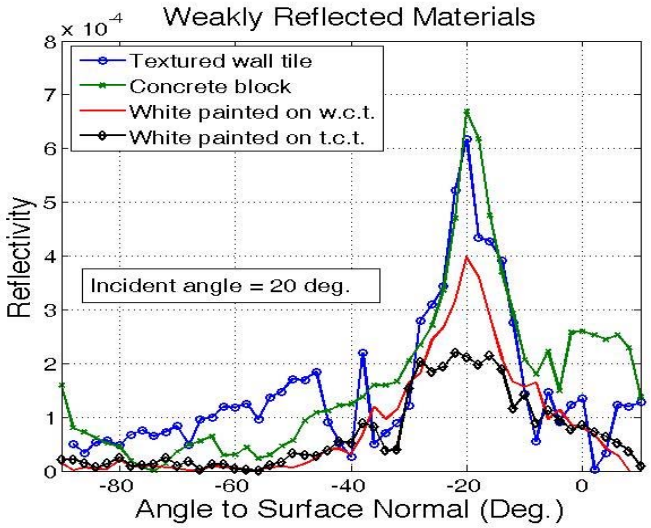

Figure 5.5: Reflectivity of weakly reflected materials

The results of backscatter due to surface roughness are shown in figure 5.6 where polished aluminum surfaces were modified by sanding as explained in section 4. The reflectivity of these samples appears to have a significant specular component reflection with 0.027, 0.032, and 0.015 for sanded surfaces using #200, #150, and #100 grits respectively. Their reflectivity decreases up to 56% when viewing angle moves ±2˚ from direct reflected angle θ_r.

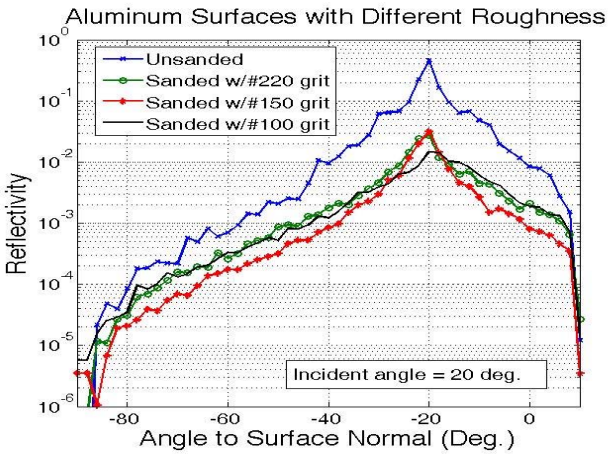

Figure 5.6: Reflectivity of different roughness aluminum surfaces

We evaluated the QCL backscattering results with the measurements using FTIR system. The FTIR measurements give reflectivity of samples with $\theta_{inc} = 35^{\circ}$ wavenumber between 400 cm^{-1} and 3500 cm^{-1}. Figure 5.7(a) shows the measured reflected spectra from gold coated mirror and polished granite. These data are processed as equation 5.2 and the result is shown in figure 5.7(b).

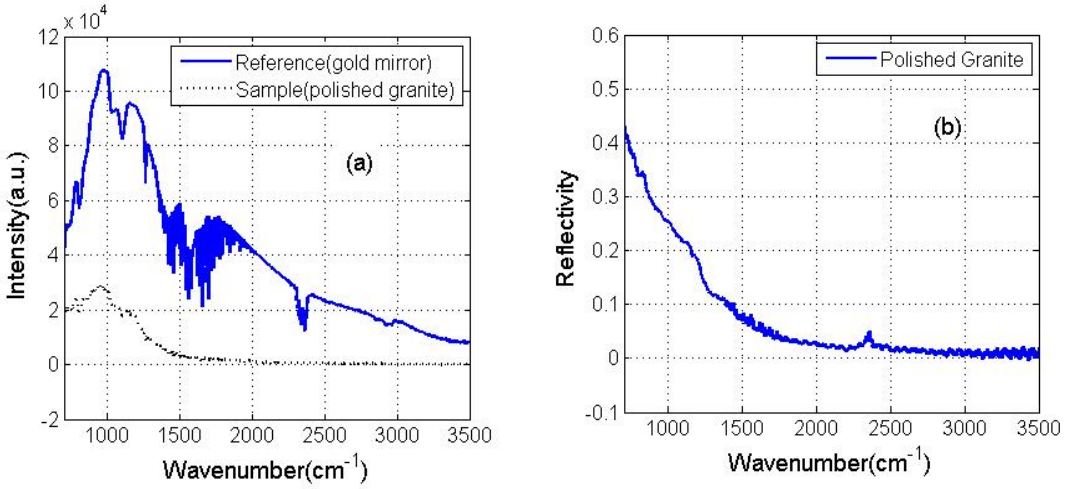

Figure 5.7(a) Reference spectrum (reflected signal from gold coated mirror) and sample spectrum (reflected signal from polished granite), (b) calculated reflectivity of polished granite

Additional data is shown in figure 5.8 for reflectivity of sanded aluminum surfaces. The reflectivity of finer grit sanded surfaces gives higher values and these differences are larger for smaller frequencies.

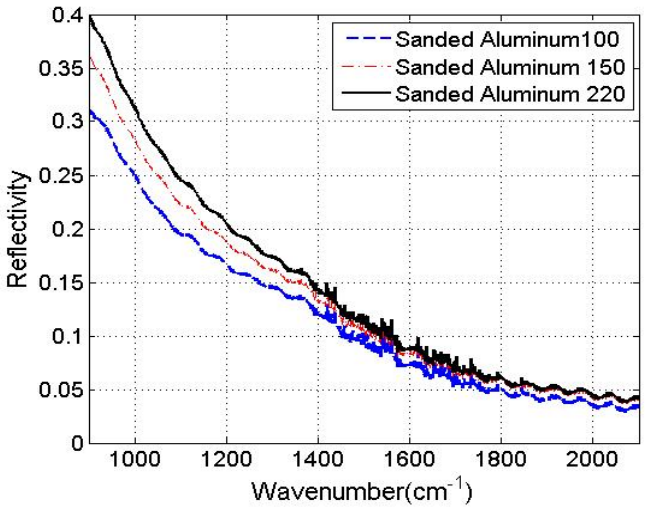

Figure 5.8: Calculated spectrum of reflectivity for sanded aluminum surfaces from 400 cm^{-1} to 2500 cm^{-1}

Both QCL backscattering measurement and FTIR system measurement of white ceramic tile are shown in figure 5.9. The reflectivity measurement with QCL is found to be ~20% smaller than reflectivity measurement with FTIR system at the same frequency which we attribute to small systemic instrument alignment errors and the very small reflectivity value.

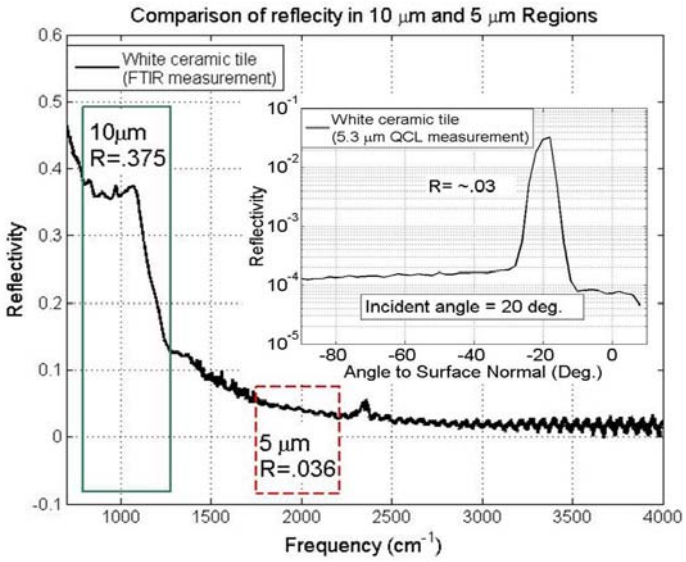

Figure 5.9: Comparison of reflectivity measurements using QCL and FTIR

It is also interesting to note that the FTIR backscattering measurement shows reflectivity of white ceramic wall tile at 10 μm is ~ 10 times larger than its reflectivity at 5μm. Similar results were observed in the other samples - polished granite, polished marble and sanded aluminum surfaces. This fact points to the benefit of open-path backscattering system design with longer path-length in 10μm wavelength region. The surface albedo for the urban building materials measured by QCL and FTIR are recorded in Table 5.1. The QCL measurement at 5.3 μm (column 2) is in good agreement with the results from FTIR at 5 μm (column 3) for white ceramic wall tile and polished granite. However, FTIR measurements are larger than QCL measurements for sanded aluminum surfaces which may be the results of strong water vapor absorbance near 5μm and geometric errors in experimental setup.

Sample Materials	**QCL measurements**	**FTIR measurements**	
	β@5.3μm	β@5μm	β@10μm
White ceramic wall tile	0.030	0.036	0.375
Polished granite	0.029	0.031	0.252
Polished marble	0.045	n/a	n/a
Unpolished aluminum	0.154	n/a	n/a
Concrete block	$6.8x10^{-4}$	n/a	n/a
Textured wall tile	$6.2x10^{-4}$	n/a	n/a
Unsanded aluminum	0.456	0.315	0.812
Sanded al. w/#220 grit	0.027	0.045	0.314
Sanded al. w/#150 grit	0.031	0.043	0.284
Sanded al. w/#100 grit	0.015	0.036	0.251
White painted white ceramic tile	$3.2x10^{-4}$	n/a	n/a
White painted on textured wall tile	$2.5x10^{-4}$	n/a	n/a

Table 5.1: Summary of albedo measurements on building materials using QCL and FTIR

To appreciate these results, we applied the above results to a simple link analysis, which was explained detail in chapter 3.4. In this model, optical efficiency (η) can be calculated from total power attenuation (α_{tot}) due to atmosphere conditions and sensor system components, relative power gain (γ_{tot}), receiver and link parameters (surface

albeto β, and solid angle Ω) as shown in equation 5.3. Total power loss for 1045 – 1047 cm^{-1} band with ozone, ammonia, water vapor and carbon dioxide absorption and solid angle depend on the path length of the system. Once the efficiency is calculated, the signal to noise ratio (SNR) can be calculated from equation 5.4.

$$\eta_{BS} = \alpha_{tot}\gamma_{tot}\beta_{ref}\Omega_{ref} \tag{5.3}$$

$$SNR = \frac{P_0 \eta D^*}{\sqrt{A_D \Delta f}} \tag{5.4}$$

where we used P_0 = 400 mW, D* = 5x10^9 Jones, detector area A_D=1mm x 1mm and Δf = 160 MHz. In figure 5.10, SNR values are shown using β = 0.3 and β = 0.8 for the path length between 100 m and 250 m.

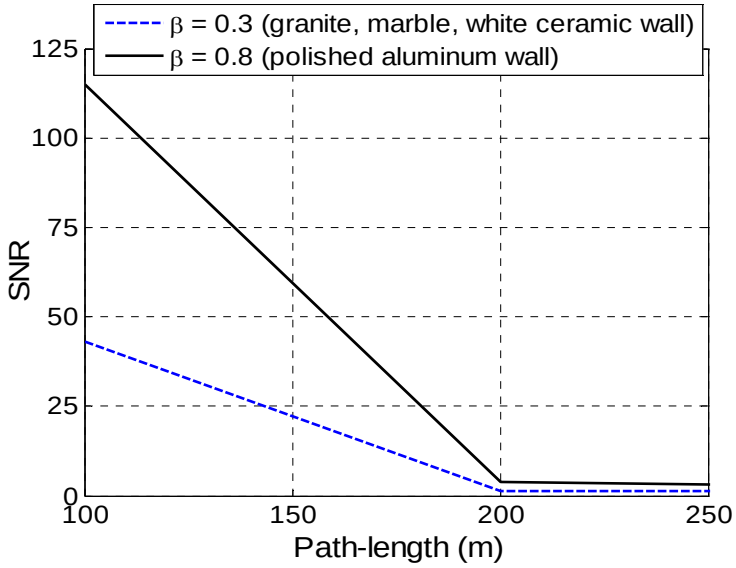

Figure 5.10: Calculated SNR for open-path backscattering systems using granite, marble, or white ceramic wall and aluminum wall between 100 m and 250 m path length

The results show that an open-path backscattering system using granite, marble or white ceramic wall tile can be deployed for 100 m path length as we average 10x10^3 pulses to reach SNR of 4x10^3 which give 1% accuracy results. If we use a polished

aluminum wall, we can decrease the averaged pulses to $1.3x10^3$ (these theoretical calculations did not take account on the effect of solid angle increases at a short distance measurements). In SNR calculation, we only included noise from the detector but noise from other sources, for example, DAQ system, and pre-amplifier, may dramatically reduce SNR. These factors will be accounted in future works.

References

[1] V. Vladutescu, B. Gross, F. Moshary, S. Ahmed, “Assessment of a QCL Laser Approach for the Simultaneous Measurement of Ambient Ammonia and Ozone” Proc. SPIE 6760, 676005 (2007)

[2] R. Prado and F. Ferreira, "Measurement of albedo and analysis of its influence the surface temperature of building roof materials", Energy and Building 37, 295-300 (2005)

[3] V. Degli-Esposti, F. Fuschini, E. Vitucci, and G. Falciasecca, "Measurement and modeling of scattering from buildings", IEEE Transactions on Antennas and Propagation, 55(1), 143-153 (2007)

[4] A. Earp, G. Smith, and J. Franklin, "Simplied BRDF of a Non-Lambertian Diffuse Surface", Lighting Res. Technol. 39(3), 265-281 (2007)

[5] H. Henshall, and J. Cruickshank, “Reflectance characteristics of selected materials for reference targets for 10.6 μm laser radars”, Applied Optics, 27(13), 2748-2755 (1988)

CHAPTER 6: CONCLUSION

6.1. Summary of the Thesis

This thesis is focused on the performance modeling (called Open-path System Model) and validation of a Quantum Cascade Laser Open-path System (QCLOPS) to monitor ambient gases, mainly O_3 and NH_3. The instrumentation of O_3-NH_3 open-path system is difficult due to 1) weak absorption features of O_3 and NH_3 compare to background gases, such as H_2O and CO_2, 2) requirement of hi-resolution laser to define fine spectral features of O_3, 3) availability of QCL in 9.6 μm range, which covers resonable strong O_3 and NH_3 absorption bands, with 100's of mW peak output power. The system design uses a single DFB pulsed QCL operating at 9.6 μm wavelength (1045 -1047 cm^{-1} range), corresponding to reasonably strong absorption lines of O_3, and NH_3. The GENSPECT codes with HITRAN database and the LSQ analysis are used to calculate the system's retrieval error as a function of SNR and then, the required SNR to 1% and 10% accuracies are defined.

The OPSM evaluates the system component parameters and calculates the attenuation of laser power along the path-length in the atmosphere by various mechanisms, such as particle scattering, turbulence, absorption, and free space laser beam propagation. From the received power at the detector via collecting telescope, and the system noise calculation, the SNR of measurement signal is determined and numbers of samples are averaged to reach the required SNR. Finally, the OPSM calculates the measurement time or temporal resolution of detection to accuracy as the function of path-

length. We found that dual O_3 and NH_3 1% accuracy detection can be done in < 1 s with the limit of detection as small as 0.4 ppb for O_3 and 30 ppt for NH_3 for L=1km.

The OPSM was validated with the several field measurements using currently implemented open-path system, the QCLOPS-CCNY which used a 5.3 μm QCL for H_2O concentration measurements. The results showed a good agreement and gave confidence on the design of O_3-NH_3 open-path sensor.

6.2. Proposed Future Work

In this thesis, we simulated the feasibility of the O_3-NH_3 open-path system using the model (OPSM), and this model was partially validated. However, the measurements were made using a strong absorption line of currently available QCL (5.3 μm emission) range and this did not realistically simulate the high SNR and large scale temporal averaging that would be needed. Therefore, in the absence of an available O_3-NH_3 source laser, we propose to further our validation studies through retrieval using small absorption feature.

To see if this is possible, we run the GENSPECT simulation to generate H_2O absorption features along with other interfering gas (CO_2) within the 1897-1903 cm^{-1} spectral window, which is the current 5.3 μm QCL emission range. As shown in figure 1, there is very small absorption feature of H_2O at 1898.67 cm^{-1}, and the CO_2 absorption is negligible in this window. Figure 1 (right) shows the H_2O absorption feature for L=40m, 60m, 100m, and 120m. To best simulate the conditions needed for O_3-NH_3, we look to further minimize the water vapor feature by using short path-lengths.

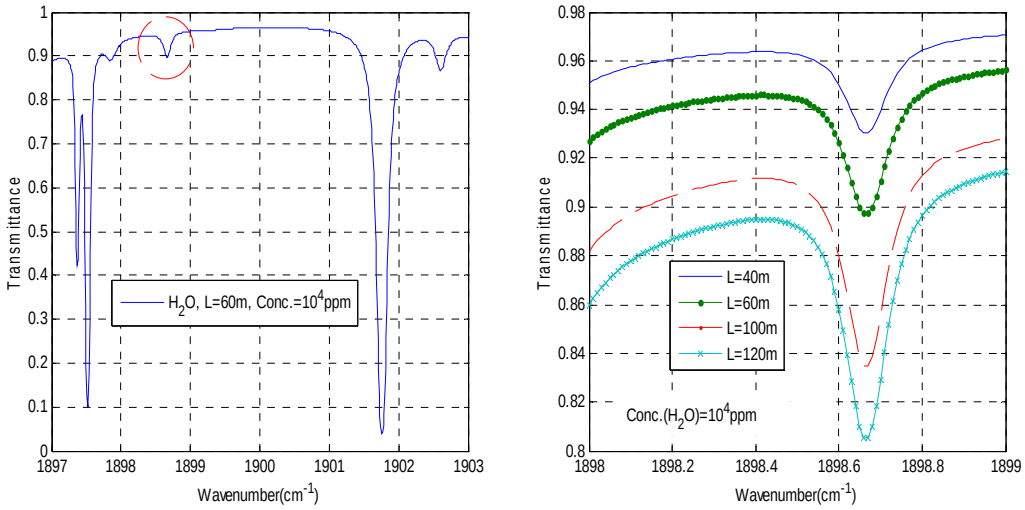

Figure 6.1: H_2O absorption feature in the spectral window in which current 5.3 µm QCL can be operated (left), and detailed view of H_2O small feature between 1898 and 1899 cm^{-1} (right)

The LSQ analysis, which is a critical part of the retrieval method, was performed for the spectral domain 1898 – 1899 cm^{-1} to calculate required SNR as the function of fractional error and the results are shown in figure 6.2.

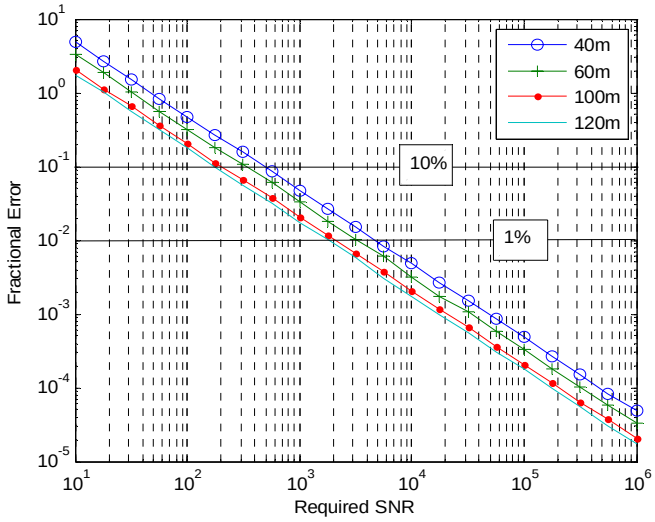

Figure 6.2: Required SNR of H_2O concentration retrival in 1898-1899 cm^{-1} window as the function of fractional error

We find that required SNR to obtain 1% retrieval accuracy for a path-length L=40m is $5x10^3$, which is comparable to the needed SNR for O_3-NH_3 retrieval at 1% accuracy for L=1km (i.e. $8x10^3$). Figure 6.3 shows the link model simulation results, number of samples and measurement time to 1% accuracy of H_2O peak at 1898-1899 cm^{-1} window, as the function of L.

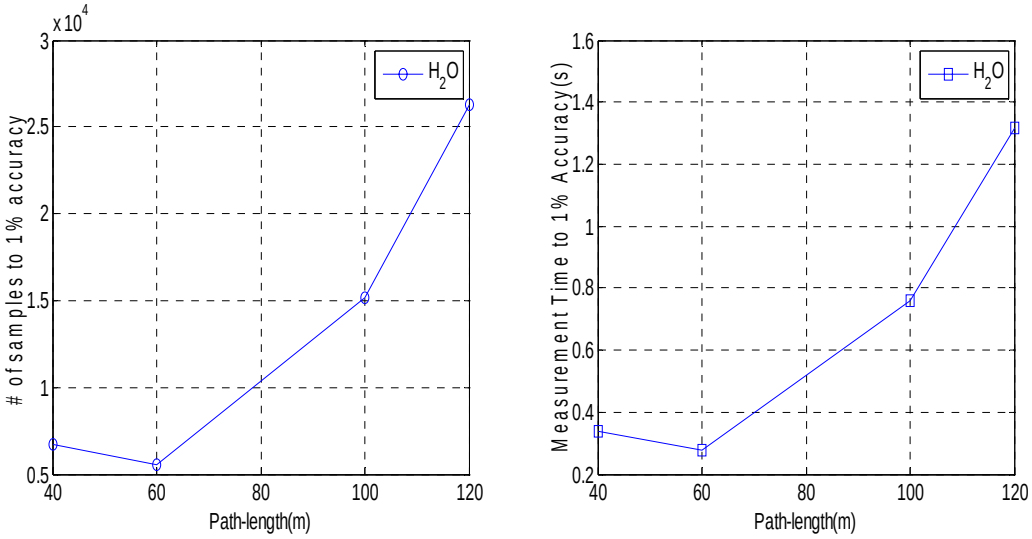

Figure 6.3: The link model simulation results (number of samples and measurement time) for H_2O peak retrieval at 1898-1899 cm^{-1} window (pulse rate = 20 kHz)

The results show that ~60k samples are needed and it will take ~0.3s for L=60m with QCL pulse rate = 20kHz.

Clearly, demonstration of pulling out and retrieving the water vapor concentration on this small feature provides very strong evidence that the ozone-ammonia retrieval is indeed feasible.

The proposed further works for this project is to build an O_3-NH_3 open-path sensor system using 9.6 μm (1045-1047 cm^{-1} range tunable) QCL. We can install a 9.6 μm QCL on the current QCLOP system and make several field measurements for O_3 and NH_3 concentration in different urban areas where air pollution has reached unhealthy level.

Packaging the retrieval algorithm and all other necessary programs, and development of a user friendly GUI, such as LabView for the system have to be done in near future. The DAQ system with high sampling rate, > 500 MS/s is required to process the data and it has to be reliable to build a compact portable system. Moreover, as explained in chapter 3 and 4, we have to implement the 2-axis tracker/positioned, which can be used to eliminate/reduce misalignment error.

APPENDIX

A: Further Investigation on the System Noise to Compare the Measurements with the Model Simulation Results

Analysis of turbulent noise

When a laser beam propagates through the atmospheric turbulence, the laser intensity fluctuation appears because of the random changes in the index of refraction. In this report, turbulent noise due to these fluctuations was analyzed using Rytov approximation, which is limited to the weak irradiance fluctuation conditions. The weak fluctuation for a Gaussian-beam is defined as when

$$\sigma_1^2 \langle 1 \text{ and } \sigma_1^2 \Lambda^{5/6} \langle 1 \tag{A-1}$$

where σ_1^2 is Rytov variance and calculated as

$$\sigma_1^2 = 1.23 C_n^2 k^{7/6} L^{11/6} \tag{A-2}$$

where C_n^2 is the refractive-index parameter and it varies between 10^{-13} and 10^{-17} ($C_n^2 = 10^{-14}$ is used in our analysis based on the weather condition during our measurements), $k=2\pi/\lambda$, L is path-length and

$$\Lambda = \frac{2L}{kW^2} \tag{A-3}$$

where W is the laser beam radius at the receiver. In our system with 5.3μm QCL, we calculated $\sigma_1^2 = 0.981 \times 10^{-3}$ and $\sigma_1^2 \Lambda^{5/6} = 3.804 \times 10^{-5}$ for L=120m, and which defined that

our Gaussian-beam wave had weak fluctuation regime and valid to use Rytov approximation.

In Rytov approximation, the longitudinal component of scintillation index or normalized variance of the irradiance describes the fluctuations of received irradiance of the laser beam which propagates through the atmosphere as shown in equation A-4.

$$\sigma_I^2(L) = \frac{\langle I^2 \rangle}{\langle I \rangle^2} - 1 \tag{A-4}$$

where $<I^2>$ and $<I>^2$ are mean of intensity square and square of mean intensity respectively. For a collimated laser beam, $\sigma_I^2(L) = \sigma_1^2$ (scintillation index = Rytov variance). Moreover, if the receiving telescope aperture is larger than the irradiance correlation length, the scintillation index decreases by the factor of A and A is defined as

$$A = \frac{\sigma_I^2(D)}{\sigma_I^2(0)} \tag{A-5}$$

where $\sigma_I^2(D)$ and $\sigma_I^2(0)$ are scintillation indexes of telescope aperture diameter D and point detector respectively. The aperture averaging factor A can be calculated as:

$$A = \left[1 + 1.062 \left(\frac{kD^2}{4L} \right) \right]^{-7/6} \tag{A-6}$$

Figure 1 shows the Rytov variance and $\sigma_I^2(D)$ of the 5.3μm QCL system as the function of path-length (D_{tel}=20.3cm) .

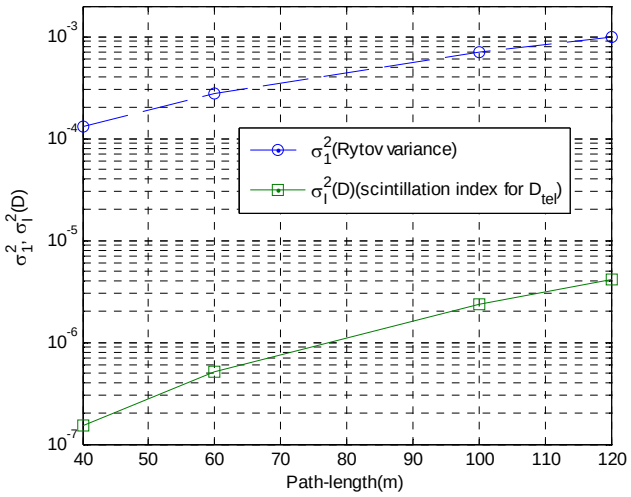

Figure (A-1): Rytov variance and scintillation index with aperture averaging

The longitudinal intensity fluctuation is calculated using $\sigma_I^2(D)$ and equation 4.

$$I_1 = \sqrt{\left(\sigma_I^2 + 1\right)\langle I_r \rangle^2} - I_r \tag{A-7}$$

where I_r is received power after path-length of L. The Vrms of turbulent noise is calculated from the optical power fluctuation I_1 and it is plotted in figure 2 together with detector noise, preamp noise (without gain factor), DAQ noise and total RMS noise.

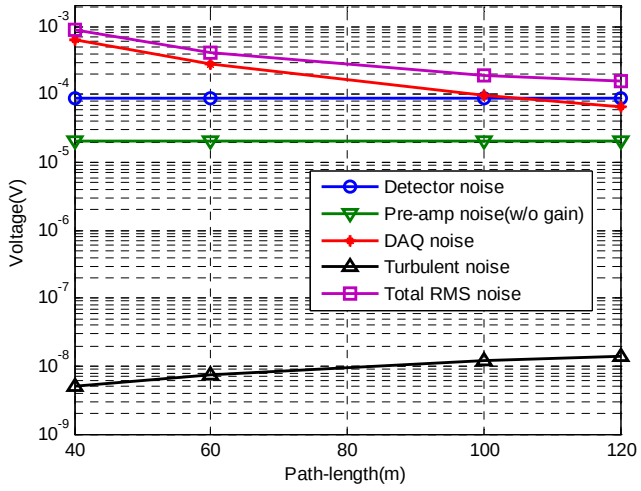

Figure (A-2): Comparison of turbulent noise with detector noise, pre-amp noise (without gain factor), DAQ noise and total RMS noise.

The results show that RMS turbulent noise due to intensity fluctuation is between $5x10^{-9}$ and $2x10^{-8}$ for L=40 to 120m, and it is negligible (4 orders of magnitude lower than detector noise).

Analysis of Preamp noise

The output noise after a preamplifier is determined by the preamp noise sources, together with the detector characteristics and it can be stated in equation A-8 [2].

$$e_n(f) = [\frac{e_n^2}{Z_D^2} + i_n^2 + (\frac{4kT}{R_D}) + (\frac{4kT}{R_F})]^{1/2} Z_F \tag{A-8}$$

where e_n is output noise density, e_n is preamplifier noise voltage, Z_D is the detector reactance, i_n is preamplifier current noise, k is Boltzmann's constant, T is temperature in degree Kelvin, R_D is the detector shunt resistance, R_F is preamp feedback resistance, and Z_F is the transimpedance gain. The preamplifier noise is normally specified as a spectral density in rms voltage or amp per square root of bandwidth and it is a normalized to a 1-Hz noise bandwidth and transimpedance gain $Z_F = 1$ [3].

The preamp (model #: Perry 481-200) which is used in our QCLOPS-CCNY, is specified that spectral noise density=1.8nV/√Hz, gain = $1000/R_D$, where R_D is the detector resistance [4]. According to the definition of spectral noise density and preamp datasheet provided by the Boston Electronics, which does not make the detector (model #: Vigo PVI-3TE-10.6), we have to include gain factor in the calculation of total system noise. Actually, the total output noise after preamp can be calculated as:

$$e_{n,tot} = [e_{n,\det}^2 + e_{n,amp}^2]^{1/2} \times G \tag{A-9}$$

where $e_{n,tot}$ is total output noise after preamp, $e_{n,det}$ is detector noise, $e_{n,amp}$ is preamp noise (spectral noise density x bandwidth), and G is the gain.

In conclusion, the results from the analysis of turbulent noise and analysis of preamp noise show that the noise due to the laser beam fluctuation by atmospheric turbulence is negligible ($<2x10^{-8}$ for L=120m) and including gain factor in preamp noise calculation provides the agreement on the our field measurements with the link power model.

B: Investigation on Quantization level and Noise Signal in the Process of Averaging Samples to Improve Measurement SNR

In the OPSM model, we used averaging samples to reach the required SNR which was more than 3 orders of magnitude higher than per pulse SNR while our retrieving features is very tiny (smaller than noise). The two reasons which motivated to do this analysis are 1) can we bring down noise level to lower than the tiny absorption feature using current quantization system, and 2) does SNR improvement follow √n rule in more than 10^3 time averaging.

We set a signal with a small feature which is 0.1R (R is the DAQ resolution), and 3 different levels of noise (N=0.1R, N=R, N=10R) were added to the signal. We averaged signal 10 to 10^8 times and outputs were calculated in quantized values and actual analog values. The results are shown in figure 1. As shown in figure 1C, the quantized values have a good agreement with the real values when N > R, but the quantized values are different from the real values when N < R (figure 1A). Moreover, averaging 10^8 times improves the ratio of noise and signal feature by 10^4 times. We also repeated the analysis over 100 times and the results were as we stated (figure 2).

This analysis gives confidence on the process of retrieving a small absorption feature in a signal with the noise which is larger than DAQ resolution.

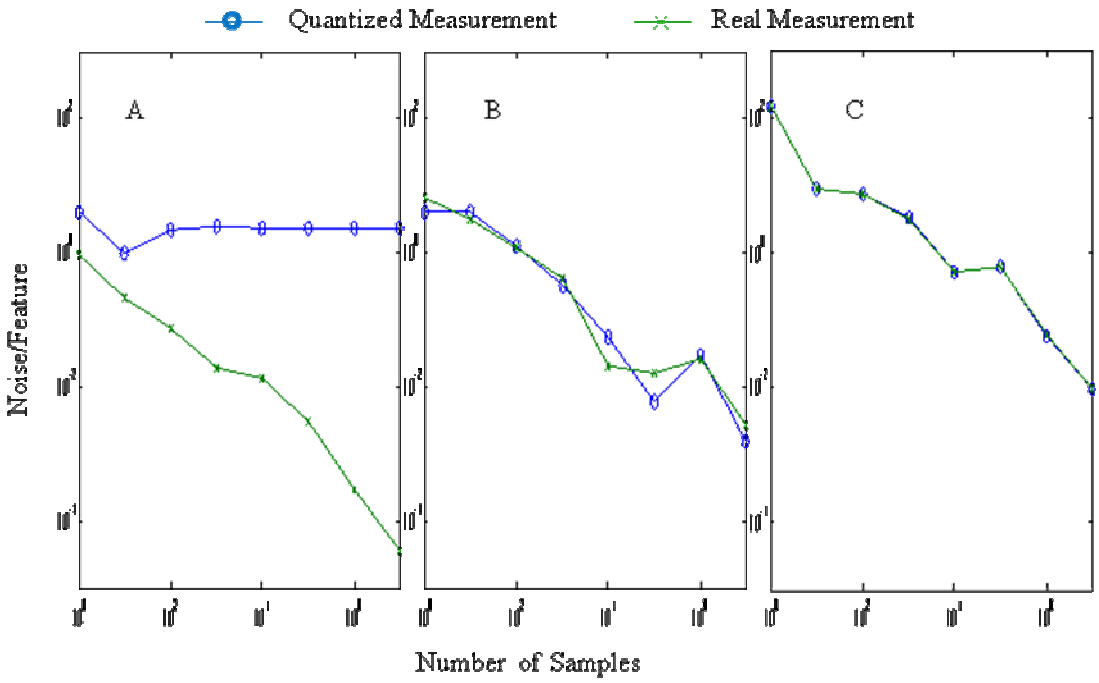

Figure (A-3): Comparison of quantized measurement and real measurement: (A) N = 0.1R, (B) N = R, and (C) N = 10R

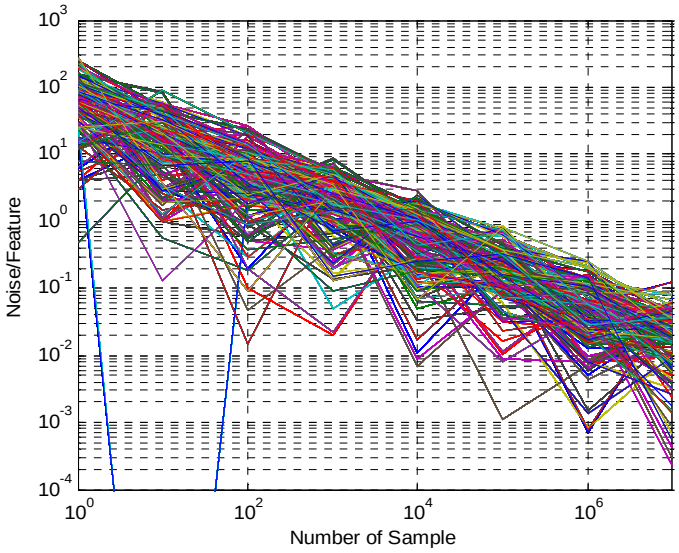

Figure (A-4): Results of 100 cases

References:

[1] L. Andrews, R. Phillips, “Laser Beam Propagation through Random Media”, SPIE Optical Engineering Press, Washington (1998)

[2] Teledyne Judson Technologies, “Preamplifiers”, at http://www.teledynejudson.com/preamp.html

[3] J. Graeme, “Photodiode amplifier: op-amp solutions, chapter 5.1.3 Total rms output noise”, McGraw Hill, New York, (1996) (pp88-92)

[4]Boston Electronics Corporation, “Preamps: DC-Coupled Preamps for Photovoltaic HgCdZnTe detector”, at http://www.boselec.com/products/documents/co2laserdetectors.pdf

BIBLOGRAPHY

Chapter 1

[1] http://www.citymayors.com/environment/polluted_uscities.html

[2] D. Liu, and B. Liptak, "Environmental Engineers' Handbook", CRC Press (1999)

[3] J. Renard, S. Calidonna, and M. Henley, "Fate of ammonia in the atmosphere - a review for applicability to hazardous releases", J. of Hazardous Materials, B108, 29-60 (2004)

[4] US EPA, "Ground-level Ozone Standards Designations", and "Ozone and your Health" at http://www.epa.gov/ozonedesignations/, and http://www.epa.gov/airnow//ozone-c.pdf

[5] http://www.mirthecenter.org/research.aspx

[6] V. Vladutescu, B. Gross, F. Moshary, S. Ahmed, "Assessment of a QCL Laser Approach for the Simultaneous Measurement of Ambient Ammonia and Ozone" SPIE Proceedings, 6760-6768 (2007)

[7] F. D'Amato, P. Mazzinghi, F. Castagnoli, "Methane analyzer based on TDL's for measurements in the lower stratosphere: design and laboratory tests", Appl. Phys. B75, 195-202 (2002)

[8] M. Lwin, "Evaluation of Quantum Cascade Laser Open-path Systems", thesis proposal (2008)

Chapter 2

[1] F. Tittel, D. Richter, and A. Fried, "Mid-Infrared Laser Applications in Spectroscopy", Appl. Phys. **89**, 445-516 (2003)

[2] G. Stephens, "Remote Sensing of the Lower Atmosphere", Oxford University Press, New York (1994)

[3] J. Renard, S. Calidonna, and M. Henley, "Fate of ammonia in the atmosphere - a review for applicability to hazardous releases", J. of Hazardous Materials, B108, 29-60 (2004)

[4] http://www.osha.gov/dts/chemicalsampling/data/CH_218300.html

[5] US EPA, "Ground-level Ozone Standards Designations": http://www.epa.gov/ozonedesignations/

[6] J. M. Hollas, "Modern Spectroscopy", 4th ed., John Wiley & Sons, Inc., New Jersey (2004)

[7] G. Herzberg, "Molecular Spectra and Molecular Structure II: Infrared and Raman Spectra of Polyatomic Molecules", 7th printing, D. Van Nostrand Company, Inc., New Jersey (1956)

[8] R. M. Goody and Y. L. Yung, "Atmospheric Radiation: Theoretical Basis", Oxford University Press, New York (1989)

[9] G. Petty, "A First Course In Atmospheric Radiation", 2nd Ed., Sundog Publishing, Madison, WI (2006)

[10] L. S. Rothman, et al., "The HITRAN molecular spectroscopic database and HAWKS (HITRAN AtmosphericWorkstation): 1996 edition", J. Quant. Spectrosc. Radiat. Transfer, **60**, 665–710 (1998)

[11] L. S. Rothman, et al., "The HITRAN molecular spectroscopic database: edition of 2000 including updates through 2001", J. Quant. Spectrosc. Radiat. Transfer, **82**, 5–44 (2003)

[12] L. S. Rothman, et al., "The HITRAN 2004 molecular spectroscopic database", J. Quant. Spectrosc. Radiat. Transfer, **96**, 139–204 (2005)

[13] B. M. Quine, J. R. Drummond, "GENSPECT: a line-by-line code with selectable interpolation error tolerance", Journal of Quantitative Spectroscopy & Radiative Transfer , **74**, 147-165 (2002).

[14] D. Haaland, and R. Easterling, "Application of New Least-squares Methods for the Quantitative Infrared Analysis of Multicomponent Samples" Appl. Spec. vol. 36, 665-673, 1982

[15] S. Chapra, and R. Canale, "Numerical Methods for Engineers", 6th ed., McGraw-Hill Higher Education, Boston (2010)

[16] A. Kosterev and F. Tittel, "Chemical Sensors Based on Quantum Cascade Lasers" IEEE JQE vol. 38, no. 6, 582-591 (2002)

[17] R. Pierret, "Advanced Semiconductor Fundamentals" vol 6, 2nd ed. Prentice Hall, NJ (2003)

[18] Bell Labs technical information at http://www.bell_labs.com/org/physicalsciences/psr/qc/index.html

[19] J. Faist, F. Capasso, C. Sirtori, D. Sivco, A. Hutchinson, S. Chu, and A. Cho, "Narrowing of the Intersubband electroluminescent Spectrum in Coupled-Quantum-Well Hetrostructures" Appl. Phys. Lett., vol. 65, 94-96, 1994

[20] D. Hofstetter, J. Faist, M. Beck and A. Muller, "Demonstration of high-performance 10.16 mm quantum cascade distributed feedback lasers fabricated without epitaxial regrowth" Appl. Phys. Lett. vol. 75 no.5, 665-667 (1999)

[21] DFB Pulsed Room-Temperature lasers at http://www.alpeslasers.com/lasers-on-stock/index.html

Chapter 3

[1] B. M. Quine, J. R. Drummond, "Genspect: a line by line code with selectrable interpolation error tolerance", JQSRT **74** 147-165 (2003).

[2] L.S. Rothman, A. Barbe, D.C. Benner, L.R. Brown, C. Camy-Peyret and M. Carleer et al., "The HITRAN molecular spectroscopic database: edition of 2000 including updates through 2001, JQSRT **82** 5–44 (2003).

[3] V. Vladutescu, B. Gross, F. Moshary, S. Ahmed, "Assessment of a QCL Laser Approach for the Simultaneous Measurement of Ambient Ammonia and Ozone" SPIE Proceedings, 6760-6768 (2007)

[4] F. Tittel,D. Richter, and A. Fried, "Mid-infrared laser applications in spectroscopy" Springer Berlin, **89**, 458-529 (2003)

[5] http://www.maxion.com/singlemode.html

[6] "User Manual for LS-03-D Laser System", Cascade Scientific, Document Number D-7010-0003 (2007)

[7] www.vigo.com.pl, from VIGO System, S.A., Warsaw, Poland

[8] V. Rutten, ¨Telescope Optics; A Comprehensive Manual For Amateurs¨, WIllmann-Bell, Inc., Virginia (2003)

[9] http://www.galacticfool.com/collimate-newtonian-telescope

[10] G. Duxbury, N. Langford, M. McCulloch, and S. Wright, "Quantum Cascade Semiconductor Infrared and Far-infrared Lasers: from Trace Gas Sensing to Non-linear Optics", Chem. Soc. Rev., 34, 921-934 (2005)

[11] Z. Bielecki, W. Kolosowski, J. Mikolajczyk, "Free-space Optical Data Link Using Quantum Cascade Laser", PIERS Proceedings, Cambridge, USA, July 2-6 (2008)

[12] A. Biswas and M. Wright, "Mountain-Top-to-Mountain-Top Optical Link Demonstration: Part I", IPN Progress Report, 42-149 (2002)

[13] A. Prokes, "Atmospheric effects on availability of free space optics systems", Optical Engineering 48(6), 066001 (2009)

[14] B. Saleh, and M. Teich, "Fundamentals of Photonics", 2nd ed., Wiley-Interscience (2007)

[15] P. Corrigan, M. Lwin, B. Gross, F. Moshary, "Design of an ozone and ammonia open-path sensor with a quantum cascade laser", prepared to submit to a technical journal

[16] P. Corrigan, "Quantifying QCL System Noise", presentation slides

[17] W. Kester, "Understand SINAD, ENOB, SNR, THD, THD + N", Mt-001 Tutorial, Analog Devices (2009)

[18] L. Kristensen, P. Kirkegaard, "Digitization Noise in Power Spectral Analysis", Journal of Atmospheric and Oceanic Technology, **4**, 328-335 (1987)

[19] http://64.106.166.130/techSupport/resource_center/downloads/wp-understanding-lasers-and-laser-optics.pdf

Chapter 4

[1] T. Ball, "Water vapor is the most powerful greenhouse gas", at http://www.skepticalscience.com/water-vapor-greenhouse-gas.htm

[2] P. Corrigan, M. Lwin, B. Gross, F. Moshary, "Design of an ozone and ammonia open-path sensor with a quantum cascade laser", prepared to submit to a technical journal

[3] Infrared detector catalog from Vigo System S.A. at http://www.vigo.com.pl/index.php/en/english_menu/products/ir_detectors

[4] F. Pedrotti, L. Pedrotti, L. Pedrotti, "Introduction to Optics", 3rd ed., Benjamin Cummings, (2006).

[5] E. Normand, M. McCulloch, G. Duxbury, N. Langford, N., "Fast, real-time spectrometer based on a pulsed quantum-cascade laser", Optics Letters **28**, 1 (2003).

[6] M. McCulloch, E. Normand, L. Langford, G. Duxbury, D. Newnham, "Highly sensitive detection of trace gases using the time-resolved frequency downchirp from pulsed quantum-cascade lasers", J. Opt. Soc. Am. B **20**, 8 (2003).

[7] J. McManus, P. Kebagian, M. Zahniser, "Astigmatic mirror multipass absorption cells for long-path-length spectroscopy", Applied Optics, 34 (18), 3336-3348 (1995)

[8] http://www.aerodyne.com/products/amac/astigmatic_absorpt.htm

[9] P. Corrigan, M. Lwin, R. Huntley, A. Chhabra, F. Moshary, B. Gross and S. Ahmed, "Portable open-path chemical sensor using a quantum cascade laser", Proc. SPIE 7312, 73120P (2009)

[10] The NYCMetNet surface data by the Remote Sensing Laboratory of The City College of New York at http://nycmetnet.ccny.cuny.edu/Data-Download_Surface.asp

[11] R. Heinsohn, and J. Cimbala, "Indoor Air Quality Engineering: Environmental Health and Control of Indoor Pollutants (Drugs and the Pharmaceutical Sciences)", 1st ed., CRC Press (2003)

[12] Open-path FTIR Air Monitoring System, Supplement Manual by MIDAC Corporation

[13] V. Vladutescu, B. Gross, F. Moshary, and S. Ahmed "Assessment of a QCL Laser Approach for the Simultaneous Measurement of Ambient Ammonia and Ozone" SPIE Proceedings, 6760-6768 (2007)

[14] V. Saptari, "Fourier-Transform Spectroscopy Instrumentation Engineering", SPIE Press, Washington, (2004)

[15] P. Griffiths and J. Haseth, "Fourier Transform Infrared Spectrometry", 2nd ed., John Wiley & Sons, Inc., New Jersey (2007)

Chapter 5

[1] V. Vladutescu, B. Gross, F. Moshary, S. Ahmed, "Assessment of a QCL Laser Approach for the Simultaneous Measurement of Ambient Ammonia and Ozone" Proc. SPIE 6760, 676005 (2007)

[2] R. Prado and F. Ferreira, "Measurement of albedo and analysis of its influence the surface temperature of building roof materials", Energy and Building 37, 295-300 (2005)

[3] V. Degli-Esposti, F. Fuschini, E. Vitucci, and G. Falciasecca, "Measurement and modeling of scattering from buildings", IEEE Transactions on Antennas and Propagation, 55(1), 143-153 (2007)

[4] A. Earp, G. Smith, and J. Franklin, "Simplied BRDF of a Non-Lambertian Diffuse Surface", Lighting Res. Technol. 39(3), 265-281 (2007)

[5] H. Henshall, and J. Cruickshank, “Reflectance characteristics of selected materials for reference targets for 10.6 μm laser radars”, Applied Optics, 27(13), 2748-2755 (1988)

PUBLICATION AND PRESENTATIONS

1. **M. Lwin**, P. Corrigan, B. Gross, F. Moshary and S. A. Ahmed, "Performance Modeling and Validation of a Chirped Pulse Quantum Cascade Laser for Open-path Ambient Gas Monitoring", prepared to submit to the Applied Optics (2010)

2. **M. Lwin**, P. Corrigan, B. Gross, F. Moshary and S. A. Ahmed, "Mid-infrared Backscattering Measurements of Building Materials using a Quantum Cascade Laser", SPIE Proc. Vol. 7660-43 (2010)

3. **M. Lwin**, P. Corrigan, B. Gross, F. Moshary and S. A. Ahmed, "Mid-infrared Backscattering Measurements of Building Materials using a Quantum Cascade Laser", poster presentation, SPIE Defense, Security and Sensing 2010, Orlando, FL, (April 2010)

4. **M. Lwin**, P. Corrigan, P. Castillo, C. Padilla, B. Gross, F. Moshary and S. A. Ahmed, "Albedo Measurements of Urban Building Materials for Open-path Quantum Cascade Laser Baskscattering System", poster presentation, Princeton University, NJ, (March 2010)

5. **M. Lwin**, P. Corrigan, B. Gross, F. Moshary, "Evaluation of a Multispectral Retrieval Analysis for Quantum Cascade Laser Open-path System using Multipass Gas Cell Configuration", oral presentation, Mid-infrared Technologies for Health and the Environment (MIRTHE) Summer Workshop, St. John's University, New York, NY, (August 2009)

6. P. Corrigan, **M. Lwin**, B. Gross, F. Moshary, "Assessment of Dual Ammonia and Ozone Open-Path Sensing with a Quantum Cascade Laser", poster presentation, CLEO/IQEC 2009, Baltimore, MD, (June 2009)

7. P. Corrigan, **M. Lwin**, R. Huntley, A. Chhabra, F. Moshary, B. Gross, S. Ahmed, "Portable Open-Path Chemical Sensor using a Quantum Cascade Laser", oral presentation, SPIE Defense, Security and Sensing 2009, Orlando, FL, (April 2009)

8. **M. Lwin**, P. Corrigan, R. Huntley, A. Chhabra, B. Gross, F. Moshary, "Open-Path Quantum Cascade Laser System for Ambient Air Quality Monitoring", poster presentation, Princeton University, NJ, (February 2009)

9. **M. Lwin**, "Evaluation of Quantum Cascade Laser Open-path System Designs", oral presentation and Ph. D. Thesis Proposal, the City College of New York, NY, (September 2008)